Novel 3D Tomographic Techniques with Applications to Flame Imaging

A dissertation presented to the faculty of the School of Engineering and Applied Science

University of Virginia

In partial fulfillment of the requirements for the degree

Doctor of Philosophy

In Mechanical and Aerospace Engineering

by

Christopher I. Windle

May 2024

APPROVAL SHEET

This
Dissertation
is submitted in partial fulfillment of the requirements
for the degree of
Doctor of Philosophy

Author: Christopher Windle

This Dissertation has been read and approved by the examing committee:

Advisor: Lin Ma

Advisor:

Committee Member: Daniel Quinn

Committee Member: Harsha Chelliah

Committee Member: Zongli Lin

Committee Member: Vamshi Korivi

Committee Member:

Committee Member:

Accepted for the School of Engineering and Applied Science:

Jennifer L. West, School of Engineering and Applied Science

May 2024

Abstract

In order to resolve the turbulent and three-dimensional (3D) structures of combustion processes, four-dimensional (4D) diagnostics, meaning time-resolved measurements including all three spatial dimensions, are required. These 4D measurements are critical in understanding flame behaviors in a multitude of practical applications. Computed tomography (CT) is a key tool in obtaining instantaneous 3D flame measurements by using multiple two-dimensional (2D) line-of-sight projections collected from cameras to generate a 3D reconstruction of a signal emission distribution within a flame, and these measurements can be considered 4D when they are time-resolved. However, obtaining 4D combustion measurements with sufficient spatial and temporal resolution has many challenges. While improvements in camera technology and the use of additional cameras may yield higher spatial resolution, typically these factors are limited for a given experimental setup. Therefore, new techniques must be developed to maximize the spatial resolution of a given setup. Additionally, due to the large amounts of data required for 3D CT, which is compounded by the need for time-resolved measurements, improved techniques are desired that can reduce the computational costs in both time and memory while maintaining reconstruction accuracy. The primary focus of this dissertation is the development and analysis of improved algorithms to achieve the goals of reducing computational costs without a loss in accuracy, while also implementing them in such a way as to improve the spatial resolution of the reconstructions.

First, this dissertation describes an adaptive spatial discretization (ASD) technique that aims to reduce computational costs without a loss in accuracy by identifying regions within the reconstructed measurement volume that require either high or low spatial resolution and treating these regions respectively with a fine or coarse discretization. This way, only regions that require a higher resolution, mainly those regions with large spatial gradients, are solved using a fine discretization, so that the total amount of computational resources required for CT can be reduced while still maintaining accuracy in important regions. This method was validated using a phantom study using six cases that represent a range of distributions found in tomography applications.

In addition to the ASD method, a pixel masking method is described that has been applied to volumetric laser-induced fluorescence (VLIF) measurements. The masking method works on the principle that all voxels that contribute to pixels containing signal below an estimated signal floor must contain no substantial emission and can be removed from the tomographic reconstruction. This reduction of pixels and voxels reduces the computational costs of CT without adversely affecting reconstruction accuracy. This method was validated by directly comparing the results of the VLIF reconstruction to 2D planar LIF (PLIF) measurements. Both the ASD and masking techniques were used to reduce the computational costs of CT without reduction in reconstruction accuracy and also showed the ability to improve spatial resolution, satisfying two key needs of obtaining 3D and 4D combustion measurements.

In terms of practical demonstration, limited space and harsh conditions are typical and present challenges in implementation. Under many practical conditions of interest, it is difficult to obtain experimental data with enough views to perform tomography with adequate accuracy and resolution. These challenges are worsened under field conditions, outside of a laboratory environment. To enable visualization of flames under practical conditions, this work describes a proof-of-concept demonstration using fiber-based endoscopes (FBE) in conjunction with a single camera. Results showed the design could significantly reduce the equipment cost and footprint and allowed visualization of flames inside a ground vehicle testbed with limited viewing access. The time-resolved 3D measurements were used to resolve the temporal dynamics and spatial structures of the target flame under challenging experimental conditions. This experimental setup has shown to be capable of delivering 4D tomographic capabilities under challenging conditions and may serve as a promising platform for future practical measurements. With a combination of progress in both data acquisition and data processing techniques, as described earlier, this dissertation contributes to the advancement of combustion tomography and diagnostics, as well as providing techniques that may be applicable to a wide range of tomography applications.

Acknowledgments

First, I would like to thank my advisor Lin Ma for his constant support and mentorship. His guidance helped me to become a better writer, communicator, scientist, and engineer.

Thank you also to Dr. Dan Quinn, Dr. Harsha Chelliah, Dr. Zongli Lin, and Dr. Vamshi Korivi for taking the time and effort to serve on my Ph.D. committee, and for providing me with feedback to improve this dissertation.

I am appreciative of the collaboration and opportunities afforded to me by the U.S. Army and Air Force Research Labs. Thanks to them, I was able to work with many talented people on some very interesting projects.

Finally, I would like to thank my family and friends for their constant support during this journey. I especially thank my wonderful wife Sara for encouraging me to follow my dreams and for her unwavering support, as well as our daughter Evelyn for being a welcome (and sometimes unwelcome) distraction during my final years as a graduate student.

Table of Contents

List of Figures

Chapter 1

1. Introduction

1.1. Background and Motivation

The study of combustion processes continues to be an area of active research across many disciplines. This includes studies to improve the efficiency and design of combustion engines, propulsion devices, and industrial power generation [1-3], expand our fundamental understanding of combustion mechanics [4, 5], and improve safety in fire events [6-8]. Towards these goals, combustion diagnostics seek to measure and characterize flame properties such as temperature and chemical species distributions [9], heat release rate and equivalence ratio [10], and flame structure [11], to better understand the underlying flame dynamics. However, such measurements can be difficult to obtain using traditional experimental techniques due to a lack of both spatial and temporal resolution, as well as being invasive and challenging in the harsh environments near combustion processes. For instance, the use of multiple thermocouples to measure the flame temperature distribution not only severely lacks spatial resolution, but also risks disturbing the flow itself [12]. For this reason, optical techniques are optimal for multi-dimensional combustion measurements.

Much work has been devoted to obtaining one-dimensional (1D) and two-dimensional (2D) measurements of various flame parameters via less invasive means [13-15]. However, these measurements fail to fully characterize flames in most practical combustion processes because these flames are inherently unsteady and three-dimensional (3D). In order to completely characterize and understand flame mechanics, 3D measurement techniques are required. One method to extend the 2D laser technique to 3D, called planar laser-induced fluorescence (PLIF), was to quickly scan the laser sheet across the flame, although this technique suffers from poor temporal and spatial resolution and also significant equipment considerations that would be infeasible under field conditions

[16, 17]. In another study, 3D flame surface density was estimated using 2D measurements but relied on averaged parameters, models, and assumptions of flame behavior [18]. These examples highlight the need for direct 3D measurements to improve temporal and spatial resolution, as well as inform computational models of combustion.

Computed tomography (CT) is a valuable tool in the study of combustion, as it enables multi-dimensional measurements to be acquired through non-invasive means [19-21]. CT is an optical measurement technique that uses multiple line-of-sight images, called projections, from cameras to generate an instantaneous 3D reconstruction of a signal distribution [22]. In many applications of tomography, the measurement volume is discretized into small cubes called voxels (analogous to 3D pixels) that represent the signal intensity at each voxel location, and the voxel intensities are solved for using the measured projections. While CT is mainly known for its use in the medical field, it has been used across many different disciplines, including material inspection, geophysics, and, most important to this dissertation, combustion studies [23-26].

When applied to combustion processes, CT typically aims to reconstruct a 3D emission signal distribution. Depending on what is being measured, the signal could be chemiluminescence, incandescence, or fluorescence from soot or radicals in the flame [27]. In many cases, the collected signal is generated by the flame, while in others these signals can be induced using a laser. As mentioned, PLIF has long been an optical technique for the study of flames, but recent advances in laser technology have allowed for volumetric LIF (VLIF) measurements to be taken, to which CT has been applied to obtain direct 3D laser-induced flame measurements [28, 29]. In these cases, the thin laser sheet has been expanded to a thicker laser slab that illuminates the entire measurement volume, and multiple cameras can simultaneously image the emitted signal.

Regardless of the method used to collect a flame signal, the 3D reconstruction process has significant computational costs in both time and memory [30]. To reliably apply tomography to generate a 3D signal reconstruction, three simultaneous line-of-sight projections are needed at a minimum, although more are necessary to improve accuracy and resolution [19, 31, 32]. In one case, as many as 40 simultaneous images were collected for use [33]. Due to the large amounts of data collected, iteratively solving for the 3D signal

2

distribution using tomography requires significant computational resources. For example, one typical setup using five megapixel cameras required approximately 50 GB of memory [31]. In addition, many minutes or even hours may be required to obtain a 3D reconstruction of a single instantaneous frame [34, 35]. As cameras continue to improve in pixel resolution, while further improving the available spatial resolution and scale of tomographic reconstructions, the computational costs will continue to increase. Additionally, with the use of high-speed cameras, time-resolved flame measurements can be acquired that enable 4D flame analysis that is able to resolve the transient nature of spatial structures. However, because each frame must be reconstructed individually, the computational costs are compounded even further for 4D measurements. For these reasons, and with the ultimate goal of real-time diagnostics, significant improvements to the computational efficiency of tomography algorithms are sorely desired [36]. The first key motivation of this dissertation is the development and analysis of improved algorithms to reduce the computational requirements of obtaining 4D tomography measurements, with a focus on combustion.

While the application of CT to flame diagnostics has enabled instantaneous 3D measurements, obtaining these measurements is not without challenge. The setups for multi-dimensional flame measurements, particularly those that include laser diagnostics, can be expensive and have a significant physical footprint. A typical experimental setup may include multiple high-speed cameras to capture images of the target flame from multiple orientations [37, 38]. On-site and *in situ* setups may be unable to accommodate many cameras due to space or viewing limitations, so alternative solutions are required to enable data acquisition [33].

Endoscopes have proven to be useful tools that allow for image acquisition equipment, such as cameras, to be located safely away from hazards, while also being small enough to place in confined locations. For example, one group placed an endoscope within the combustion chamber of a test engine cylinder to assist in combustion imaging, which would otherwise be impossible using a traditional camera setup [39]. Recent advances in fiber-optic technology allow for multiple fiber inputs to collect into a single output that can be viewed by a single camera. In this way, a single camera can simultaneously view a flame

Figure 1.1: Ground vehicle testbed where flame measurements were taken, located at Aberdeen Proving Grounds, MD. Photo courtesy of the U.S. Army Research Lab.

from multiple orientations, reducing a flame visualization setup's financial cost and physical footprint. While multi-input fiber-based endoscopes (FBE) have been used in other works, they have been implemented in laboratory environments and have not yet been demonstrated for large-scale field measurements prior to this work [34, 40].

The second key motivation for this dissertation is therefore the demonstration of a proof-of-concept integrated sensor design to visualize large, turbulent flames *in situ* and under field conditions. A large number of injuries and causalities are caused by, or related to, fire incidents in ground vehicles [41, 42]. Due to the very fast evolution of fire incidents within vehicles and their complicated confined space, understanding the development and propagation of the flame front is of critical importance for safety concerns. In support of this, a project funded by the U.S. Army Research Lab aimed to study the evolution of quickly evolving flames within ground vehicles by simulating fire events within a ground vehicle testbed. Figure 1.1 shows the testbed that contained the large, turbulent flames that were visualized in this work. However, to fully characterize the flames in this scenario,

time-resolved 3D measurements were required. This work is part of an ongoing campaign with the Army Research Lab to better understand the volatile flames encountered in these dangerous vehicle fire scenarios, with the goal of informing the design and development of automated fire extinguishing systems.

1.2. Objectives and Contributions

Based on the challenges described in reducing the large computational cost of CT, as well as obtaining multi-dimensional flame measurements under field conditions, the motivation of this dissertation is twofold: first is the development and analysis of two improved algorithms for tomography to reduce computational cost while maintaining or improving accuracy, and second is the demonstration of an integrated sensor design to improve data acquisition and reduce the experimental setup footprint for large-scale combustion measurements.

In Chapter 2, an adaptive spatial discretization (ASD) technique was developed as a method of reducing the computational resources required to perform CT, while also offering the capability to improve spatial resolution. In highly turbulent flames, there may be regions where the spatial gradient of the signal intensity (e.g., LIF, chemiluminescence, or other forms of signal generation from the flame) does not change greatly. These regions in space do not require as fine a spatial discretization when reconstructing as regions with larger spatial gradients to achieve a similar level of accuracy. The ASD technique identifies regions with high and low spatial gradients by first performing a preliminary reconstruction using a coarse discretization throughout the measurement volume. Regions with large spatial gradients are deemed as regions of interest and are treated with a finer discretization and the reconstruction is completed over the mixed-discretized mesh. This technique is validated by a phantom study that uses six different known signal distributions that allow for direct comparison of results.

Chapter 3 describes a 3D reconstruction technique called the pixel masking method, which is analyzed and validated against the traditional method of reconstruction without the use of masking. The goal of the pixel masking method is to reduce the computational requirements of the reconstruction process while maintaining reconstruction accuracy by omitting voxels that contribute to pixels with no flame signal. Based on the estimated error

in the camera view angle, a buffer region was implemented around regions of the expected flame signal to ensure that these regions would not be unintentionally masked. The validation of this technique was enabled by the use of simultaneous 2D planar and 3D volumetric laser-induced fluorescence (LIF) measurements of a turbulent jet flame. The planar LIF (PLIF) measurements were taken to be the ground truth, as PLIF is a well-established technique in laser diagnostics. The volumetric LIF (VLIF) measurements were used to generate a 3D reconstruction of the flame using CT. For comparison, a cross-section of the reconstruction was compared to the corresponding PLIF measurement taken at the same plane. In addition to flame contour length, the thickness of the CH layer was measured and compared between the PLIF and VLIF measurements.

In Chapter 4, an integrated sensor design was developed as a proof-of-concept to enable large-scale flame visualization within a ground vehicle testbed under field conditions. The sensor collected data using a 9-to-1 FBE with integrated lenses in conjunction with a single camera, and was capable of acquiring projections from nine different orientations simultaneously. Data was collected for two flame conditions: a smaller propane torch flame, and a larger jet fuel pool flame. 4D flame measurements were obtained from this data using a CT algorithm to solve for an instantaneous reconstruction of the flame signal for each time-resolved frame. Due to the large uncertainty in the view angle for each FBE input, an iterative process was used to optimize the view angles during reconstruction. The time-resolved 3D measurements were combined to visualize and analyze the evolution of 3D flame structures over time, including velocity calculations of specific flame features, as well as the temporal evolution of the estimated flame surface area.

Chapter 5 includes a summary of the dissertation and its contributions to the field of combustion measurements and emission tomography. Additionally, future research possibilities are discussed that may expand on the work described in this dissertation.

Finally, Appendix A outlines additional related research efforts that have been explored and require additional work or are beyond the scope of this dissertation. First, A.1 describes the implementation of the integrated FBE-based sensor design, which was successfully used for flame visualization within the ground vehicle testbed, to visualize a

simulated Mach 5 scramjet flame within UVA's Hypersonics Research Complex. Next, A.2 describes an alternative approach to ASD, where regions of large gradients within the measured projections were used to inform which regions in the measurement volume would be treated with a finer discretization. Finally, A.3 describes an application of CT using proper orthogonal decomposition (POD), where the projections were used to iteratively solve for the scalar amplitudes of 3D eigenvector modes (obtained by applying POD on a large training set), as opposed to solving for each individual voxel within the measurement volume.

A summary of the main contributions of this dissertation are as follows:

1) The ASD technique was developed that was able to identify regions of large spatial gradients within a reconstruction volume with no *a priori* information. This information was used to generate a mixed discretization where regions of high and low spatial gradients were treated with fine and coarse discretization, respectively. In this way, the total number of voxels solved could be reduced, and computational time and memory requirements were saved without a loss in accuracy, and even a gain in spatial resolution in some cases.

2) A pixel masking method was analyzed and validated using a direct comparison of PLIF and VLIF measurements. The flame front contour length and thickness of the CH layer were calculated and compared. The method's accuracy was improved by implementing a buffer region based on the estimated error in view orientations.

3) A proof-of-concept sensor setup based on FBEs and a single camera was designed and implemented that enabled multi-dimensional (time-resolved 3D) visualization and analysis of large-scale fire events within a ground vehicle testbed under field conditions. Computed tomography was used to estimate the emission distribution and the time evolution of key flame features and surface area were calculated.

Chapter 2

2. Development of an Adaptive Spatial Discretization Technique

A subset of this work has been submitted to *Helyon* under the title "Adaptive Spatial Discretization for Volumetric Emission Tomography" at the time of writing.

Abstract

This chapter describes a new tomography technique to significantly reduce computational costs while maintaining reconstruction accuracy by applying an adaptive spatial discretization (ASD) within a 3D measurement volume. The ASD technique determines regions of high interest within the measurement volume with minimal computational resources by identifying regions with large spatial gradients in a preliminary coarse reconstruction. Then it applies a finer discretization to only the regions of high interest, allowing for a reduction in overall computational costs without sacrificing accuracy in important regions. A variety of phantom studies were performed to validate the technique and quantify the reconstruction accuracy and reduction in computational time. The results showed that this application of ASD yielded a reduction in computational time of up to 50%, while the reconstruction error increased by no more than 0.21% across six phantom cases. Through another set of phantom tests, where a high-resolution phantom is reconstructed with a limiting number of camera pixels, it was found that the ASD technique not only reduced computational time but could also improve the accuracy and spatial resolution under this more realistic scenario.

2.1. Introduction

While CT has become an indispensable tool for non-invasive imagining, the ever-increasing need for more data and higher-resolution reconstructions has motivated the development of improved tomography algorithms. Many methods have been developed in the past to reduce the computational cost of tomography while maintaining reconstruction accuracy and resolution [27]. As an example, masking methods can reduce the size of the measurement volume to be reconstructed by limiting the reconstruction to regions only where the signal level is high enough (compared to the noise level) and are discussed further in Chapter 3 [43, 44]. The inclusion of *a priori* information has also been shown to improve reconstruction times, although prior information is not always available [45]. In some cases, large datasets from a particular setup have been collected and analyzed that can better inform future reconstruction through the use of machine learning or other techniques like proper orthogonal decomposition (discussed further in Appendix A.3) [46-48].

Non-uniform discretization schemes have been used in many cases to improve the spatial resolution of tomography or reduce the inversion problem to a manageable size. In these schemes, the discretization of the measurement volume may differ throughout, with a finer discretization used only in regions that require higher spatial resolution. Adaptive meshes have been used in electrical capacitance and electrical impedance tomography, although their implementation has primarily been 2D and is limited to soft-field tomography and may not apply to other forms of emission tomography [49, 50]. An adaptive hybrid mesh has been used in chemical species tomography, although this work also focuses on a 2D measurement domain and the mesh was determined prior to tomographic reconstruction based on the location of the laser arrangement [51]. Similarly, prior information based on previous measurements or estimates of regions that would benefit from a finer discretization has been used to inform an adaptive discretization in biomedical tomography [52, 53]. Previous work has also mainly focused on using adaptive discretization techniques to improve spatial resolution without quantifying the reductions in computational cost, if any.

Based on the previous work, this work demonstrated an adaptive spatial discretization (ASD) technique for tomography within a 3D measurement volume. Compared to past efforts, the main contributions are twofold. First, the ASD technique determines the regions of high interest based on the raw signal distribution and a preliminary reconstruction with a coarse mesh. The regions of interest are defined as those that contain large spatial gradients in the reconstructed signal and require higher resolution to reconstruct accurately. The results have shown that this technique required only minimal computational cost and yet effectively determined the regions of interest. A finer discretization is then applied to only the regions of interest while the remaining regions maintain the coarse discretization. The second main contribution is that this technique involves no use of *a priori* information, demonstrating its strength and flexibility for use across many tomography problems. The use of *a priori* information can be problem-specific because different problems are governed by different physical laws. The technique developed in this work can be applied to many forms of tomography in conjunction with various reconstruction algorithms. The limitations in the current implementation of the ASD technique, as well as ongoing efforts, are outlined toward the end of this chapter.

2.2. Mathematical Formulation of Tomography

This section briefly describes the mathematical formulation of the tomographic reconstruction algorithm used in this work. Under the typical formulation, the measurement volume is discretized into equal-sized voxels whose signal is captured by camera projections. Figure 2.1 shows this formulation as a schematic of the relationship between the discretized measurement volume and the measured projections. Based on this schematic, the mathematical formulation of the tomography problem is shown in Equation 2.1 [30]:

$$P(x_P, y_P) = \sum_{x_F}^{N_x} \sum_{y_F}^{N_y} \sum_{z_F}^{N_z} F(x_F, y_F, z_F) \cdot PSF(x_F, y_F, z_F; \ x_P, y_P) . \qquad (2.1)$$

Here, $P(x_P, y_P)$ represents the signal captured on a pixel located at position (x_P, y_P) under a Cartesian coordinate system on the camera. $F(x_F, y_F, z_F)$ represents the concentration of

the
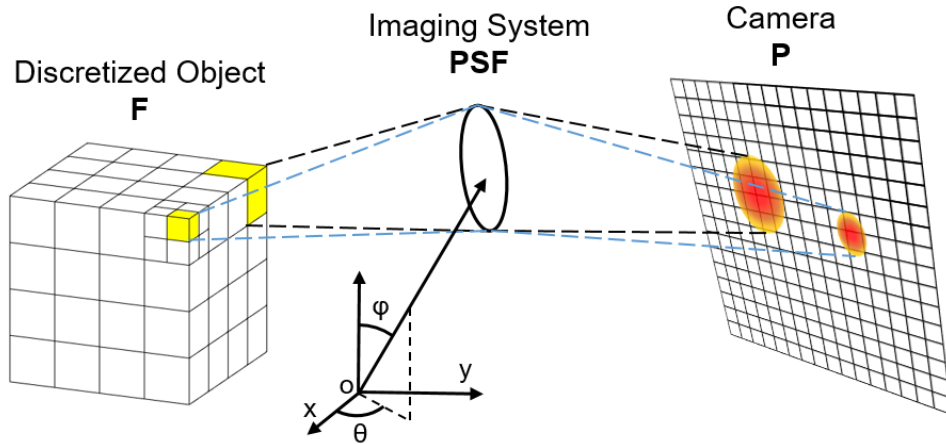
Figure 2.1: Mathematical formulation of tomography, showing the contribution of a coarse and fine voxel to a measured projection, with the smaller voxel contributing to fewer pixels

emission signal within a voxel at location (x_F, y_F, z_F) within the measurement volume. PSF is the point spread function, which represents the contribution of a voxel located at (x_F, y_F, z_F) on the pixel (x_P, y_P), and is dependent on the imaging system. In summary, the signal value on pixel (x_P, y_P) is the weighted summation of all voxels that contribute to this pixel. The measured projections are used as inputs in Eq. 2.1 and the discretized concentrations of F are solved.

As seen in Eq. 2.1, PSF has a number of elements equal to the product of the lengths of P and F, which can lead to very large computational and memory requirements in practice when many views are used. While PSF is typically sparse because many voxels do not contribute to all pixels (especially when the target is within or near the focal plane), the storage requirements of PSF, as well as the projections and the reconstruction, are still quite large, e.g. on the order of gigabytes [31].

When generating PSF, there are often many assumptions and simplifications to be made about the behavior of photons. In this work, PSF is generated using geometrical optics, meaning that photons behave as rays, moving only in straight lines, and the wave nature of light is neglected [54]. This approximation may be acceptable when the wavelength of light is significantly smaller than the spatial structures with which it interacts, which ultimately limits the spatial resolution that is achievable with this

approximation [55]. Based on this assumption, this work uses a lens-imaging model based on a single-lens approximation to generate PSF, where the straight paths of rays are traced and their location on the camera lenses are calculated based on ideal-lens optics. An alternative Monte Carlo method has been used occasionally throughout the production of this work, where many individual photons are generated at each voxel and their paths are traced, but will not be reported on in this work due to the significant increase in computational costs required for this statistical technique [30].

Another key assumption under this formulation is that the concentration of a particular voxel does not affect the path of photons passing through it. For this reason, this is a linear formulation and does not account for any beam-steering effects due to the varying gradients in refractivity that are typically measured using background-oriented schlieren [56], or multiple scattering effects [57]. Additionally, the generation of PSF in this work was based on geometrical optics and does not consider the wave nature of light. For these reasons, PSF depends only on the imaging system (i.e. the lens and camera parameters and orientations) and is completely determined prior to reconstruction. Thus, Eq. 2.1 can be solved purely as a system of linear equations, as opposed to a system of partial differential equations for nonlinear problems [58].

The linear nature of the tomography problem allows for a variety of solution algorithms, however, this work will focus on the algebraic reconstruction technique (ART) due to its simplicity, which allows for straightforward illustration of the newly developed techniques [22, 32, 59]. In every iteration of ART, each voxel is updated a number of times equal to the number of pixels to which it contributes. The formulation of ART in Equation 2.2 shows the updated voxel value F of the jth voxel (when the pixels and voxels are notated in vector format) after iteration $k + 1$ from the ith pixel:

$$F_j^{k+1} = F_j^k + \beta \frac{P_i - \sum_{j \in N_i} PSF_{i,j} F_j^k}{\sum_{j \in N_i} PSF_{i,j}^2}. \tag{2.2}$$

Here, β is a relaxation factor that promotes convergence under conditions with noise or measurement uncertainty and is typically a value less than 1 (although ART is stable with β between 0 and 2). The term $\sum_{j \in N_i} PSF_{i,j} F_j^k$ represents the projection of all the reconstructed voxels during iteration k that contribute to the pixel i (called the re-

projection), P_i is the measured projection at this same pixel, and N_i is the total number of voxels that contribute to pixel i. ART adds the difference between the measured projection and the current re-projection to the current voxel value of F, normalized by the denominator $\sum_{j \in N_i} PSF_{i,j}^2$. In this way, the error between the measured projections and re-projections is decreased over many iterations until a set number of iterations have occurred or a defined convergence criteria has been met.

2.3. Adaptive Spatial Discretization

While the main characteristics of various measurement targets can differ greatly depending on the specific field of application (e.g. medical imaging vs. turbulent flow measurements), some common features are typical to many targets. However, across many disciplines, some common features may be exploited to increase the efficiency of computed tomography. The key observation of relevance to the ASD technique is that most targets have regions within the measurement volume that contain relatively low signal or uniform features. Based on this observation, the ASD technique was developed to exploit these properties in order to reduce both the computational memory requirements and solution time for volumetric tomography while maintaining reconstruction accuracy. This is accomplished by more intelligently allocating the computational resources to regions of interest. In doing so, more and smaller voxels are used within the regions of interest while fewer larger voxels are used elsewhere, allowing the most important regions to be reconstructed with increased accuracy.

Figure 2.2 shows a flow chart outlining the steps of implementing ASD for the tests described here, as demonstrated on a 2D cross-section of a simple circular signal distribution. Step 1 of the ASD method generates a coarse mesh with a voxel size larger by a fraction of two in each dimension than what would typically be used in the tomographic reconstruction. The larger and fewer voxels require very little memory to store, and the computational time to generate the PSF is largely insignificant (on the order of seconds or less). Step 2 performs a preliminary reconstruction using the coarse mesh by iteratively solving Eq. 2.1 using the ART method shown in Eq. 2.2. The goal of this step is to broadly
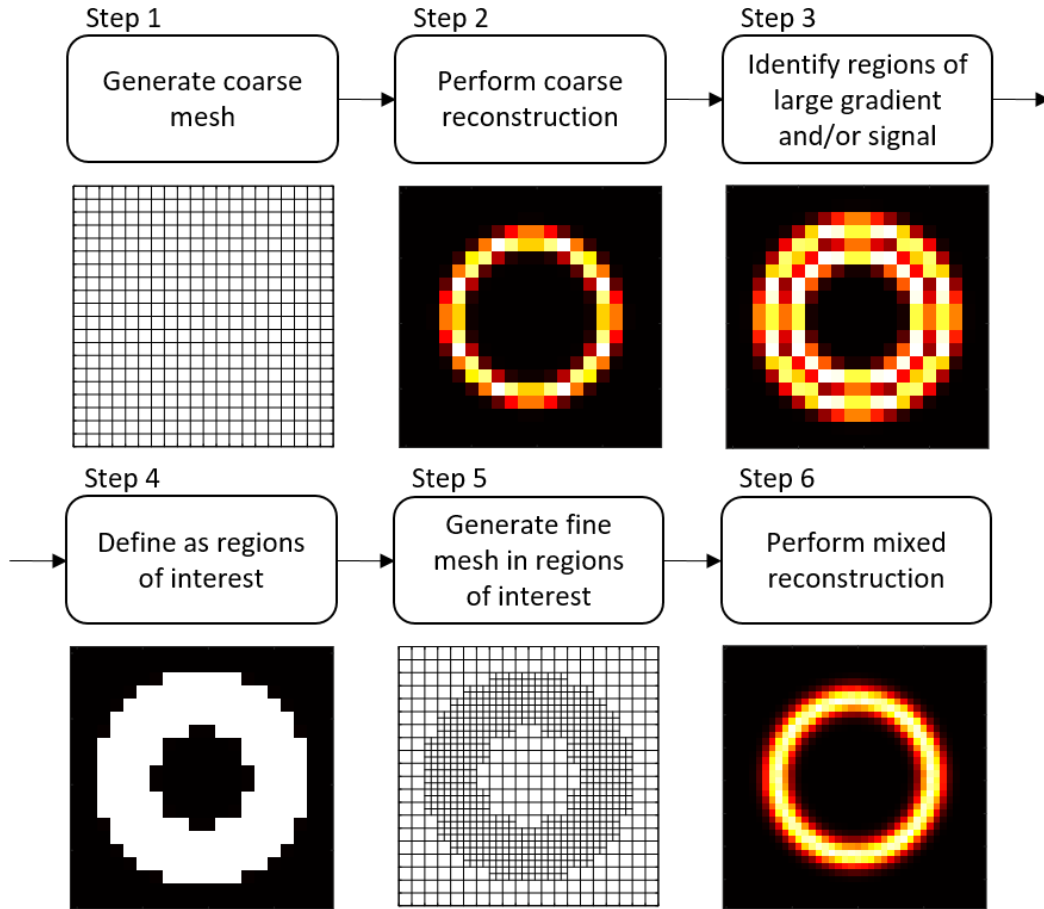
Figure 2.2: Flow chart of the ASD technique applied on a simple signal distribution, shown on a 2D cross-section

determine which regions within the measurement volume contain large signal gradients, and therefore this step does not need to be performed until a convergence criteria is reached. Typically only a few iterations are needed, thus this step can be orders of magnitude quicker than a complete baseline reconstruction. In this study, it was found that as few as five iterations could accurately identify the desired regions of interest. In Step 3, the spatial gradients of the coarse reconstruction are calculated in 3D. Depending on the noise level and the variance within the coarse reconstruction, a smoothing filter may be used to better identify regions of large gradient. In this work, a median filter was used to reduce the effects of noise on the preliminary reconstruction. Typically, a gradient threshold would be used to determine which regions require finer discretization, and the threshold may be application-dependent. For this reason, there was no set threshold used across all cases.

14

The determination of a gradient threshold will also depend on the minimum accuracy required throughout the reconstruction. Step 4 defines the regions of large gradient as regions of interest that will be treated with a fine discretization. Depending on the application, it may be desirable to also include regions with large signal (from Step 2) in addition to large gradients in the regions of interest. Step 5 replaces the coarse discretization within regions of interest with a fine discretization, where each fine voxel is half the size of a coarse voxel in each dimension. Therefore, coarse voxels within the regions of interest were replaced with eight new fine voxels within the PSF, where each fine voxel contributes to fewer pixels as shown in Fig. 2.1. An eight-to-one voxel size ratio is not the only option available, but it does make implementation significantly easier. It would be possible to use other ratios or even have multiple different tiers of regions of interest depending on the scale of the signal gradient, and this possibility is discussed later in this Chapter. Finally, Step 6 iteratively solves Eq. 2.1 using ART over the mixed-discretized volume until a set number of iterations or a convergence criterion is met.

This application of ASD results in fewer total voxels to be solved than a traditionally uniform discretization with the goal of yielding shorter computational time and smaller memory requirements. During Step 4, it is possible to identify the approximate ratio of the measurement volume to be treated as regions of interest and redefine the coarse mesh in Step 1 to optimize the total number of voxels to be approximately equal to the total number of pixels, which is the limitation imposed by the linear algebra limit when no *a priori* information is assumed [30]. This constraint can be broadly interpreted as the information that can be reconstructed (the total number of voxels) cannot exceed the information obtained by the projections (the number of pixels). While the primary focus of this chapter is on implementing ASD as a means of reducing computational costs while maintaining reconstruction accuracy, the use of ASD to improve spatial resolution is also briefly explored.

2.4. Phantom Study Results and Analysis

This section reports on the numerical validation of the ASD technique through phantom simulations using six different phantoms to emulate a wide range of different
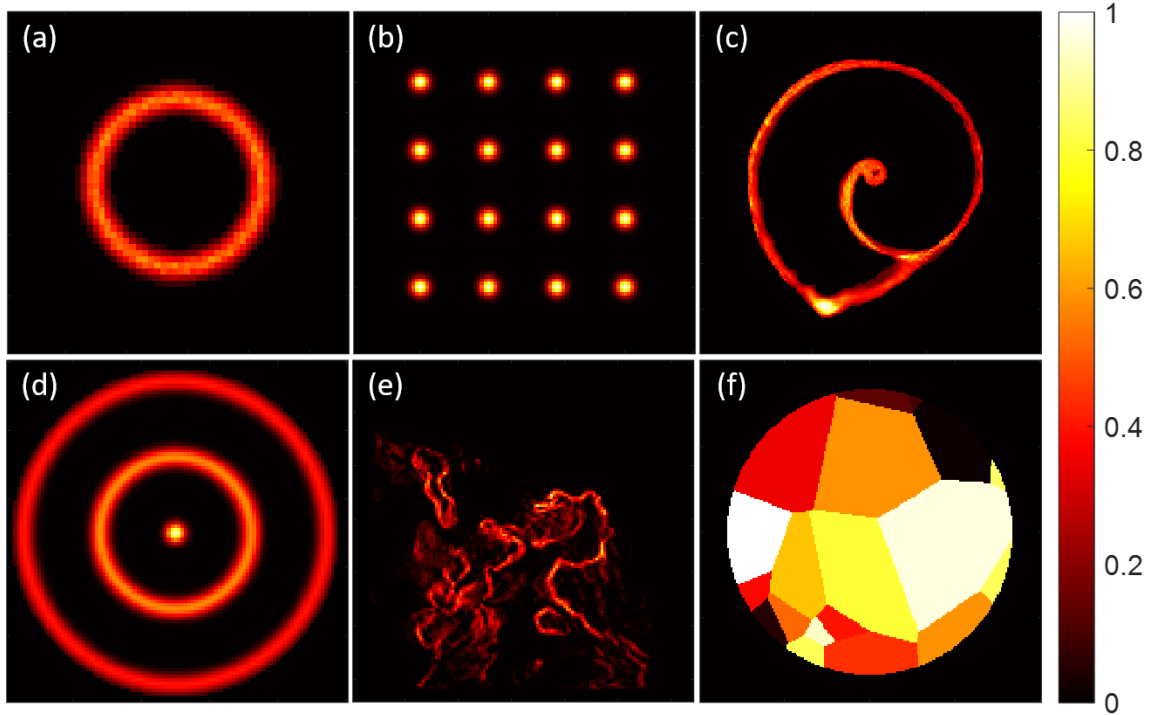
Figure 2.3: Central cross-sections of the six phantoms used in this study: a) cone flame, b) Gaussian points, c) seashell, d) concentric sinusoid, e) turbulent flame, and f) random uniform regions

signal distributions that may be encountered during tomography research and application. In a phantom study, simulated projections of known 3D distributions are obtained through the forward projection step of a tomography algorithm. These simulated projections typically include artificial noise such that the tomographic inversion process is not identical to the forward projection step, while also more closely simulating real-world conditions. The noisy simulated projections are then used as inputs of the tomography algorithm to test a new computational technique, and the resulting 3D reconstruction can be directly compared to a phantom to quantify and validate the technique [20, 32, 60].

Figure 2.3 shows central cross-sections of the six phantom cases 1-6 (2.3a-2.3f), all of which are three-dimensional and of various sizes, and also whose signal distributions have been normalized. Figure 2.3a is of an experimentally obtained cone flame with voxel dimensions (56×56×192), 2.3b is of 16 uniformly distributed Gaussian spheres with dimensions (100×100×20), 2.3c is a seashell cross-section obtained from reconstructions of x-ray images taken by [61] and has dimensions (150×150×20), 2.3d is of a concentric
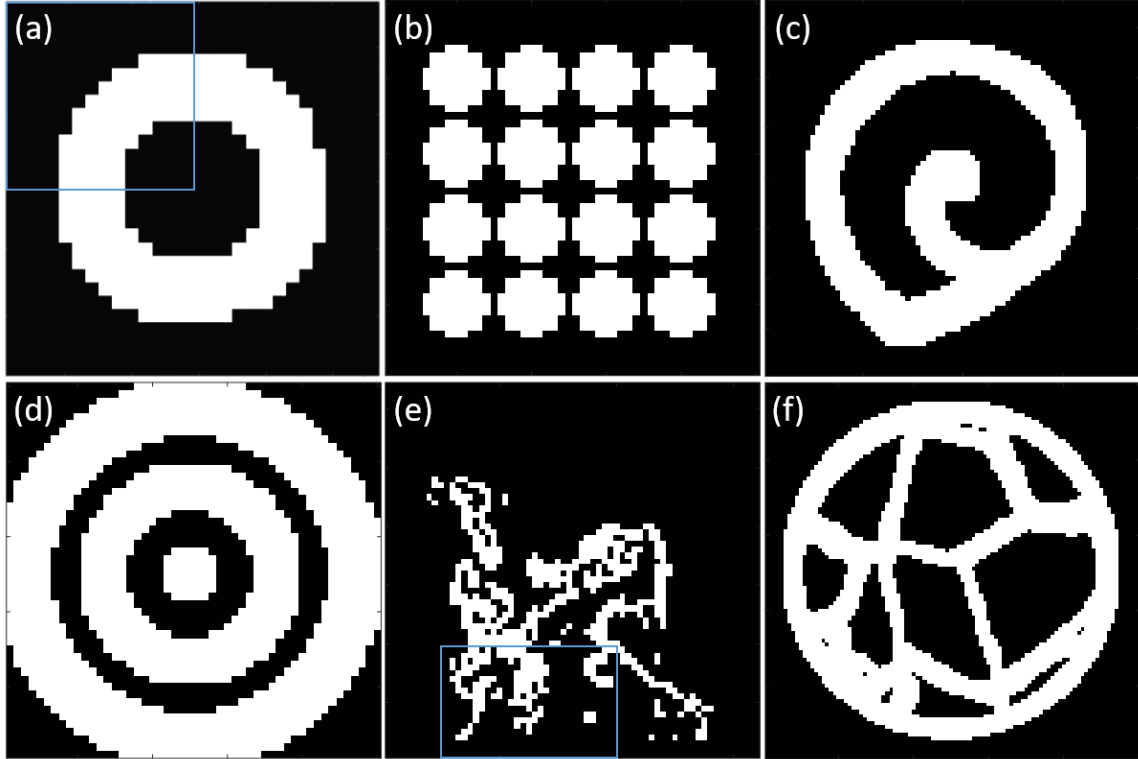
Figure 2.4: Central cross-sections after the preliminary reconstruction for each of the six phantoms, showing the regions of interest highlighted in white that will be treated with finer discretization

sinusoid and has dimensions ($100 \times 100 \times 20$), 2.3e is of a turbulent flame reconstructed from VLIF images taken by [62] and has dimensions ($128 \times 30 \times 128$), and finally 2.3f is of a random distribution of uniform regions and has dimensions ($200 \times 200 \times 20$). Each of the phantoms (except the sixth, 2.3f) was not uniform in the depth-wise dimension. For instance, the seashell has a twist as it increases in depth, and the turbulent flame has significant complexity in the depth-wise direction. However, in each case, the phantoms were relatively thin in one dimension compared to the others. This is because, due to the co-planar arrangement of the 18 views, there was not much coupling between regions that were significantly distant in depth. Therefore, no substantial information would be gained by examining larger phantoms.

Figure 2.4 shows the regions of interest determined from Step 4 of ASD for each of the six phantom cases at the same central cross-sections shown in Fig. 2.3. By comparison to Fig. 2.3, it is clear that the important regions, that is, those with large spatial

17
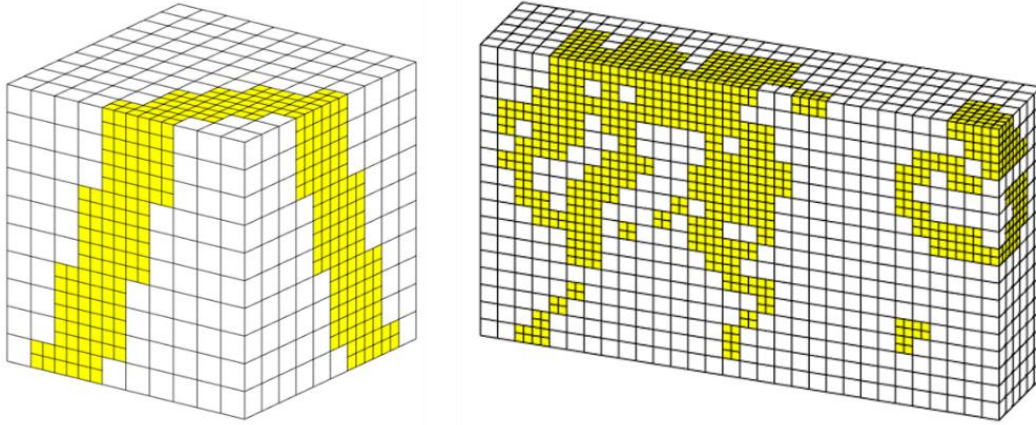
Figure 2.5: Volumetric cross-sections of the cone flame (left) and the turbulent flame (right), where regions of interest are highlighted and have been treated with a fine discretization

gradients, were accurately detected from the coarse reconstruction. In Fig. 2.4f, for example, the regions of uniform signal were not determined to be regions of interest, and a coarse discretization in these regions should offer a sufficient spatial resolution. However, ASD clearly marks out the interfaces between uniform regions of different intensities.

Figure 2.5 shows a volumetric view of the cross-sections for the cone flame (left) and the turbulent flame (right), shown in the boxed regions of Fig. 2.4a and 2.4e, where the regions of interest are highlighted. Here, these regions have been treated with fine discretization that is half the size of the coarse discretization in each dimension. As demonstrated here, the ASD technique could determine regions of interest at internal regions within the measurement objects, something which would not be possible if using the projections alone. Additionally, it should be noted that the thicknesses of the regions of interest seen in Figs. 2.4 and 2.5 are typically thicker than the regions of signal. This is first because the gradient was calculated at the interface between voxels, and all voxels surrounding a large-gradient interface will be treated as regions of interest. Also, because a coarse reconstruction was used to determine the regions of interest, each marked voxel would contain eight finely discretized voxels. However, this was not considered to be a problem, as the risk of missing a key feature due to insignificant resolution was greater

18

than the small increase in computational time to include a slightly too large region of fine discretization.

To perform the numerical validation, each phantom was projected onto 18 equally-spaced co-planar views with 3% Gaussian noise artificially added. The number of views used in this study was chosen to be a compromise between the typical numbers of projections used across many different fields [32, 63, 64]. The 18 noisy projections were then used to reconstruct the phantom by iteratively solving the inversion problem in Eq. 2.1 using ART with and without ASD. In both cases, no regularization, *a priori* information, or other special treatment was applied to either method. The baseline reconstruction, without the use of ASD, had a discretization that was the same as the phantom, and the ASD method had a discretization such that the fine voxels were the same as the phantom and baseline. This allowed for a straightforward comparison between the phantom and the reconstructions. Across the six phantoms, the amounts of the measurement volume that were determined to be regions of interest, and thus treated with fine discretization, ranged from 14.2% (Case 1) to 37.2% (Case 4). With a voxel size ratio of 1-to-8 between coarse and fine voxels, the mixed meshes had between 24.9% and 45.1% of the total number of voxels as the baseline, respectively.

Figure 2.6 shows a comparison of the results between the baseline and ASD methods of reconstruction for the six phantom cases, showing the computational time required to perform the reconstruction. As a reference for computational time, all computations were performed on a single core of a 2.20 GHz Inter Xeon E5-2650 v4 processor. In each case, the ASD method required only approximately half the computational time as the baseline method, indicating that a large portion of the measurement volume was treated with a coarse discretization. Reconstructions were performed for the same number of iterations for the baseline and ASD methods, and the number of iterations was set such that the reconstruction was at or near convergence for both methods [65]. However, it was also found that there was no significant difference in time to reach a set level of convergence between both methods. Under these conditions, the size of the PSF was the primary contributor towards computation time, which depends on the number of pixel contributions from each voxel, as well as the total number of voxels.
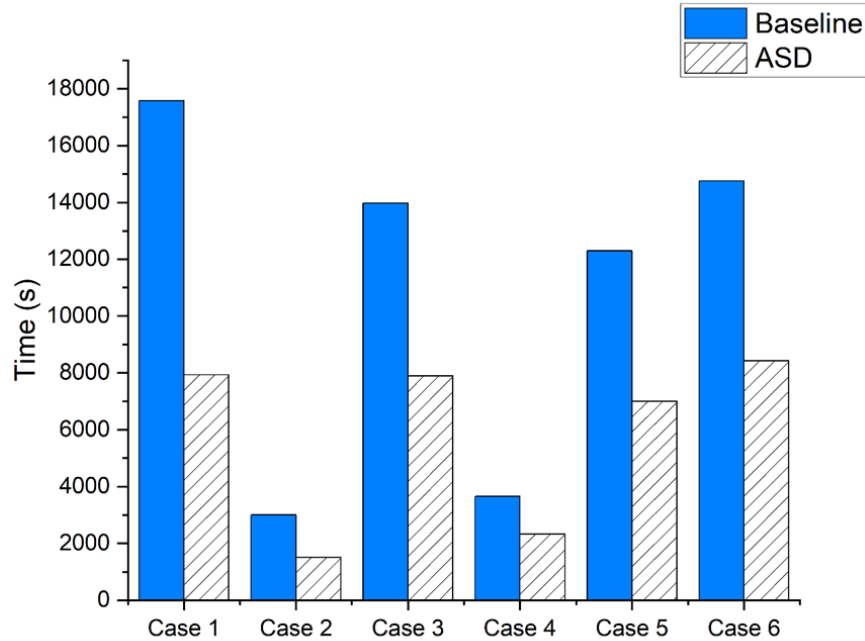
Figure 2.6: Comparison of the total computational time for the baseline and ASD methods across the six phantom cases

Because a single coarse voxel contributes to nearly as many pixels as eight fine voxels (due to its larger size), the maximum reduction in computational time using ASD is only slightly greater than 50%. This can be seen in Case 1, where the total number of voxels using ASD was 24.9% that of the baseline, but the reduction in computational time was 54.9%. The smallest decrease in computation time was 36.1% in Case 4, where just less than half the measurement volume was treated with a fine discretization. While in general it is possible to use a different voxel size ratio for the coarse and fine discretization, such as 1-to-27 (when a fine voxel is one-third the size of a coarse voxel in each dimension), it was found that in this particular application of ASD the additional savings in computational cost were insignificant compared to the further increase in reconstruction error that the larger coarse voxels incurred.

Figure 2.7 shows the reconstruction error for each case, which was roughly the same between the baseline and ASD methods. The reconstruction error in this study was defined as the fractional difference between the phantom and the reconstruction and is defined as follows:
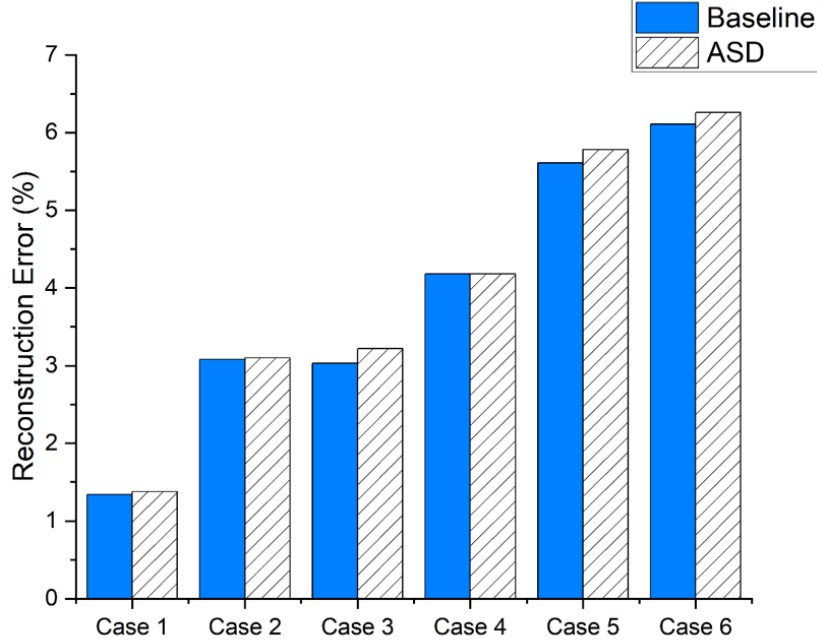
Figure 2.7: Comparison of the reconstruction error, as compared to the phantom, for the baseline and ASD methods across the six phantom cases

$$e_R = \sum_{x_F}^{N_x} \sum_{y_F}^{N_y} \sum_{z_F}^{N_z} \frac{|F(x_F, y_F, z_F) - R(x_F, y_F, z_F)|}{F(x_F, y_F, z_F)}, \tag{2.3}$$

where F is the phantom and R is the reconstructed distribution. For direct comparison of the mixed-discretized reconstruction with the phantom, each coarse voxel in the reconstruction was set to eight fine voxels of equal signal value and no interpolation was used. While the ASD method consistently had a slightly greater error (as one would expect when using fewer total voxels), the largest increase in error was only 0.21%, found in Case 3. The extremely low increase in error while requiring only about half the computational resources indicates that the ASD method was able to accurately identify the regions of importance within the measurement volume and reconstruct them with high accuracy using the same discretization as the baseline method. This demonstrates the strength of the ASD method, as well as its flexibility, as no information about the distributions nor their projections was needed before reconstruction.

While the relative error of the ASD method was not significantly different from that of the baseline, the spatial distribution of the error is of importance, as an excess
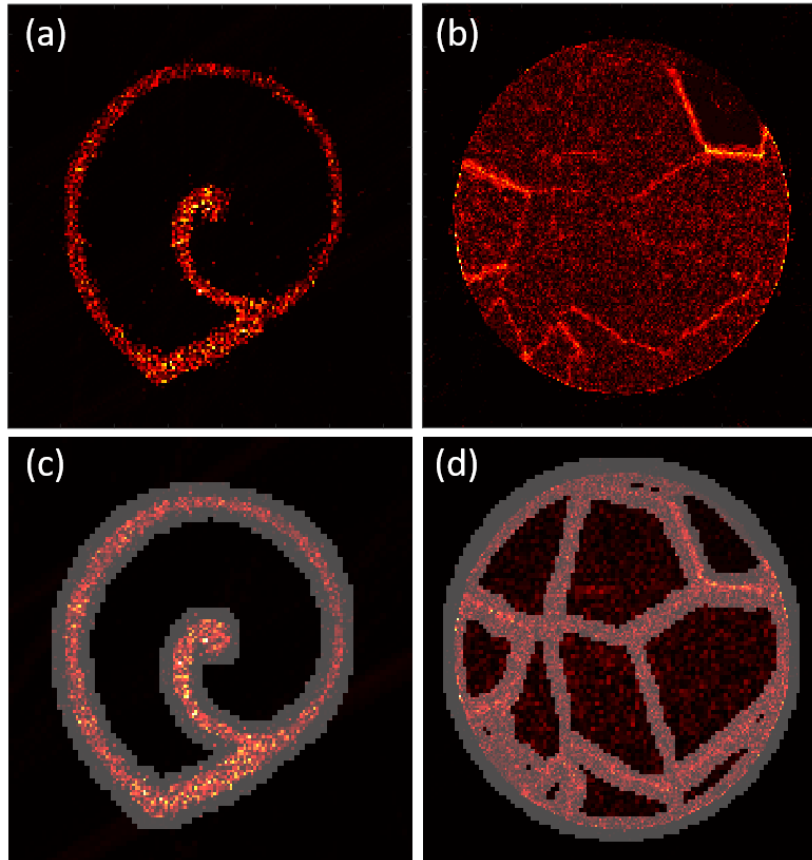
Figure 2.8: Voxel-by-voxel difference between reconstruction and phantom for a) Case 3 baseline, b) Case 6 baseline, c) Case 3 ASD, and d) Case 6 ASD, where the regions of interest are overlaid on the ASD methods

concentration of error within the regions of interest would be unfavorable. Figure 2.8 shows the spatial distribution of the difference between the reconstructions and the phantoms for two cases. Figures 2.8a and 2.8b show the cross-sections of the voxel-by-voxel difference between the reconstructions and phantoms for Cases 3 and 6, respectively, while Fig. 2.8c and 2.8d are the corresponding differences for the ASD methods, where the regions of interest shown in Fig 2.4 are overlaid with transparency. For Case 3, the error distribution was nearly identical between both methods, with the ASD method having a slightly larger error overall, as discussed previously. Unsurprisingly, neither case had a significant error in the low-signal regions. In Case 6, where the interior regions had significant but uniform signal, it was expected that error would be present throughout. Figure 2.8b shows that the highest errors for the baseline methods were localized near regions of large gradient (the

22

interfaces between uniform regions), which was a trend that is also seen in Fig. 2.8d. The largest difference between the baseline and ASD methods in Case 6 was that the errors in the regions not of interest when using ASD were less uniform, likely a consequence of the noise within the projections and the larger voxel size in these regions, although this difference did not seem to contribute greatly to the overall error within the reconstruction.

In this application of ASD, a significant decrease in computational time has been shown while maintaining reconstruction accuracy across six phantom cases. This was accomplished by reducing the total number of voxels to be computed. However, in these tests, the discretization and size of the reconstructions were the same as the phantoms and did not represent a realistic scenario. In more realistic scenarios, the reconstruction resolution achievable is limited by the amount of pixel information obtained (excluding any *a priori* information). To simulate this more realistic scenario, two phantoms (the Gaussian points and the concentric sinusoid, shown in Figs. 2.3b and 2.3d) were recreated at a much larger size of $400 \times 400 \times 20$ voxels (a total of 3.2×10^6 voxels) and projected onto the same 18 views with pixel resolution of 400×80 pixels each (a total of 5.76×10^5 pixels), thereby severely limiting the maximum achievable reconstruction resolution. Additionally, 3% Gaussian noise was added again to the phantom projections, which also limited the maximum achievable accuracy of the reconstruction. Based on the noisy phantom projections, the two phantoms were reconstructed using a variety of discretizations. The reconstructions were directly compared to the phantoms to assess the accuracy based on Eq. 2.3, where the reconstructions were up-scaled to the same number of voxels as the phantom using a bicubic interpolation, as described in Ref. [66]. This direct comparison with the phantom allowed for the accuracy of the reconstructions to be determined at a range of discretizations.

Figure 2.9 shows the results of the reconstructions for the two phantom cases, where the reconstruction error is plotted against the total number of voxels used on a log scale. The vertical red line indicates the total number of pixels used, which represents the expected maximum number of voxels that could be used to obtain the best accuracy. In both cases, the discretization of the reconstructions was the same, with a number of voxels in the horizontal direction of 60, 80, 100, 150, 200, 300, and 400. The number of voxels in

23
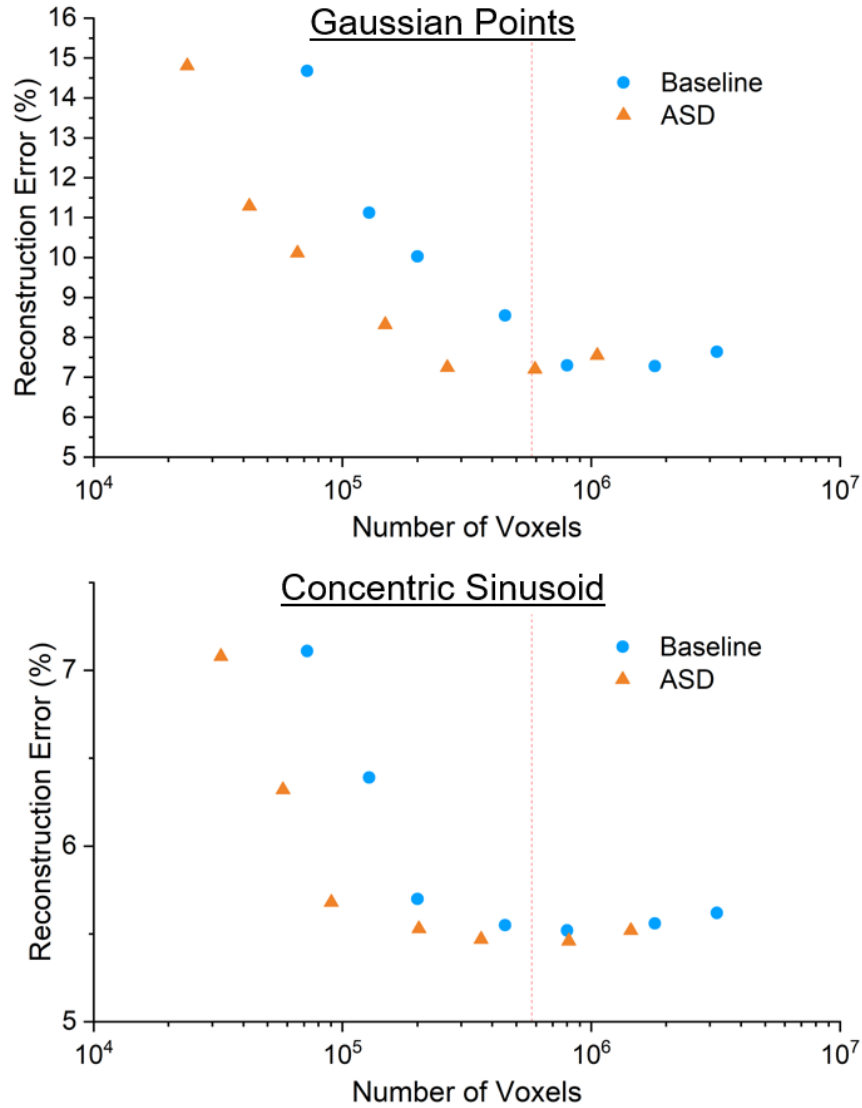
Figure 2.9: Comparison between the reconstruction errors for two phantom cases as a function of the total number of voxels used in the reconstruction for the ASD and baseline methods. The reconstructions were up-scaled and directly compared to a high-resolution phantom.

the depth direction (compared to the 20 voxels for the phantom) was scaled accordingly such that the voxels were approximately the same size in each dimension for all cases. As expected, as the total number of voxels increased, and the voxel size subsequently decreased, the error decreased. However, once the voxel count increased beyond the red dotted line, which indicates the number of pixels used as inputs for reconstruction, the error plateaued, where an increase in voxels did not yield more accurate results. This plateau

was expected because, once the total number of voxels has reached the total number of pixels, no further information could be extracted from the projections as imposed by the linear algebra limit.

A subtle yet interesting result that can be seen in Fig. 2.9 is that, beyond a plateau of reconstruction error as the number of voxels increased, there was a small increase in error with increasing voxels. The rise in error beyond the plateau point was likely due to artifacts caused by the measurement noise in the simulated projections. For example, a relatively large voxel that contributed to many different pixels would effectively take on a value equal to the average contribution from the noisy pixels. In this way, the error caused by the noise could be reduced (although this may not be the case for all sources of noise). However, for smaller voxels that contribute to fewer pixels, a singly noisy pixel may contribute greatly to the value of the contributing voxels, thereby increasing the reconstruction error.

Another interesting finding from Fig. 2.9 was that the minimum error achievable was smaller when using ASD as opposed to the baseline method, indicating that the ASD method could achieve an increase, albeit marginal, in spatial resolution. This is likely due to the ASD method making better use of the information available in the projections by more intelligently distributing the same number of voxels. Additionally, this shows that the ASD method was more resistant to noise due to the presence of larger voxels that may reduce the adverse effects of noise. It was also shown that, for both phantom cases, the ASD method could achieve the same or better accuracy than the baseline while using significantly fewer voxels. These results were also seen in the previous tests as well, indicating that the ASD method can offer improvements across different metrics under many different testing conditions. With all else held constant, the total number of voxels is typically proportional to both computational time and memory, and therefore the implementation of ASD was able to reduce overall computational cost without a loss in accuracy across different forms of implementation.

2.5. Summary

This work reports on an adaptive spatial discretization technique that exploits regions of relatively uniform or low signal within a measurement volume to make better

use of computational resources, either by reducing computational cost while maintaining accuracy or by increasing spatial resolution without increasing computational cost. The ASD technique determines regions of high interest based on the signal distribution through a preliminary reconstruction with a coarse discretization. Regions of interest are defined as those with large spatial gradients in the partially reconstructed signal, and the results show that the ASD technique effectively determined the regions of interest with minimal computational cost. Regions of interest are treated with a finer discretization while the remaining volume maintains the coarse discretization. This technique does not include any *a priori* information and can be applied to many forms of tomography and used with various solution algorithms, although this work has limited the analyses to the ART algorithm.

The advantages of ASD are demonstrated and quantified using a series of phantom studies. A total of six cases were selected for this work to represent a variety of spatial distributions. In each case, 18 simulated projections were generated with 3% Gaussian noise which were used to reconstruct the phantom using the baseline and ASD methods. Through direct comparison of the reconstruction and the phantoms, the ASD technique was able to drastically reduce computational times by up to 50% while yielding little to no increase in reconstruction error. Additionally, there was no significant change to the spatial distribution of error within the reconstructions using ASD. To simulate more realistic conditions, high-resolution phantoms of two cases were generated and projected onto the same 18 views with 3% Gaussian noise. These two cases were reconstructed using the ASD and baseline method across a range of discretizations, where it was found that the ASD method was more noise-resistant, was able to slightly increase the minimum achievable error, and simultaneously reduced the computational cost.

There are some limitations to the ASD technique in its current implementation. A generic limitation of ASD is that it requires the presence of regions with uniform or low signal within the measurement volume to be applicable. While this is often the case in many applications of tomography, this technique would be of limited value in cases where the entire target region needs the same high resolution. Another limitation in this implementation of ASD is that the measurement volume is only discretized in two sizes

(coarse and fine), and in a 1-to-8 size ratio due to the use of cubical voxels. In general, the discretization size ratios do not need to be 1-to-8, as other voxel shapes may be used. However, it was found that a 1-to-8 size ratio was superior to a 1-to-27 ratio (where each fine voxel is one-third the size of a coarse voxel in each dimension) because the extra decrease in computational cost using the finer voxels was insignificant compared to the increase in error. However, a multi-zone approach may be used with regions requiring high, medium, and low resolutions to resolve this issue which is being explored in our ongoing work. Finally, these tests were limited to phantoms with known distributions. To further test the applicability of ASD and the potential capability to increase spatial resolution, future work includes testing on real-world targets.

Chapter 3

3. Analysis of a Pixel Masking Method Using Direct Comparison of VLIF and PLIF

Abstract

This work reports the validation of a masking method to significantly reduce computational costs while maintaining the reconstruction accuracy of tomography for laser-induced fluorescence (LIF) imaging of the methylidyne radical (CH) in a turbulent CH_4-air flame. The masking method excludes from the tomographic reconstruction all regions of the measurement volume that contribute to pixel regions that contain no signal, as those regions must contain no fluorescence, thereby reducing computational costs. An additional buffer zone was implemented around the remaining voxels within the measurement volume based on the expected error in view registration to ensure that no voxels containing fluorescence were accidentally masked. This method is validated via direct comparison of simultaneous 2D planar LIF (PLIF) and 3D volumetric LIF (VLIF) measurements of highly turbulent flames within a measurement volume of 42 mm (width) $\times$ 5 mm (depth) $\times$ 42 mm (height). The flame front perimeter was calculated and directly compared between the PLIF measurement and a corresponding cross-section of a 3D reconstruction derived from the VLIF measurements. Through this comparison, it was shown that the masking method could reduce the overall computational time while simultaneously improving the reconstruction accuracy by concentrating computational resources on regions of high interest. The masking method was particularly advantageous for CH-LIF measurements as the extent of the CH radical distribution is limited to the thin flame surface, leaving a large fraction of the probed volume devoid of signal and able to be excluded from the reconstruction.

3.1. Introduction

Due to the large range of experimental conditions encountered when performing CT, different computational techniques may be better suited for different environments. For example, in the previous chapter, the ASD technique requires regions of low spatial gradients within the target signal to be applicable. For this reason, it is important to have a multitude of techniques to reduce the computational cost of CT under different circumstances by exploiting various features of flames and their measurements. This chapter reports on the validation and analysis of an alternative computational technique, called the 3D pixel masking technique, which exploits a different property than ASD to again significantly reduce the computational cost of CT while maintaining or even improving the reconstruction accuracy.

The masking technique works on the principle that all voxels that contribute to pixels containing signal below an estimated signal floor must contain no substantial emission and can be removed from the tomographic reconstruction. By reducing the number of pixels and voxels from the reconstruction, the computational cost of CT is reduced without adversely affecting reconstruction accuracy. Consequently, by removing some voxels from the reconstruction, more and smaller voxels can be used in the remaining regions of the measurement volume, offering a potential to increase spatial resolution, as previous work has shown that spatial resolution is limited by both hardware and voxel size [30]. Similar masking techniques have previously been applied in tomography using measurements from volumetric laser absorption [44], flame emission [67], background-oriented schlieren [43], and particle image velocimetry (PIV) [68], and are more broadly discussed by Grauer et al. in Ref. [27]. In each case, masking has been shown to improve reconstruction accuracy.

In this work, the pixel masking technique was validated and analyzed through direct comparison of flame front contour length calculations derived from simultaneous 2D and 3D flame measurements. The novel diagnostic setup described here, which was used prior to the work of this dissertation and is described in Refs. [62, 69], collected laser-induced fluorescence (LIF) measurements of the methylidyne radical (CH) in turbulent CH_4-air flames. The uniqueness of this setup was that it collected both 2D planar LIF (PLIF) and

3D volumetric LIF (VLIF) measurements simultaneously, which subsequently allowed for the direct comparison between these measurements and results. The VLIF measurements were used in a tomography algorithm to determine the 3D distribution of CH within the flame front, and a central cross-section that corresponded to the same location as the PLIF measurement was extracted. Thus, the flame front contour length between both 2D and 3D measurements could be directly compared and the accuracy of the VLIF reconstructions could be determined.

Based on previous work, the novelty and contribution of this work is two-fold. First, this work demonstrates the applicability of the masking technique on VLIF tomography. Second, the results in this work demonstrate that the masking technique, with an added buffer region to compensate for estimated errors in view registration, is particularly well-suited for VLIF measurements of the CH radical, as this species exists only within a thin layer representing the flame front [70]. Therefore, a larger portion of the measurement volume may be masked, saving computational resources while simultaneously allowing for an increase in the spatial resolution of the reconstruction.

The effectiveness of the masking method was assessed and validated by direct comparison of cross-sectional flame-contour lengths obtained from 3D tomographic measurements against 2D planar laser-induced fluorescence (PLIF) measurements of the methylidyne radical (CH). PLIF is a well-established technique for obtaining 2D flame measurements [71, 72]. In past works, PLIF has been extended into volumetric LIF (VLIF), and instantaneous 3D flame measurements from multiple cameras were demonstrated [28, 69, 73]. The VLIF measurements are used in the CT algorithm to calculate the 3D distribution of the fluorescence within the flame. The flame-contour length was then calculated at the central cross-section of the VLIF reconstruction that corresponds to the same regions as the PLIF measurement. Such datasets provide a way to directly assess the accuracy of the 3D masking technique. The PLIF measurements, which were an integrated signal over the thickness of a thin laser sheet, were accepted to be the "ground truth", as these measurements have well-established accuracy. The accuracy of the VLIF measurements was obtained by direct comparison of the flame-contour length to the PLIF results. This method of comparison has been previously demonstrated in Ref. [69] and

allowed for the validation and analysis of the masking technique in this work. Under this comparison, the reconstruction accuracy and computational time could be compared with and without the use of masking. While a similar masking technique was used by Ma et al. in Ref. [28], this work implemented a buffer region and validated the technique using a direct comparison between 2D PLIF and simultaneous 3D VLIF measurements. Additionally, the masking technique demonstrated the ability to achieve better accuracy in flame-contour length measurements described in this work. While the masking technique described here has been implemented in the context of combustion tomography, it can easily be adapted to other forms of tomography as well.

3.2. Experimental Arrangement for VLIF and PLIF

The experimental data used for analysis in this chapter was previously generated and the experimental arrangement has been presented in Ref. [62, 69]. Nevertheless, the setup and methods are described in this section for informational purposes and to motivate the computational improvements described in the remainder of the chapter. The experimental setup was designed to enable simultaneous imaging of both PLIF and VLIF measurements from a highly turbulent flame. Figure 3.1, adapted from Ref. [69], shows a schematic of the experimental setup and can be divided into three systems: the burner, the laser system and related optics, and the imaging system. The Hi-Pilot burner, a turbulent premixed Bunsen-type burner, was used to generate the experimental data presented in this work, which are of CH_4-air flames.

The flames studied in this work are denoted as Case 3B-1.05, 3 being the case number, B being the type of slotted plate used to induce turbulence, and 1.05 being the fuel-air equivalence ratio, in Ref. [62]. In this case, the equivalence ratio of $\phi = 1.05$ indicated that the combustion is fuel-rich ($\phi > 1$) and will yield slightly incomplete combustion [74, 75]. Under these flow conditions, the flame was described as having a ratio of turbulence intensity to laminar burning velocity of $u'/S_L = 16$, and a turbulent Reynolds number of $Re_T = 4200$. Of most concern to this work, however, are the length scales that are present in the turbulent reactive flow. Based on the data and equations found in Ref. [62], the integral length scale under these conditions was 9.2 mm, indicating the

Figure 3.1: Schematic of the experimental arrangement to capture simultaneous PLIF and VLIF flame measurements, originally published in Ref. [69]

largest spatial structures in the flow. The Taylor microscale (the turbulence length scale) was estimated to be about 1.3 mm and indicates the scale at which eddies begin to dissipate as heat. Finally, the Kolmogorov length scale was estimated to be 0.06 mm, indicating the smallest-scale eddies in the turbulent flow. Finally, the laminar reaction layer thickness for CH was measured to be 0.36 mm and ultimately sets a limit on the smallest scales that can be resolved using CH measurements, as in this work.

The laser system was operated at a frequency of 10 Hz (10 laser pulses per second) and was composed of a Nd:YAG pump laser, a dye laser operating with Luxottica (Exciton) DCM dye dissolved in methanol, and a frequency control unit (FCU). The goal of the multiple laser components was to generate UV pulses with a wavelength of 314.315 nm. This particular wavelength of light excites the $Q_2(2)$ and $Q_2(6)$ transitions of the $C^2\Sigma^+ - X^2\Pi(v' = 0, v'' = 0)$ band of methylidyne (CH) radicals that are a byproduct of the methane-air combustion [76]. This wavelength provided relatively good signal strength for CH detection with low laser fluence levels while simultaneously isolating the CH signal from those of other chemical species.

The generated UV beam was split into two components using a simple wedged window, creating a strong beam with energy of about 10 mJ/pulse for the VLIF measurement and a weak beam with about 0.5 mJ/pulse for the PLIF measurement. The collimated VLIF laser slab was created by expanding the strong laser beam with a pair of spherical lenses (-50 mm and 750 mm focal lengths); a pair of right-angle "tools" were used to "define" the desired slab width of 5 mm. Note that the 5 mm thick slab is thinner than the width of the burner output. For the weak beam, a set of mirrors was used to delay the laser pulse by about 45 ns relative to the VLIF pulse, as indicated in Fig. 3.1. This time delay (45 ns) was short relative to any flow time scales but large enough to separate the PLIF and VLIF signals via the intensifier-gate timing. For instance, in Case 3B-1.05, the centerline velocity was measured to be 21 m/s, meaning the bulk flow would have moved only approximately 0.9 μm, which is about 40 times smaller than the projected width of a pixel. Similarly, given that each beam duration was about 8 ns long, and the lifetimes of the $C^2\Sigma^+$ states of CH are around 4 ns [77], a 45 ns delay is sufficient to ensure no overlap in PLIF and VLIF signals. The PLIF laser sheet was then formed with a -100 mm focal length plano-concave cylindrical lens and a 1 m focal length spherical lens, to create a 0.17 mm-thick sheet collimated in the vertical direction. As indicated in Fig. 3.1, the PLIF and VLIF beams were separated by a small distance and then overlapped in the probe region (having the PLIF sheet centered within the VLIF slab) by having a small angle of about 3 degrees between their propagation vectors.

Arranged around the burner were six intensified cameras (all with gate times equaling 100 ns), each equipped with a UV lens (100 mm, f/2.8 Cerco lens fitted with a Scott-glass UG-5 filter), with resolutions of 1024 × 1024 pixels. In Fig. 3.1, cameras 1 through 5 were used to capture the VLIF signal, and camera 6 was used to capture the PLIF signal. Figure 3.1 also shows the coordinate system used, where X was the direction of laser sheet propagation, Y was the direction perpendicular to the laser sheet propagation direction, and Z was in the vertical direction, aligned with the direction of the flow. All six cameras were aligned in a coplanar arrangement (in the X – Y plane) around the burner, and thus their positions were completely specified by their angular position θ relative to the Y-axis and their radial distance from the burner origin (kept approximately equal for all cameras). Before any measurements, a calibration target was placed at the expected
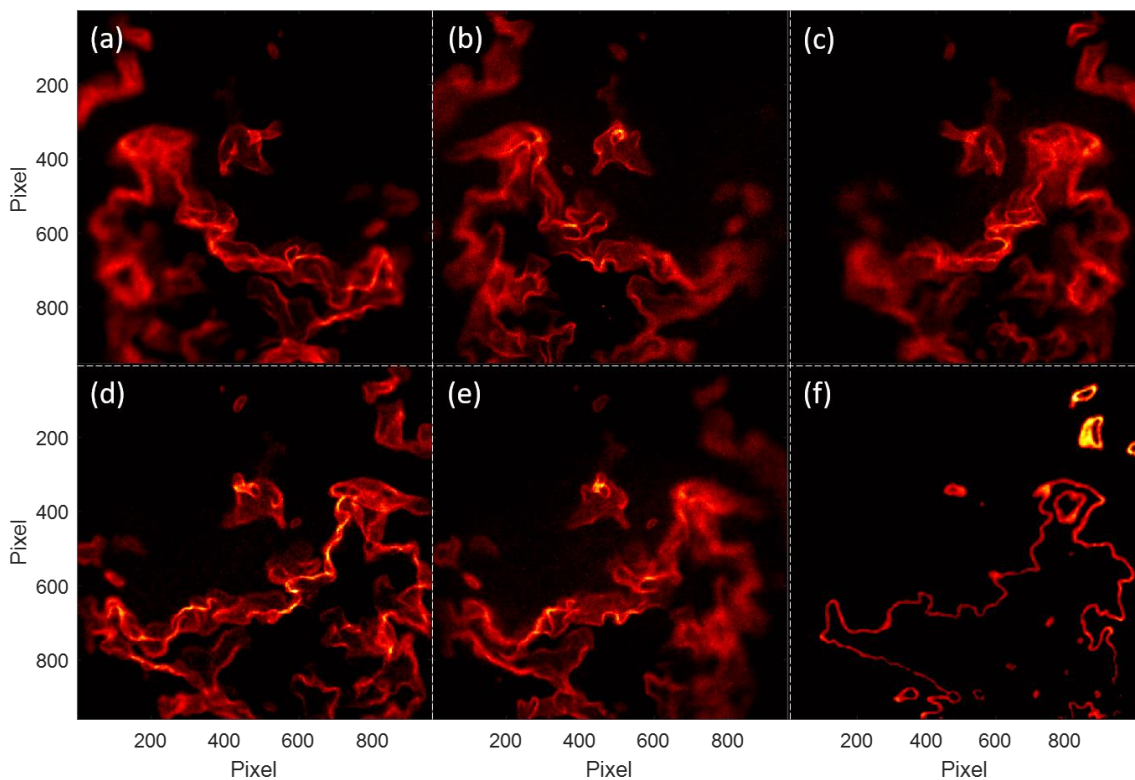
Figure 3.2: Set of projections measured by cameras 1 through 6. Panels (a)-(e) are the VLIF projections measured by cameras 1-5, and panel (f) is the PLIF measurement captured by camera 6

location of the flame to determine the orientation of each camera using a view registration program [78]. The positions of cameras 1 through 6 were found to be 37.7°, 146.9°, 183.4°, 210.5°, 336.4°, and 0.5°, respectively, with an estimated uncertainty of ±0.5°.

Figure 3.2 shows a sample of instantaneous VLIF and PLIF measurements (a single frame) collected from all six cameras. In each frame, an ensemble-averaged background image was subtracted from each instantaneous image. Figures 3.2a–e show the measured VLIF projections simultaneously captured on cameras 1-5. These images show a clear 3D structure of the flames, as one would expect from the volumetric VLIF illumination. Figure 3.2f shows a PLIF measurement captured on camera 6 at essentially the same time, which is clearly planar in nature. Using the five VLIF projections, a tomographic reconstruction was performed to generate a 3D reconstruction of the VLIF signal, which is representative of the relative CH concentration within the illuminated region of the flame. For this study,

the CH radical was chosen as the target species because it is produced near the flame's principal heat release region and is thus a good proxy of the flame front [72, 79]. Additionally, because CH only exists within the thin flame front layer, the masking method covered in this work is especially effective in treating CH-VLIF projections.

As seen in Fig. 3.2a-e, there is a significant portion of each projection that contains little to no fluorescence signal, both inside and outside the flame regions. Traditionally, these regions would be iterated over and solved in the tomography algorithm without special treatment. However, the masking method described in this work will exclude those pixels, as well as all voxels contributing to those pixels, from the reconstruction to dramatically reduce computational cost. Figure 3.2f reinforces this insight by showing that, in a cross-section of a turbulent flame ($u'/S_L = 16$), only a very small portion contains CH fluorescence signal. It is worth noting that the exact degree of reduction to computational cost depends on the specific flame conditions (e.g. what fraction of the measurement volume contains signal) and can vary considerably from one exposure to the next, but some degree of reduction has been achieved in all the frames studied here.

3.3. Methods and Problem Formulation of Masking

This section only briefly reviews the mathematical formulation of the tomographic reconstruction algorithm as it was covered in more detail in Chapter 2. This section also describes the masking method and its implementation. The mathematical formulation shown in Eq. 2.1 can be rewritten in vector form for simplicity as follows:

$$\boldsymbol{P} = \boldsymbol{PSF} \cdot \boldsymbol{F}, \tag{3.1}$$

where $\boldsymbol{P}$ is the projection vector composed of all the pixels on all the cameras, $\boldsymbol{F}$ is the 3D distribution of the VLIF signal in vector for that is to be solved, and $\boldsymbol{PSF}$ is the point spread function matrix. The nature of each variable is the same as that in Eq. 2.1. Figure 3.3 is a schematic similar to Fig. 2.1, modified to better illustrate the masking method, showing how multiple voxels contribute to a small region of pixels. If the pixel region has no significant intensity (like that shown in the circled region), then all the corresponding voxels will be masked.
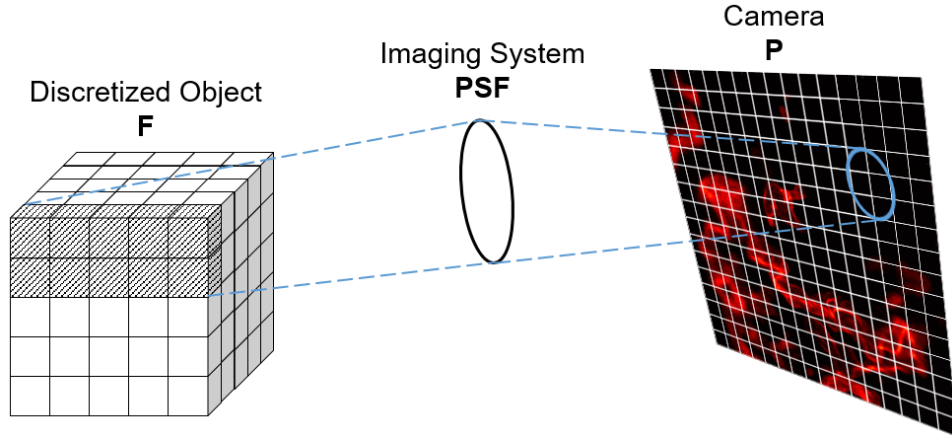
Figure 3.3: Mathematical formulation of tomography, illustrating the voxels that contribute to a region of pixels that contain no signal and will be masked

Similar to the formulation in Chapter 2, PSF in Eq. 3.1 has a number of elements equal to the product of the lengths of P and F. In this case, the size of P is on the order of 5×10^6 (from five megapixel cameras) and the size of F is of a similar size of around 4×10^6. Thus, PSF in this case has approximately $5 \times 4 \times 10^6 \times 10^6$ total elements. Once again, PSF is sparse because many voxels do not contribute to all pixels. This sparsity is exploited by the masking technique to considerably reduce to computational storage and time requirements to perform tomography by reducing the total number of pixels and voxels needed in the solution.

The masking method is a straightforward approach that operates on the principle that if a pixel on a camera receives a signal below a designated signal threshold (typically the noise level), then all voxels that project onto that pixel must emit no fluorescence signal and the pixel and all corresponding voxels are removed from P, F, and PSF, thus reducing the overall computational cost. In this work, reconstruction using the masking method was not sensitive to the value for the chosen signal "floor" for the dataset, and the same chosen value was used successfully across the entire dataset. This is illustrated in Fig. 3.3, where the highlighted region of pixels contains no signal – i.e., no occurrence of the flame front, as represented by CH-VLIF, within the illuminated region of the flame. To further illustrate which regions are masked, Figure 3.4 shows a comparison between three raw projections (top) and the same projections after masking has been applied (bottom). In the masked
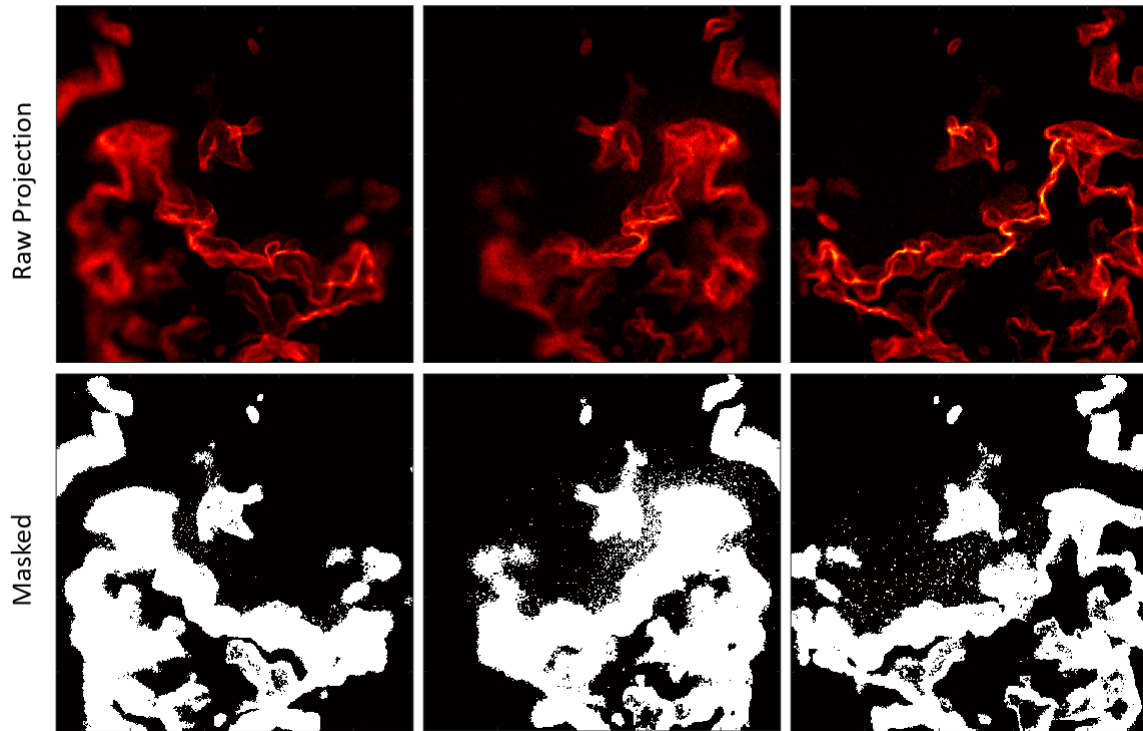
Figure 3.4: Comparison between three raw projections (top row) and the corresponding binarized images (bottom row), where white regions contain signal, and black regions contain signal below the noise level and are to be masked

projections, all pixels with signals above the signal floor are shown in white, and all pixels below the estimated noise level are shown in black. For some projections, there could still be some pixels that are likely related to noise or very low-signal regions in the measurement volume that were not masked (particularly evident in the middle projection shown in Fig. 3.3). While the noise floor could be raised to exclude these regions, it is worth not masking too aggressively as to avoid masking regions that may be necessary for a high-accuracy reconstruction. All voxels in the measurement volume that contribute to any masked pixel, as determined by the PSF, were excluded from *PSF* and thus the tomographic reconstruction, saving both computational time and memory.

A straightforward implementation of the masking technique may have undesirable effects under the presence of measurement error, particularly view registration error, which is almost always present. Because masking will remove all voxels from the reconstruction that contribute to any pixel with insufficient signal, any unaccounted-for error in the
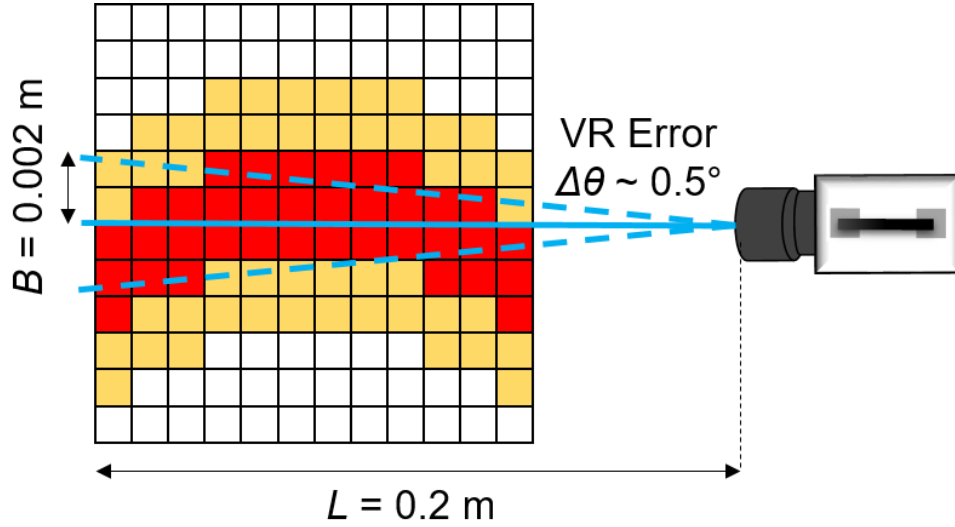
Figure 3.5: Schematic showing a buffer region (yellow) that has replaced some masked voxels (white) around a region of unmasked voxels (red). The thickness of the buffer is determined by the estimated view registration error.

location and orientation of a camera view may remove voxels that should be included. This effect will be most present at the edge of the flame surface, where voxels contribute to regions at the interface between signal and no signal on the measured projections. For this reason, a buffer region has been included at the interface between masked and unmasked voxels that reduces the total number of voxels masked.

Figure 3.5 shows a 2D schematic of how the buffer region is implemented, where the red voxels are those that are expected to contain signal and are unmasked, the white voxels are those that have been masked due to contributing to pixels that contain signal below the designated signal floor, and yellow voxels are those that replace the white masked voxels to act as a buffer and will not be masked. The amount of buffer is determined by the estimated error in camera orientation based on the view registration process. The width of the buffer is given by:

$$B = L \sin(\Delta\theta) , \tag{3.2}$$

where B is the width of the buffer, L is the distance from the camera lens to the far end of the measurement volume, and $\Delta\theta$ is the estimated error in camera orientation. Once the buffer width has been determined, the width is converted into the nearest number of voxels

38

based on the voxel width, and the buffer region is applied at the interface between masked and unmasked regions in all three spatial dimensions. In this way, the risk that signal-containing voxels will be unnecessarily masked due to view registration error is drastically reduced. Under the experimental conditions here, with a view registration uncertainty of 0.5°, the estimated necessary thickness of the buffer region is about 2 mm.

Besides saving computational resources, the masking technique also provides the potential to improve the achievable spatial resolution of the reconstruction. The spatial resolution of any tomography measurement is determined by both the hardware (the camera and lenses used and their orientations) and also the discretization size. For a given set of hardware, the spatial resolution is ultimately limited by the linear algebra limit when no *a priori* information is assumed [30, 80]. Specifically, the information that can be reconstructed (the total number of voxels) cannot exceed the information obtained by the measured projections (the number of pixels). By implementing masking, only a reduced fraction of the measurement volume needs to be reconstructed, and thus more and smaller voxels can be used within these regions and the spatial resolution may be improved. As shown in the next section, such an advantage is especially relevant for the CH-VLIF measurements because CH radicals only exist in a thin layer at the flame front. Thus, a simple application of ART would assign a large number of voxels to regions with no CH at all, resulting in a waste of computational resources and also the possibility of not achieving the maximum spatial resolution allowed by the hardware. Additionally, because masking only removes voxels that contain little to no fluorescence, no reduction in reconstruction accuracy is anticipated.

3.4. Results and Analysis

After image post-processing and preparation of the masking parameters, the measured projections were used as inputs to the tomographic reconstruction algorithm. Figure 3.6 shows a comparison of results, both with and without the use of the masking technique, obtained from the VLIF projections shown in Fig. 3.2. The top row shows results without using masking, where all voxels are considered within the reconstruction. The bottom row shows results using masking, including the buffer region, where only
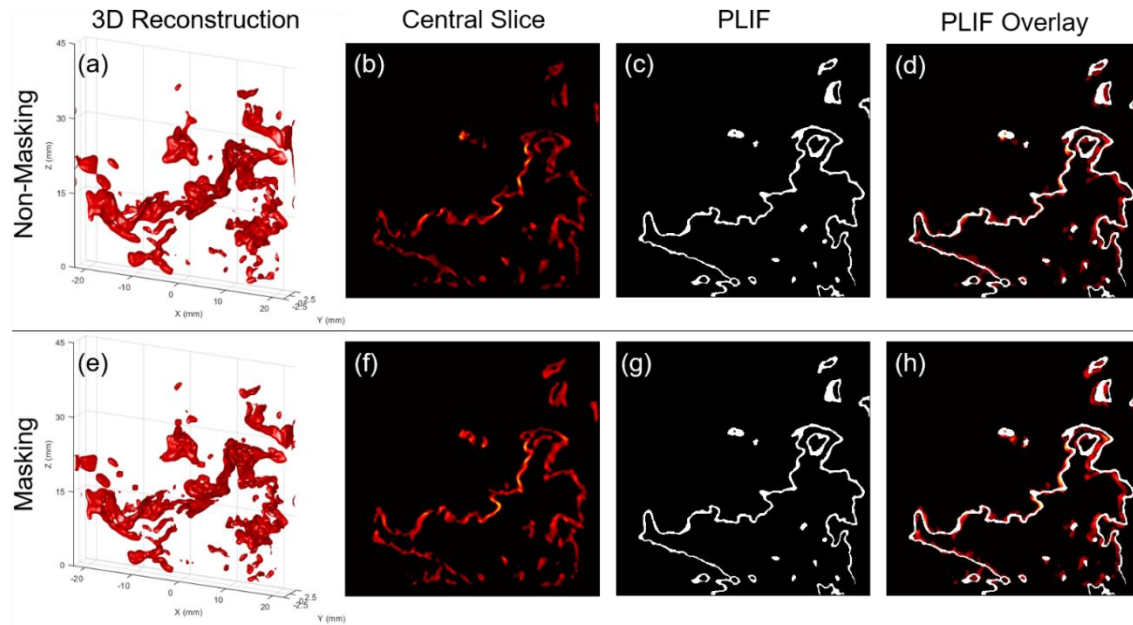
Figure 3.6: Results from the non-masking (top) and masking (bottom) methods. Panels (a) and (e) show the 3D reconstruction, panels (b) and (f) show a central slice of the reconstruction, panels (c) and (g) show the binarized PLIF measurement and are identical, and panels (d) and (h) show an overlay of the PLIF and central slice of VLIF for direct comparison.

voxels that contributed to pixels with sufficient signal were considered in the reconstruction. The measurement volume for the non-masking method was discretized into $256 \times 256 \times 30$ voxels (~2×10^6 total voxels) and had a discretization size of ~0.16 mm (i.e., about $(0.16 \text{ mm})^3$). The volume for the masking method was discretized into $324 \times 324 \times 38$ voxels (~4×10^6 total voxels) and had a discretization size of ~0.13 mm, although the masking method excluded about 40% of the total number of voxels; thus, ~2.5×10^6 voxels were solved. In both cases, the measurement volume was 42 mm (width) $\times$ 42 mm (height) $\times$ 5 mm (depth). The total number of computed voxels was kept roughly the same between both methods; however, the masking method reallocated the voxels more strategically in a smaller volume, reducing the voxel size and, consequently, a higher spatial resolution may be achieved without violating the linear algebra limit. It should be noted that the fraction of the measurement volume that will be masked is dependent on the projections and can change significantly from one exposure to the next. For both the masking and non-masking methods, the voxel discretizations were between 2-3 times

smaller than the laminar reaction layer thickness for CH (0.36 mm), indicating that the smallest structures that could be measured may be resolved, but not with a very high level of accuracy. The largest structures, those near the integral length scale of 9.2 mm, are easily resolved with such a voxel resolution, as well as those at the Taylor microscale (1.3 mm). However, regardless of the limitations of CH imaging, turbulent structures on the Kolmogorov scale (0.06 mm) are well outside the range of being resolved with the spatial resolution achievable using this hardware setup. In fact, such a small scale is unable to be resolved well using the PLIF measurements in this work, which have a pixel resolution of about 0.04 mm. Therefore, due to the limitations of hardware and CH imaging, this work focuses on measurements between the scale of the reaction layer thickness and the integral length scale.

Figures 3.6a and 3.6e show the 3D reconstructions as a smoothed isosurface of the flame surface, as represented by CH-VLIF, where the isosurface value was chosen to best show the regions of greatest intensity. Figures 3.6b and 3.6f show central slices from the 3D reconstructions that were taken at the same location and cross-sectional angle as the PLIF measurements. The signal value throughout all regions with a significant signal was relatively uniform in both the masking and non-masking cases and thus made it easy to determine a suitable value for the display of the isosurface. Figures 3.6c and 3.6g show the binarized PLIF measurement and are identical. Finally, Figs. 3.6d and 3.6h show an overlay of the VLIF central slices and the PLIF measurement for direct comparison. Overall, the CH layer obtained by the masking method appeared to be slightly more continuous and generally agreed better with PLIF measurement via visual examination (e.g., the small features in the top-right corner of Figures 3.6b and 3.6f). However, in the remainder of this discussion, quantitative metrics are used to evaluate the agreement between the PLIF and VLIF measurements.

First, the effect of the buffer region on reconstruction quality is examined to demonstrate that an appropriately thick buffer is necessary when implementing the masking method. To demonstrate this plainly, Figure 3.7 shows a comparison between a measured projection and the re-projections using masking with and without a buffer. Without the use of a buffer, given the estimated 0.5° view registration error, there are
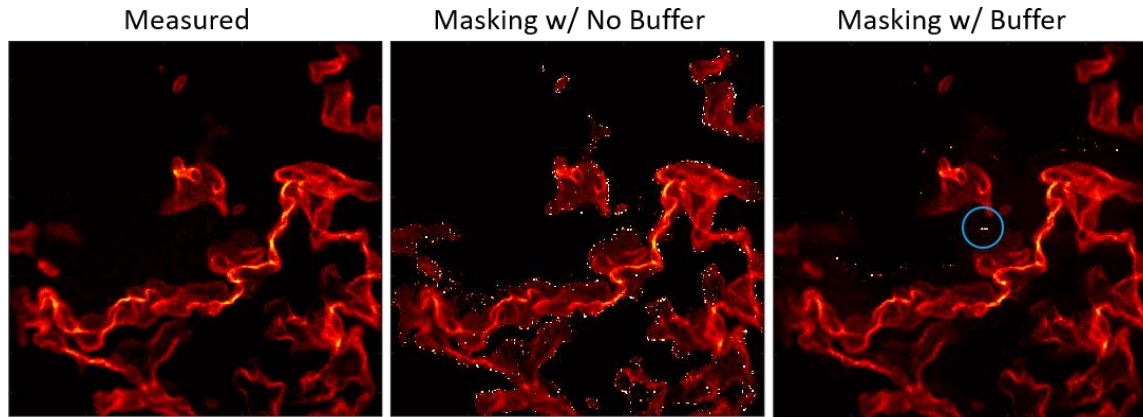
Figure 3.7: Comparison between a measured projection and re-projections using masking both with and without a buffer region

significant errors within the re-projection, particularly near regions at the interface between signal and no signal, and also very small features, as expected. When an appropriately thick buffer region was applied (nine voxels thick in the case of Fig. 3.7), these errors were drastically reduced and were mostly only present in regions with very little signal and small features, an example of which is circled. Additionally, these small errors can easily be removed either manually or with the use of a filter.

The effect of the buffer layer on reconstruction accuracy can be determined by examining the flame front contour length. The flame front contour length was measured by calculating the perimeter, including internal structures such as apparent holes within the flame, for both VLIF and PLIF measurements. For the PLIF measurement, the data was binarized (as seen in Fig. 3.6) and the perimeter was calculated by measuring the distance between adjoining pairs of pixels or voxels around the signal border. Both the binarization and the perimeter calculations were assisted by a built-in MATLAB function, with the binarization using the Otsu threshold method, and the perimeter measurements based on Ref. [81]. For the 3D reconstruction of the VLIF measurement, first the central plane that corresponded to the PLIF measured had to be identified. To do this, an iterative process was carried out over the four test cases where a central slice of the reconstruction was extracted and its correlation was calculated with respect to the PLIF measurement. The iterative process shifted both the angle at which the cross-section was taken as well as its
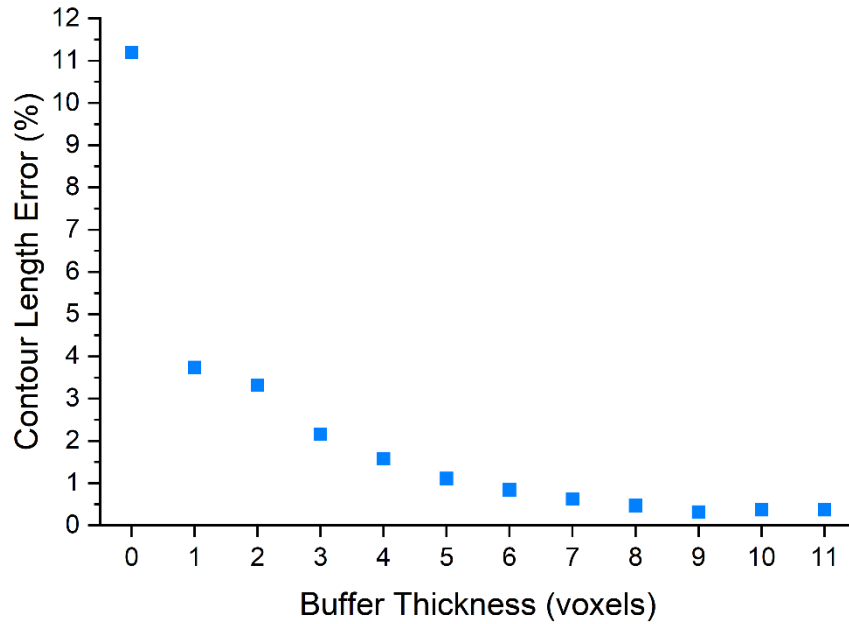
Figure 3.8: Flame front contour length error of the VLIF reconstruction compared to the PLIF measurement using the masking method as a function of the thickness of the buffer region in voxels

spatial shift within the measurement volume to find the values that maximized this correlation. It was found that, on average across the four cases, the optimal cross-sectional angle was 0.42° (compared to the estimated 0.5° in the setup shown in Fig. 3.1), and a spatial shift of the intersection between the PLIF laser sheet and the VLIF laser slab of 0.17 mm. The central cross-section of the VLIF reconstruction was taken under these parameters and, because the slice crossed the voxels at an angle, the new voxel values were interpolated based on the reconstruction.

To find the perimeter of the central cross-section, this planar slice was binarized and the perimeter was calculated in the same way as the PLIF measurement. Figure 3.8 shows the error between the reconstructed flame front contour length and the PLIF measurement for one instantaneous frame (the same frame as that shown previously) across different buffer thicknesses, starting with no buffer. There are two key findings from this: there is a drastic decrease in error when implementing even a single voxel of buffer, and there is a plateau in error once a sufficient buffer thickness has been reached. The drastic increase in error without a buffer was caused by large portions of the flame front not being

43

reconstructed due to being masked, thus significantly reducing the total flame front length. Including a single voxel buffer was sufficient for these regions to be reconstructed, albeit not at full accuracy. Second, the error reached a minimum plateau once a sufficient buffer thickness had been reached, which was nine voxels in this case. Once this thickness was reached, no flame features were masked due to the error in view registration and this buffer thickness corresponded to the approximate error in view registration. In this case, nine voxels corresponded to about 1.2 mm of buffer in the measurement volume. This was lower than the expected 2 mm of buffer, although this could be attributed to the positions of the cameras and the thin nature of the flame, where the error in camera orientations did not propagate through the entire depth of the measurement volume, in addition to the fact that the view registration errors may have been smaller than anticipated. Once the minimum necessary buffer thickness was determined, this buffer thickness was used in all subsequent masked reconstructions.

To provide a more quantitative comparison of the overall results, the flame front contour lengths of the reconstructed central slice and the PLIF measurement were calculated and compared for four different instantaneous flame measurements, all taken under the same testing conditions (Case 3B-1.05). Figure 3.9 shows a measured projection, the 3D reconstruction and the corresponding central slice using the masking method, and the binarized PLIF measurement for three other instantaneous measurements. Note that Frame 3 is that which has previously been shown, and the frames are ordered based on their chronology in the dataset. Also note that Frame 2 is that which is described in Ref. [69], although this analysis used different reconstruction parameters and methods for estimating flame front contour length. Similar to Fig. 3.6, visually there is good agreement between the VLIF and PLIF measurements, with some small exceptions. As seen across all cases, the VLIF reconstructions do not extend as far down as the PLIF measurement, and the contour length measurement for PLIF excluded regions that weren't present in the reconstructions.

In this work, it was assumed that the PLIF signal represented the contour length in 2D and, based on this assumption, was used as the ground truth for the flame front contour length. Figure 3.10a shows a comparison of the contour length between the masking

44
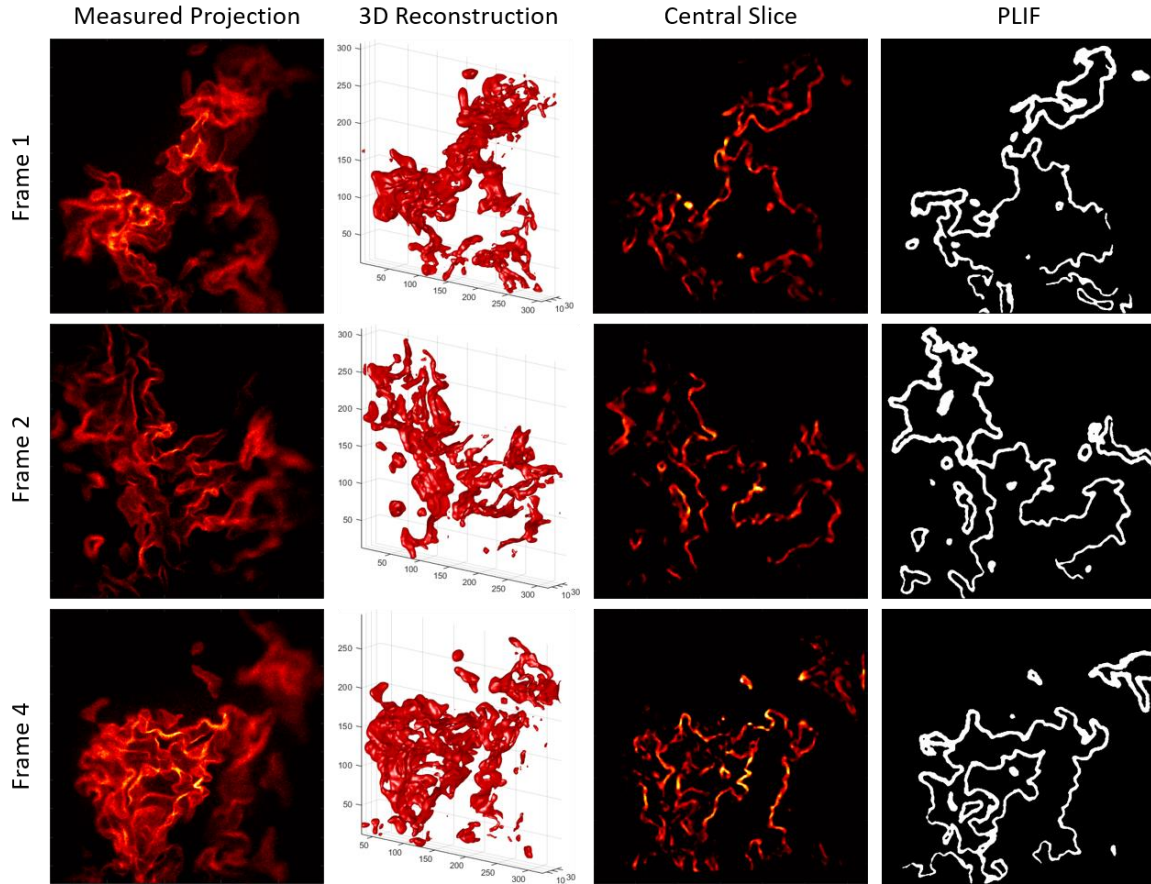
Figure 3.9: Results from the other 3 frames, where the reconstruction and central slice of the reconstruction are shown using the results from the masking method

method, the non-masking method, and the PLIF measurement, across the four instantaneous flame measurements. In each case, there is relatively good agreement between all three measurement techniques. The large variation in contour length between each frame is due to the large turbulence of the flame and the significant time difference between each of the instantaneous measurements, as witnessed by the drastically different-looking flame in Fig. 3.9. Figure 3.10b shows the corresponding relative error in the contour length from the ground truth, where the error is defined as the magnitude difference with flame-contour length derived from CH-PLIF. Here, Frame 3 is that which is shown in previous figures in this chapter. In each of the four cases, the masking method had a lower absolute relative error in contour length than the non-masking method. Additionally, the computational time for the masking method was on average 21% less than that for the non-

45
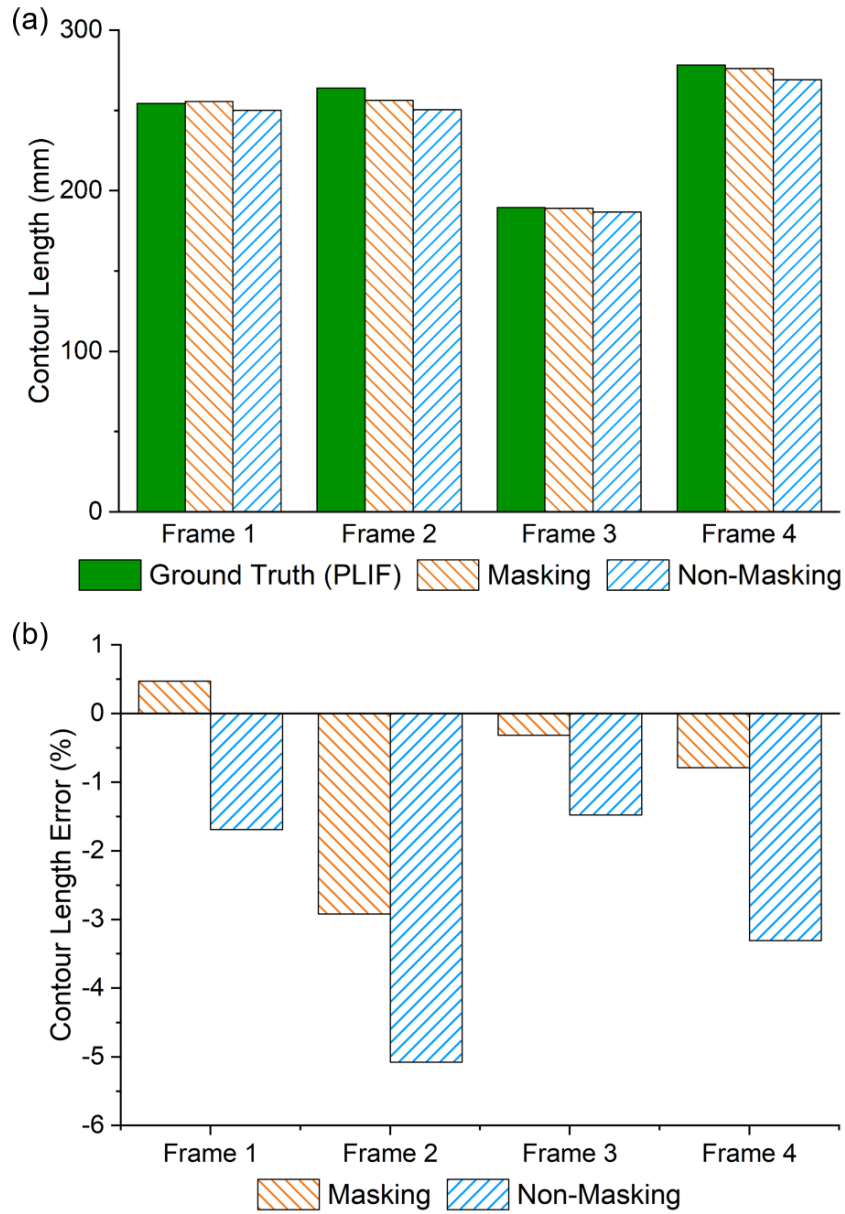
Figure 3.10: Comparison of flame front contour length for the masking and non-masking methods against the ground truth (PLIF) for four frames where a) shows a comparison of the contour lengths, and b) shows the relative error in contour lengths

masking method across the four frames while simultaneously having a smaller voxel size (0.13 mm compared to 0.16 mm), which likely contributed to the decrease in contour length error. These results indicate that it is possible to apply the masking method in such a way as to simultaneously decrease computational cost while increasing spatial resolution.
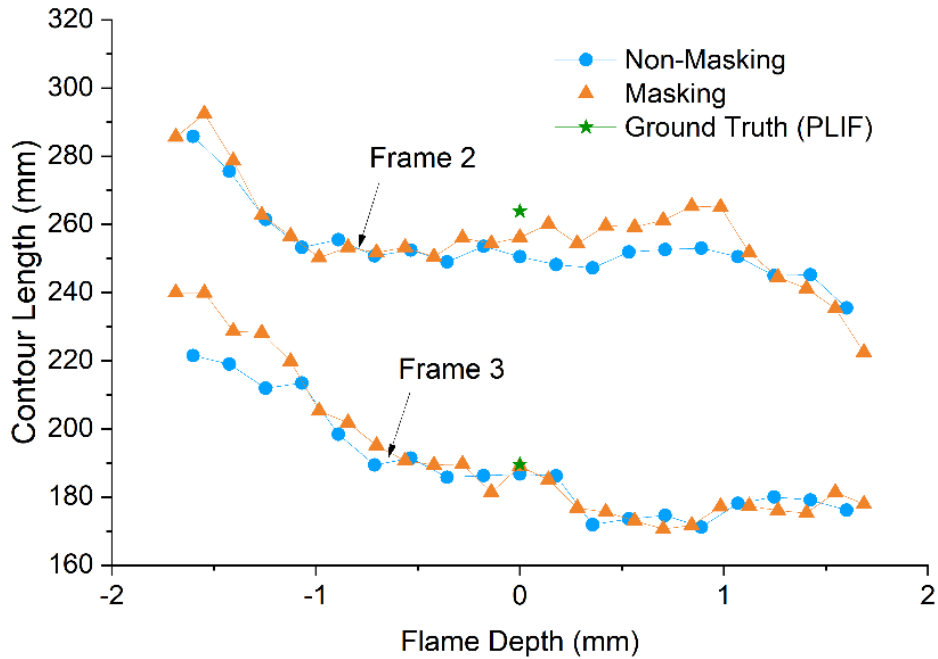
Figure 3.11: Flame front contour length at different depths for the masking and non-masking methods for Frames 2 and 3, with the PLIF as the ground truth shown as a star

Figure 3.11 shows the flame-contour length for both the masking and non-masking methods at different flame depths (calculated at different Y planes) for Frames 2 and 3. It should be noted that the significant difference in overall flame-contour length between the two frames is due to the specific flame conditions for each instantaneous measurement, as the highly turbulent flame changed significantly from one exposure to the next. A second notable result is the variation in contour length as a function of flame depth for a single instantaneous snapshot of the flame. In the above analysis, the masking method was consistently more accurate than the non-masking method, and thus it can be assumed that the calculation of the contour length from the masking method would be more accurate than the non-masking method at any flame depth. As seen in Fig. 3.11, the two methods generally have very good agreement on contour length, except for a few small regions. For instance, for Frame 3, the masking method shows a slightly longer contour length than the non-masking method between -1.75 mm and -1.25 mm. Likewise, for Frame 2, the masking method is longer from 0 mm to 1 mm. There are two possible explanations for this result. First, the masking method will likely have a more defined edge at the flame surface, which can be seen in Figure 3.6, where the central slice from the masking method has a more

47
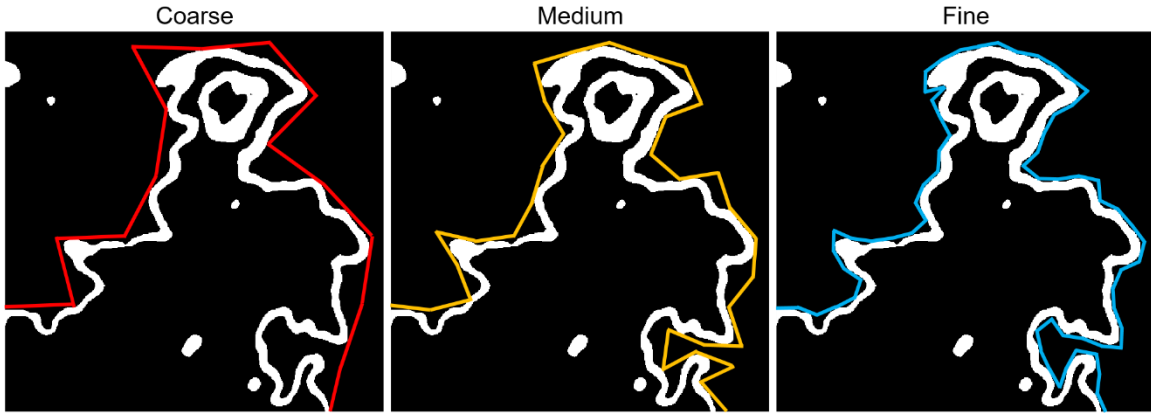
Figure 3.12: Example of the so-called "coastline paradox", illustrating how finer resolution measurements typically yield longer perimeter results

uniform signal level. This is because the masking method may eliminate some voxels near the flame edge that may have contributed to some, but not all, of the projections. Second, the smaller voxel size of the masking method can resolve smaller features that may add to the overall contour length.

With regards to the effect of discretization size and length measurements, it is worth mentioning what is colloquially known as the "coastline paradox" [82]. This is the phenomenon where the measured length of a complex perimeter (such as a coastline) increases as the discretization with which is measured decreases. This is because the smaller discretization is able to resolve smaller features that necessarily increase the measured length (as the shortest path between two points is a straight line, and any added vertex that does not lie on that line will increase the total length). Figure 3.12 shows an example of how this phenomenon affects the measured length of a segment of the flame shown in Frame 3. As seen, the shorter the lengths used to estimate the perimeter, the longer the total length is measured to be. More specifically, using rough measurements and arbitrary units to describe the lengths, the coarse measurements yielded a perimeter of 12.1 units, the medium yielded 14.9 units, and the fine yielded 16.3 units of length. However, as previously mentioned, due to the nature of the CH measurements, there is an anticipated ceiling on the maximum perimeter measurements that can be reached in practical experiments.
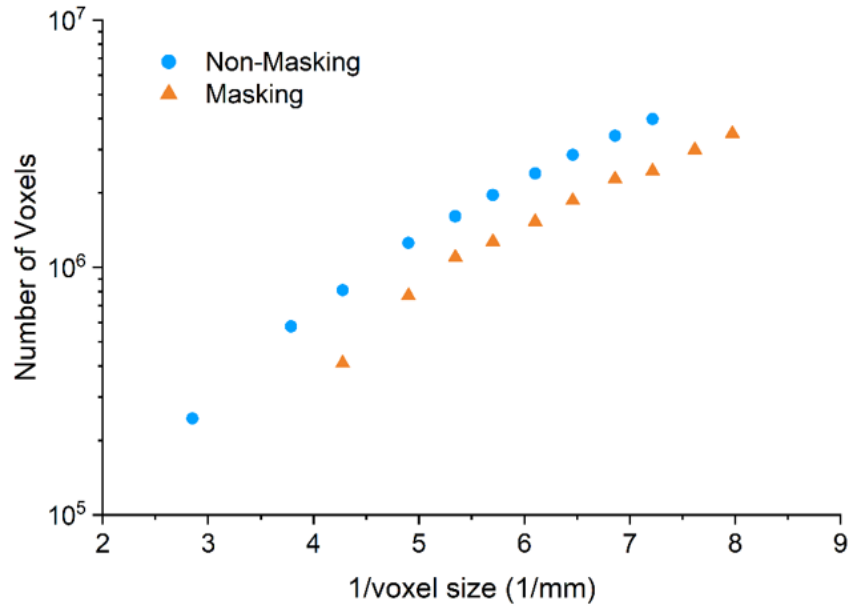
Figure 3.13: Total number of voxels in the reconstruction as a function of the inverse of voxel size, where the voxel size of the fine voxels is shown for the ASD method. Voxel size decreases as the horizontal axis values increase.

To quantify the effect that voxel size has on the contour length and overall accuracy, further analyses were performed by examining the effectiveness of the masking method across many different parameters using the results from Frame 3. Figure 3.13 shows a graph of the number of voxels used in reconstruction versus the inverse of voxel size for the masking and non-masking methods. This test was performed by uniformly increasing the number of voxels within the measurement volume for both methods and calculating the total number of computed voxels, noting that the masking method only computes voxels that contribute to pixels above the predetermined noise floor. The range of voxel sizes shown for both cases was chosen such that the smallest size using the ASD method had approximately the same number of total voxels as the baseline method, and similarly for the largest voxel size. As expected, the masking method had a smaller voxel size for a given number of total computed voxels, as it attributed the same number of voxels to a smaller volume.

Figure 3.14 shows the absolute error in flame front contour length versus the total number of computed voxels between the two methods. Across all voxel sizes, the masking
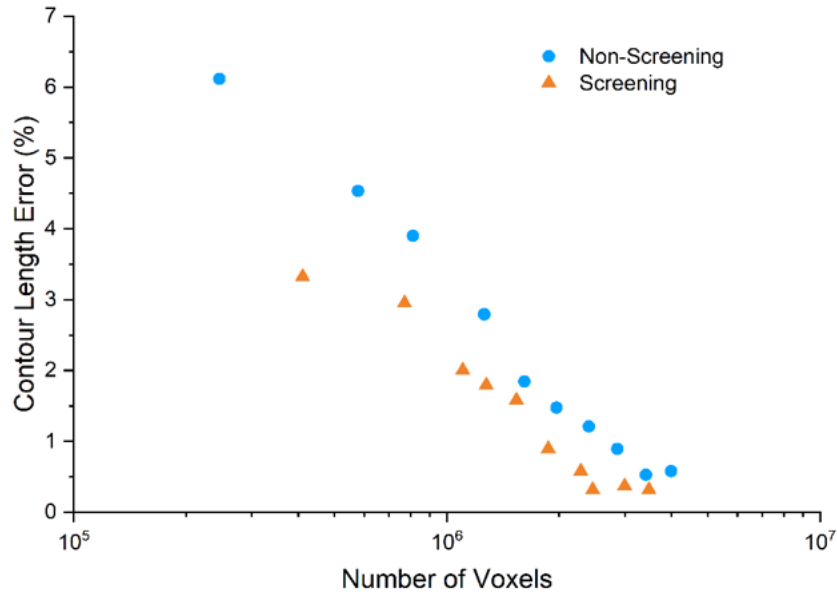
Figure 3.14: Error in flame front contour length as a function of the total number of voxels used in the reconstruction

method achieved a smaller error in contour length given the same number of computed voxels. For example, the non-masking method achieved about 1.5% error in contour length using 2×10^6 voxels, while the masking method achieved about 0.9% error using approximately the same number of voxels. This is again due to the masking method better allocating the same number of voxels to regions of high interest. It is worth noting that the error plateaus once a certain voxel size is achieved, where a further decrease in voxel size does not produce better results.

Figure 3.15 shows the absolute error in contour length versus the computational time, where all computations were performed on a single core of a 2.20 GHz Inter Xeon E5-2650 v4 processor. The trend is similar to that of Fig. 3.14, which is expected as computational time is proportional to the number of voxels computed, and the masking method reduces both the number of voxels and pixels in the reconstruction process. In this case, for example, to achieve under 1% error in contour length, the masking method reduced the computational time by nearly half, from about 1400 s to 700 s, as shown in Fig. 3.15. It is worth noting that, all other factors held constant, the computational time is proportional to the memory requirements to store the variables in Eq. 3.1, and thus the
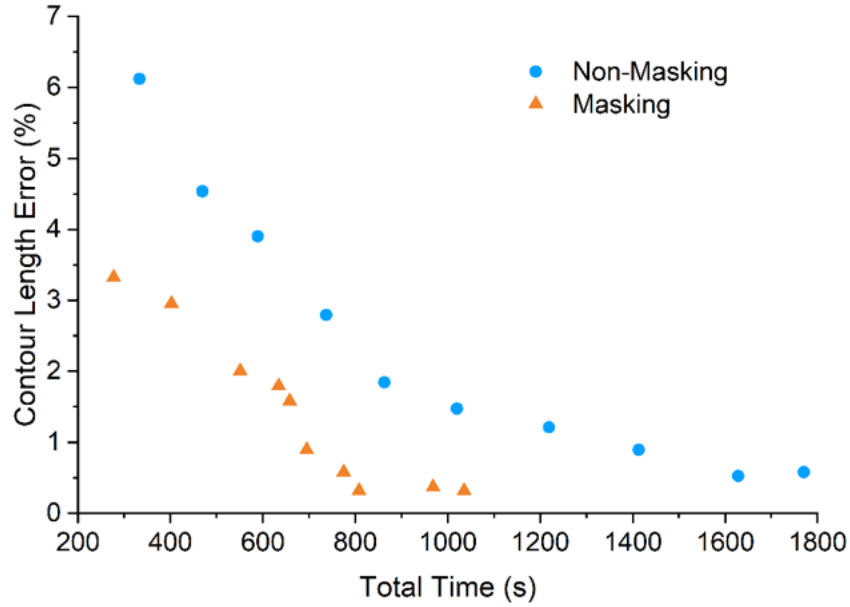
Figure 3.15: Error in flame front contour length as a function of the total computational time

masking method can reduce both the computational time and memory requirements while simultaneously increasing accuracy.

Finally, Fig. 3.16 shows the absolute error in contour length versus the inverse of voxel size. Here, there was no significant difference between the masking and non-masking methods, unsurprisingly indicating that voxel size was the primary factor in determining overall reconstruction accuracy until the plateau was reached, where a decrease in voxel size no longer yielded a smaller error. This plateau indicates that the maximum spatial resolution has been achieved under the current hardware and setup conditions. It is again worth noting that, as shown by the results in Fig. 3.11, the exact degree of improvement depends on the specific flame conditions and setup limitations (e.g., laser sheet thickness for the PLIF measurement), and varies from one exposure to the next, but improvements were observed in all frames tested in this work.

The above analyses were repeated for a total of 200 different frames and the above trends above were observed in the extended sample. It was found that even under smaller voxel size settings, the masking method saved computational time compared to the non-masking method. Using the same parameters as above for the non-masking method ($256 \times$
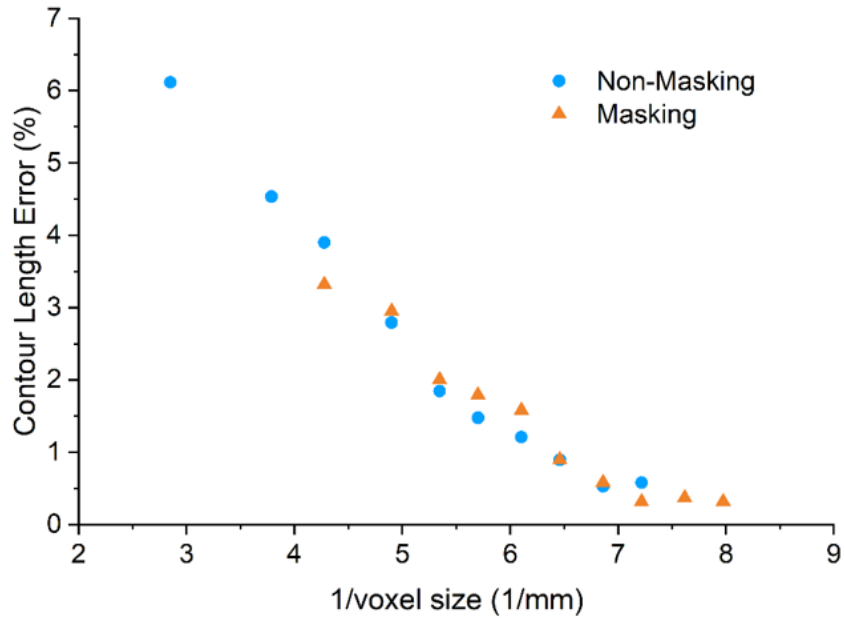
Figure 3.16: Error in flame front contour length as a function of the inverse of voxel size, where the voxel size of the fine voxels is shown for the ASD method. Voxel size decreases as the horizontal axis values increase.

256×30 voxels), the mean computational time to perform the tomography was 928 s/frame with a standard deviation of 16 s using the non-masking method. For the masking method, using a greater number of voxels ($290 \times 290 \times 34$ voxels, or a discretization size of ~0.14 mm), the mean computational time was 739 s/frame with a standard deviation of 137 s. The smaller deviation of the non-masking method was due to the fact that it did not treat any frame differently based on the projections, whereas the masking method may include more or less total voxels depending on the specific flame conditions. However, even with the large deviation, the masking method was able to achieve increased accuracy with smaller voxels while reducing computational time on average.

As a final analysis of the masking method, to confirm that the VLIF measurements were able to obtain sufficient spatial resolution to resolve features at the scale of the reaction layer thickness, the thickness of the measured CH zone is compared between the VLIF and PLIF measurements. Figure 3.17 shows a zoomed-in region of the flame displayed in Fig. 3.6 where the width of the reaction layer was calculated based on the width in voxels and pixels for the VLIF and PLIF measurements, respectively. To calculate
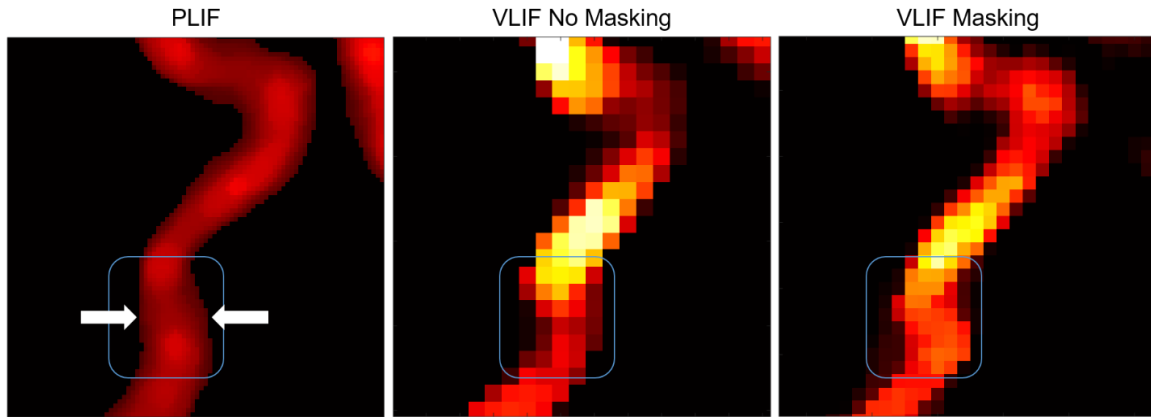
Figure 3.17: Zoomed-in regions of the flame, comparing the thickness of the CH LIF from the PLIF measurement and the corresponding cross-section of the VLIF measurements with and without the use of masking

the width for each measurement, the average width in pixels or voxels within the highlighted box was calculated and multiplied by the physical dimension of the pixel or voxel. The highlighted region was chosen due to its relative verticality of signal, making it easier to estimate the width, and also that the flame thickness in this region is a good representation of the entire flame measurements. For the PLIF measurement, the average flame thickness in the highlighted region was calculated to be 0.61 mm, which is noticeably larger than the estimated flame thickness based on CH of 0.36 mm. This may be due to the turbulence of the flame, or the fact that CH may exist in a small region outside the reaction layer. Additionally, the laser sheet used for PLIF is not infinitesimally thin (with a thickness of about 0.17 mm) which may also contribute to some thickening of the measured CH region. For the VLIF measurement without masking (using a voxel size of 0.16 mm), the flame thickness was measured to be 0.70 mm, while the VLIF measurement with masking (using a voxel size of 0.13 mm), including a buffer region, had a flame thickness of 0.64 mm. Considering the PLIF measurement as the ground truth, the masking method had a noticeably greater accuracy, and also visually matched the overall shape from the PLIF measurement more closely. Both of these are likely the case due to the finer voxel size, and subsequent greater spatial resolution, offered by the masking method. Once again, the masking method has been shown to provide greater accuracy with a smaller

computational cost than the baseline method of reconstruction, indicating that it is a useful tool in combustion diagnostics.

3.5. Summary

This work describes the validation of a masking technique to improve the tomographic inversion process. The focus of the work was on the direct validation of the technique by comparing planar laser-induced fluorescence (PLIF, which represents a 2D realization of the target quantity) and simultaneous volumetric LIF (VLIF, which represents a 3D realization of the target quantity) measurements. Through this comparison, the accuracy of the reconstruction and the computational times were quantified to assess the validity of the masking method and the improvements it can offer in reducing computational costs while maintaining, or even increasing, accuracy and spatial resolution. The target for this work was the methylidyne radical (CH), which was excited using strong transitions in its C-X(0,0) band. Since CH exists only in a thin layer near the flame front, LIF measurements of this species are a good candidate for reconstruction using the masking method. The validation was carried out by employing highly turbulent premixed CH_4-air flames that possessed abundant flame surface density. In this respect, the demonstration described here is a severe test of our implementation of tomographic inversion generally and the 3D masking method specifically.

The flame-contour lengths derived from the CH-PLIF measurement and a central slice of the CH-VLIF reconstruction, taken from the same flame depth as the PLIF measurement, were compared for both the masking and non-masking methods. It was found that the masking technique was able to significantly reduce the computational time while simultaneously improving the reconstruction accuracy. However, due to the error in camera orientation, as calculated by the view registration process, it was found that a buffer layer of approximately 1.2 mm was required to maximize the benefits of masking while minimizing the reconstruction error due to view registration error. Through comparison of the flame front contour length, it was found that the voxel size was the most important factor in determining reconstruction accuracy with the hardware and setup used in this work. The masking technique enabled reconstruction at a higher spatial resolution,

indicated by a lower error in flame-contour length, by restricting the reconstructed measurement volume to regions where CH radicals existed (i.e. close to the flame front).

As an additional metric to compare the validity and accuracy of the masking method, the thickness of the CH region was calculated. Based on theoretical expectations, the thickness of the CH reaction layer was expected to be 0.36 mm. However, the PLIF measurement, which is assumed to be the ground truth due to being a well-established technique with high spatial resolution, measured the thickness of the CH layer to be about 0.61 mm, which is quite a bit larger than expected. This could be due to a variety of factors, including the thickness of the PLIF sheet (0.17 mm), the high turbulence of the flame, or the existence of CH outside of the reaction layer. In comparison, the thickness of the CH layer using the masking method was calculated to be 0.64 mm, while the non-masking baseline method calculated a thickness of 0.70 mm, again indicating that the masking method was able to improve accuracy and spatial resolution while simultaneously reducing the computational cost.

While masking techniques have been previously shown to be effective at reducing computational time and improving the accuracy of tomographic reconstructions in other applications, such as tomographic PIV and chemiluminescence measurements, this work demonstrates the applicability of the masking technique to VLIF tomography, specifically of the CH radical, for which the masking technique is particularly well suited. However, one key limitation of these experiments is that the measurements are collected using relatively small flames under laboratory conditions and may not accurately reflect real-world conditions where combustion diagnostics could be applied. Additionally, due to limitations of the camera and laser setup for LIF measurements, the results here are not time-resolved and the temporal evolution of the flame cannot be analyzed. Therefore, time-resolved flame measurements under more practical and realistic settings are highly desired, and the following chapter describes an experimental setup to achieve such measurements.

Chapter 4

4. *In Situ* Implementation of FBEs for 4D Flame Visualization within a Ground Vehicle Testbed

A subset of this work has been published in *Combustion and Flame* under the title "*In Situ* Imaging of 4D Fire Events in a Ground Vehicle Testbed Using Customized Fiber-based Endoscopes."

Abstract

Understanding the dynamics of fire events in ground vehicles is critical to improving crew survivability. To advance our understanding, four-dimensional (4D) measurements are sorely needed to resolve both the temporal and spatial dynamics of fire events. However, there are several key challenges toward such measurements, including equipment requirements and optical access. 4D measurements, especially with sufficient temporal resolution, can be equipment intensive. Such equipment requirements are further compounded by the relatively hostile environments encountered in vehicle testbeds. Moreover, there is often very limited optical access available for obtaining such measurements within vehicular environments. This work describes the design and implementation of a customized fiber-based endoscope (FBE) proof-of-concept setup in order to overcome these challenges and enable 4D flame measurements in a ground vehicle testbed located at the Army Research Laboratory, Aberdeen Proving Ground, and is part of an ongoing campaign to characterize these flames. Using a customized 9-to-1 FBE bundle, 4D imaging of relatively large-scale fire events was demonstrated under field conditions at 500 Hz with a single camera located at a safe distance outside the vehicle. Measurements were collected of a propane torch flame within a volume of 19.2 cm (width)

× 19.2 cm (depth) × 15.0 cm (height) and a larger, more turbulent pool flame within a volume of 35 cm (width) × 35 cm (depth) × 29 cm (height). The measurements were then processed by volumetric tomography to resolve the temporal dynamics and spatial structures of the target flame within the vehicle testbed by calculating the time evolution of key features and the estimated flame surface area. This proof-of-concept measurement platform has shown that such an FBE-based setup can overcome many of the challenges of field measurements while enabling time-resolved tomographic measurements of large and turbulent flames.

4.1. Introduction

While a deeper understanding of the dynamics of turbulent flames within realistic applications has long been desired [83-85], it is of particular significance in the context of fires within ground vehicles. A large portion of injuries and casualties are due to or related to fire incidents in ground vehicles. Due to the very fast evolution of fires within these vehicles and their complicated confined space [41], understanding the development and propagation of the flame front is of critical importance for safety concerns. In order to fully resolve such fire dynamics, four-dimensional (4D) diagnostics are required, i.e., diagnostics that are capable of resolving the spatial structures of the fire in all three spatial dimensions and also the temporal dynamics [30, 31, 86-88]. Optical and laser diagnostics provide some unique advantages for flame imaging due to their noninvasiveness [71, 89, 90]. Due to the importance of multidimensional measurements, the extension of laser-based diagnostics to 3D and 4D has attracted a considerable amount of research investment, as demonstrated in the previous chapter. However, laser diagnostics require extensive hardware that is relatively costly and delicate, and also requires sufficient optical access for illumination and signal collection [91]. Even without the use of laser diagnostics, the equipment setups for combustion emission tomography can be large and unwieldy, often requiring large mounts and mirrors [92].

These challenges are well illustrated by the 4D imaging of fire events in the ground vehicle testbed targeted in this work. Consequently, the primary goal of this work is to describe the development of a proof-of-concept 4D imaging setup, to demonstrate its implementation on the vehicle testbed, and to analyze how it overcomes the challenges and what its limitations are. The 4D imaging technique developed in this work relied on the combination of customized fiber-based endoscopes (FBE) and computed tomography. In order to perform volumetric tomography, multiple cameras are typically used to collect the integrated line-of-sight projections from different orientations. The measurement environment targeted in this work posed several significant challenges to this approach, including the equipment cost, equipment safety, optical access, and the difficulty of setup and alignment. With the development of fiber-optic technology, many of these challenges can be mitigated by the use of FBEs in place of multiple cameras, as described in earlier

works [78]. This past work demonstrated that the use of FBEs could dramatically reduce the equipment cost, simplify the setup and alignment, and minimize the footprint and optical access requirements for tomography measurements.

The majority of past work in combustion tomography, specifically those demonstrating the use of FBEs, has been limited to laboratory applications and environments. To advance the capabilities of tomographic measurements towards more practical applications, this work describes the customization and development of a new FBE setup aimed at field applications, such as the ground vehicle testbed described here. To accomplish this goal, a customized 9-to-1 FBE bundle was designed, with nine inputs combined into one output, so that the projection from up to nine different orientations could be simultaneously captured by a single camera. The lengths of the FBE input arm were customized so that they could reach different optical windows flexibly and allow the camera to be placed a safe distance away from the fire events. Furthermore, the FBE was designed so that lenses could be easily integrated into the FBE inputs to facilitate setup and alignment under field conditions. These new designs were tested in a field measurement campaign at the Army Research Laboratory at Aberdeen Proving Grounds (ARL APG) as part of a larger campaign to better understand and characterize the volatile flames encountered in vehicle fire situations. The three-day campaign demonstrated that the new designs overcame the anticipated challenges and successfully enabled 4D measurements of fire events within the vehicle testbed. Moreover, the design of the diagnostics was also shown to be sufficiently robust for the transportation between University of Virginia (Charlottesville, VA) and ARL APG, and for the assembly, alignment, measurement, and disassembly within three days. Finally, time-resolved 3D tomographic measurements were generated, the reconstruction fidelity was explored, and quantitative measurements of flame motion and changes in surface area were performed.

4.2. Experimental Arrangement for Field Measurements

The experimental arrangement can be broken into two major components: the testbed and overall setup, and the customized FBE assembly. The experiments described in this work were performed in a ground vehicle testbed located onsite at ARL APG. Figure
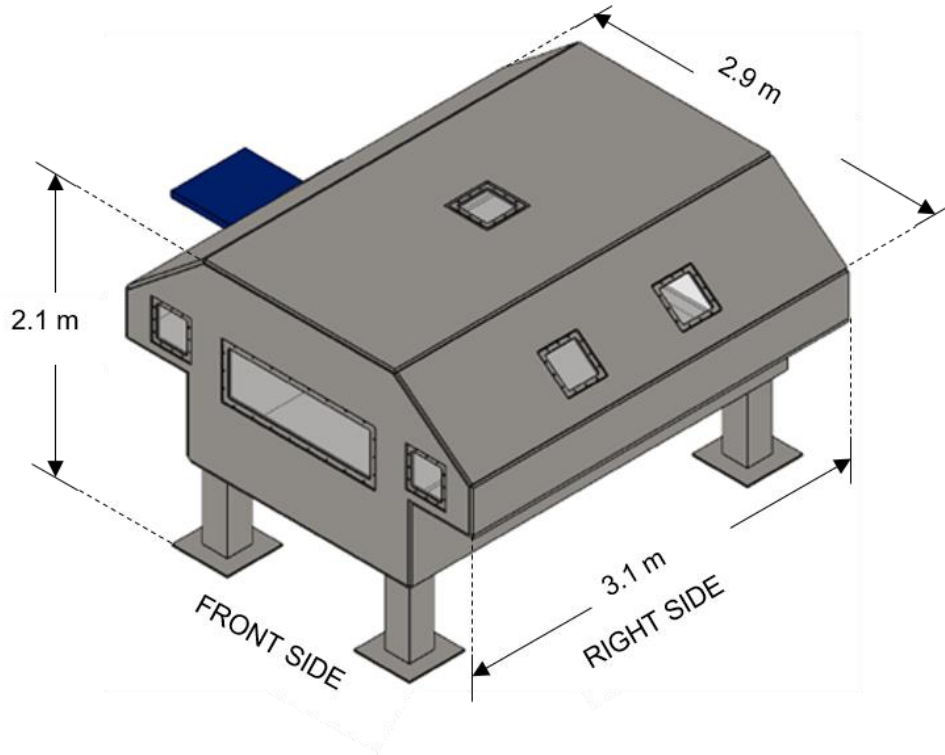
Figure 4.1: Schematic of the ground vehicle testbed located at ARL APG showing the front and right sides. Two additional viewports are hidden from view under the overhang on the right side.

4.1 shows a schematic of the testbed viewed from the front and right sides, which were the two sides used for image collection in this work. The front side had one large viewport in the center with dimensions of 117 cm × 36 cm and two smaller ports on either side with dimensions of 25 cm × 25 cm. The right side has four 25 cm × 25 cm ports, two of which can be seen in Figure 4.1, and two below the overhang. Typically, each viewport is covered by a polycarbonate window, however, the windows were removed for testing to reduce unwanted signals from glare.

Using the schematics provided, an in-house replica of the ground vehicle testbed was built to ensure that successful setup and data acquisition could occur during the short measurement campaign. Figure 4.2 shows the 1:1 scale replica of the testbed that was used to inform the design of the sensor setup, as well as a preliminary design of the setup. Using the replica testbed, multiple iterations of the sensor setup were constructed and tested to optimize data collection, transportability, and ease of on-site construction. Ultimately, the

Figure 4.2: Wooden replica of the ground vehicle testbed built at a 1:1 scale used for design and rehearsal of the FBE sensor setup

final setup that was easiest to implement relied on seven FBE inputs on the front side and the last two inputs on the nearest viewports on the right side. This allowed for the widest range of input orientations limited by the constraints of the FBE bundle and environment.

Based on the finalized sensor setup design, a single day of setup was required at the start of the ARL APG measurement campaign. Figure 4.3 shows the experimental arrangement for on-site, *in situ* measurements within the ground vehicle testbed, as seen from the front face of the testbed, where the single camera (Photron SA-4) and the customized FBEs are aligned and mounted on the custom 80-20 aluminum frame directly adjacent to the testbed. Seven of the nine FBE inputs viewed the target flames through the three front viewports, while the other two inputs viewed the flames from the side. As the targets for measurement data, two different flames were generated within the interior of the testbed: a propane torch flame and a pool flame. Because the polycarbonate windows were removed, smoke from the flames was able to exit through the testbed viewports and

Figure 4.3: Experimental setup of the 4D sensors to visualize flames within the ground vehicle testbed located at ARL APG

deposit on the FBE input lenses, illustrating again the benefits of a setup that can move the more expensive camera away from hazards.

Figure 4.4 shows the overall experimental setup schematically to better illustrate the FBE orientations with respect to the target flame, which are specified by the azimuthal angle (θ) and inclination angle (φ) as shown. Figure 4.4a shows the schematic from the top, where each FBE input, numbered 1 through 9 with increasing θ, was located approximately around the perimeter of a rectangle due to the geometry of the testbed and its viewports. Not all the inputs were aligned in a co-planar fashion, and therefore the inclination angle was defined, as shown in Fig. 4.4b. The FBE output integrated and transmitted all the signals captured by the nine inputs into the camera, as shown in Fig. 4.4a. The Photron SA-4 high-speed camera was fitted with a Nikkor 105 mm lens and was focused on the output of the FBE bundle. In this work, the target signals collected were primarily due to the emission from soot particles in the visible spectral range produced by the flames. Therefore, the 4D diagnostics used here were
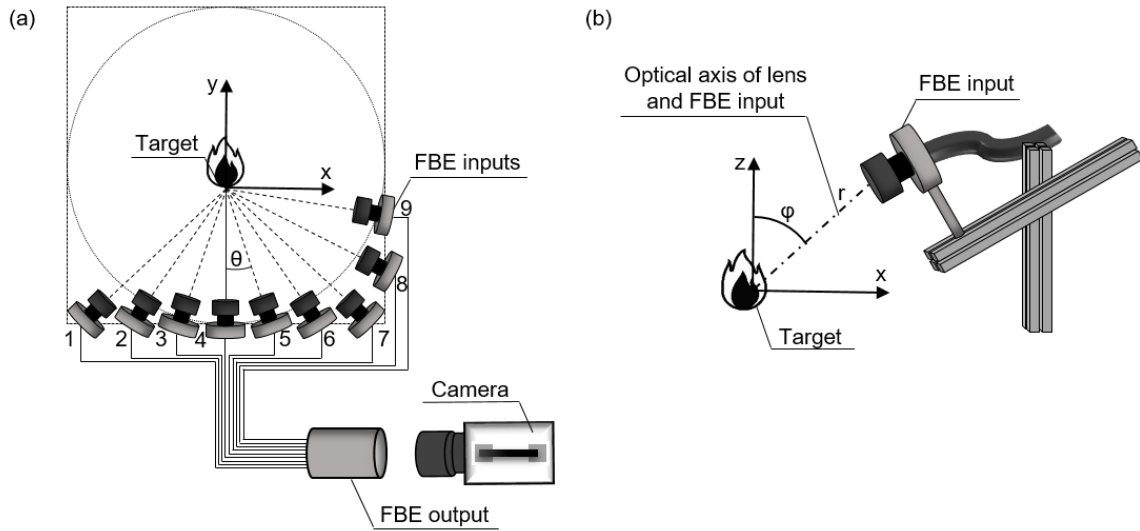
Figure 4.4: Schematic of the overall experimental setup, a) as seen from the top view, where θ is the azimuthal angle of the FBE inputs, and b) as seen from the side view, where φ is the inclination angle

based on emission tomography, and this work therefore essentially uses the soot emission intensities to represent flame locations [31].

Due to the limitation of having to set up all FBE inputs not equidistant from the target flame (ranging between 1.3 and 2.0 meters), the 8th and 9th FBE inputs, those that were furthest from the camera (with an arm length of 3.0 m), had difficulty in alignment. The lack of optimal orientation for these two inputs resulted in a large portion of the projections captured not overlapping with the measurements captured by the other seven inputs. Therefore, in the subsequent tomographic reconstruction, either a significantly smaller volume (that which all nine FBE views overlapped) would be reconstructed, or the measurements captured by the 8th and 9th inputs would be ignored. This work decided on the latter approach and did not include the measurements from the 8th and 9th FBE inputs in the reconstruction process.

The key component of these diagnostics, the customized FBE bundle, is detailed in Figure 4.5. Figure 4.5a shows the nine separate input arms that are integrated into a single output. The nine input arms were designed to different lengths, with three being 1 meter
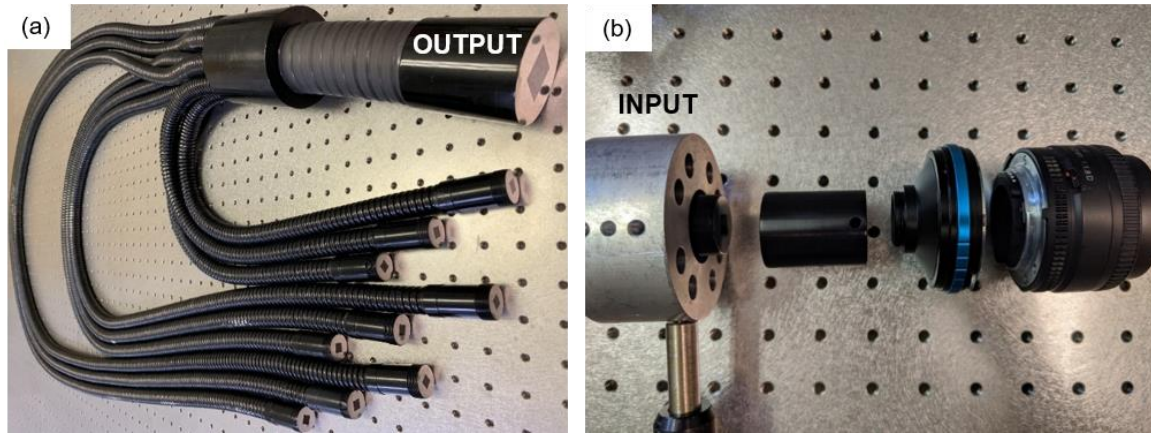
Figure 4.5: Photo of the customized nine-to-one FBE bundle, where a) shows the full bundle with different arm lengths, and b) is a close-up of one input arm and the lens integration

long, three being 2 meters, and three being 3 meters. The purpose of such a design was to allow the input arms to accommodate the different distances from each viewport to the camera and to reach different viewports flexibly. Each individual FBE input contained a 470×470 array of individual fiber filaments, each with an approximate diameter of 18 μm, that are packed in a square arrangement. With nine input arms, there were a total of 1,988,100 ($9 \times 470 \times 470$) image elements in the output end. The number of individual fiber filaments and the total number of imaging elements were designed such that the FBE would not be the limiting factor in spatial resolution compared to the single camera. More specifically, if the number of imaging elements from the FBE output was significantly fewer than the number of camera pixels, then a large part of the pixel resolution of the camera would essentially be wasted. Conversely, if the number of fiber image elements was significantly greater than the number of pixels, then a large portion of the imagining fibers would be wasted. The Photron SA-4 camera in this work had a maximum pixel resolution of 1024×1024 pixels, representing a reasonable match between the imaging elements in the FBE and the pixel resolution of the camera. With the camera focused on the FBE output end, the approximate resolution of each FBE output was 340×340 pixels.

Figure 4.5b shows a close-up of the input end assembly. Each input was held with an aluminum mount as shown on the left side of Fig. 4.5b. The input end was threaded, and

Figure 4.6: The calibration target within the ground vehicle testbed as seen from the outside, also showing the pool container, the propane torch, and some FBE input ends

an adjuster (the part immediately to the right of the input end) with matching thread was custom fabricated so that the left end of the adjustor could be assembled to the FBE input and finely tuned for focusing purposes. The right end of the adjustor was also threaded so it could be assembled to a lens adapter, to which a lens could then be attached. In this work, a Nikkor 50 mm lens was used for each input arm. A single locking mechanism was also fabricated on the adjustor to lock the alignment once it was finely tuned.

In order to determine the precise location of each FBE input (the distance to the target, and the azimuthal and inclination angles), a view registration process was performed. To begin, a calibration target, a flat plate with a checkerboard pattern with precisely known dimensions, was placed at the expected location of the flame. The calibration target was mounted on a rotational stage and images of it were captured at various angles by each of the FBE inputs. Figure 4.6 shows the calibration target within the testbed, which was placed near the center of the container that would later generate the pool flame, and a short distance in front of the propane torch, where the center of both flames was expected to be. Due to the difficult lighting conditions and unstable platform
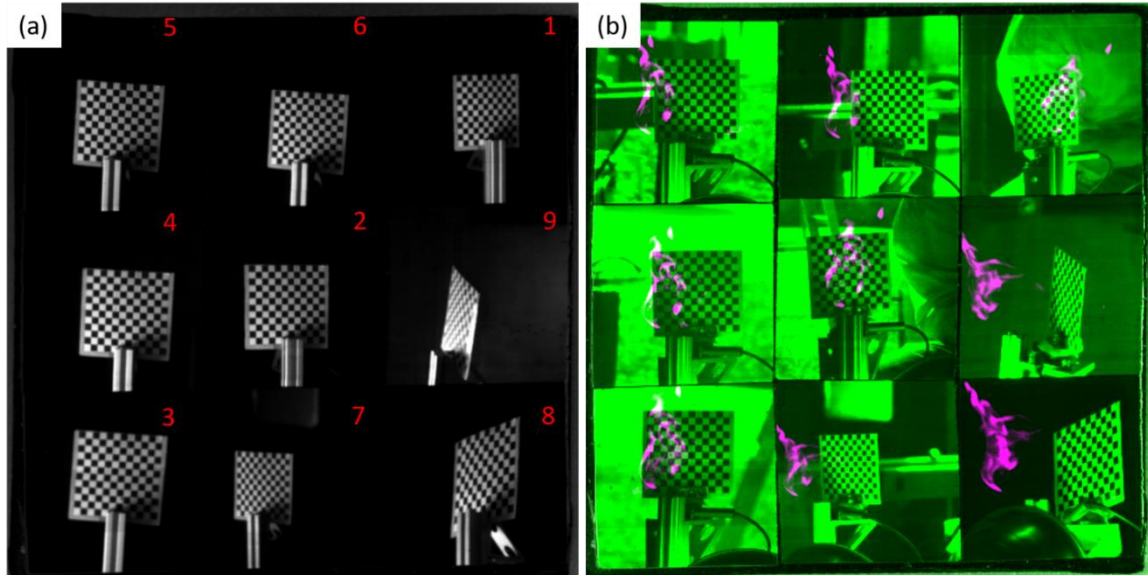
Figure 4.7: Projections of the calibration target as viewed from the nine FBE inputs, a) just the illuminated target numbered with increasing θ, and b) an overlay of the propane torch flame (purple) with the target

to which it was mounted, challenges were present in calibration that do not typically exist under laboratory conditions, and some of these challenges are addressed in a later section.

Figure 4.7 shows two examples of the simultaneous projections from each of the nine FBE inputs, as viewed on the output end by the camera, with Fig. 4.7a showing just the illuminated calibration target with FBE inputs labeled according to Fig. 4.4a. From this particular orientation, the view from the 9th input in Fig. 4.7a is not of high enough quality to use in the view registration procedure due to the steep viewing angle of the flat plate. To combat this problem, and also to offer more views to constrain the view registration algorithm, the calibration target was placed on a rotational stage and multiple sets of projections, like those pictured in Fig. 4.7a, were taken at a multitude of known rotational angles. Figure 4.7b shows a similar photo, but with an overlay of the propane torch flame (purple) to illustrate the challenges of aligning the calibration target with the target flame, and also to show the significant positional discrepancy for the 8th and 9th FBE inputs with respect to the calibration target, as mentioned earlier.
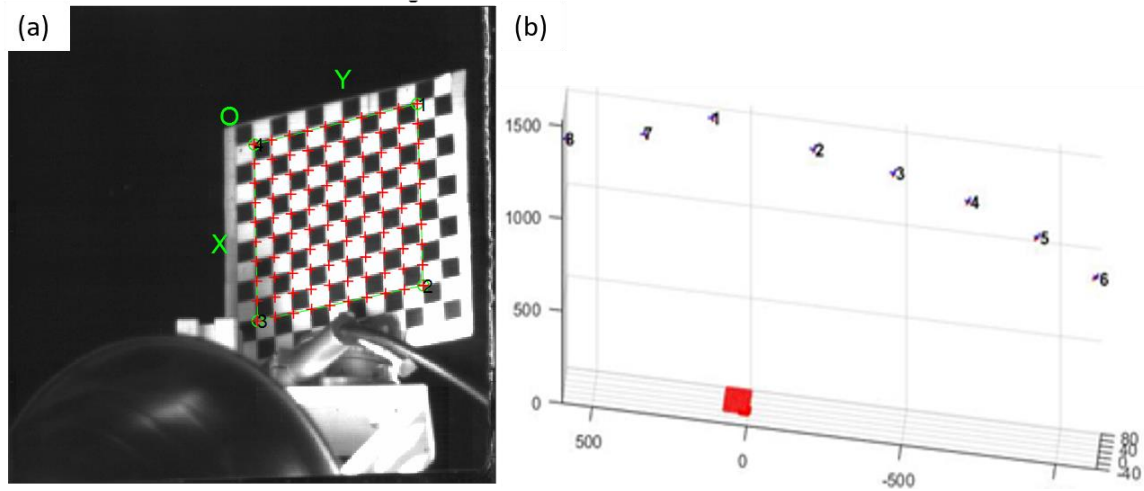
Figure 4.8: a) The view registration detection of the checkerboard pattern on the calibration target, and b) the calculated orientations of a single FBE input with respect to the calibration target (red) across eight known rotational positions

The view registration algorithm used in this work is an open-source MATLAB program that can infer the location and orientation of cameras based on the magnification and distortion of the known pattern of the calibration target [93]. In this case, the images from each FBE input of the calibration target at the known rotational positions were used in the view registration algorithm, which identified the checkerboard pattern on each image to infer the orientation for each image and, ultimately, determine the position of the FBE input. Figure 4.8a shows an example of the view registration detection for one view. For most FBE inputs, eight images of different known rotational positions were of high enough quality to use in view registration. Figure 4.8b shows the eight calculated orientations of a single FBE input from the perspective of the calibration target (red). Each of the known rotational positions were separated by $\theta = 10°$, however, there is obviously a slight discrepancy shown in Fig. 4.8b, illustrating the degree of view registration and subsequent measurement error. To account for the view registration error, the average position and orientation values were used for each FBE input.

Finally, after performing the calibration and view registration, one final step was performed to optimize the view angles and reduce reconstruction error due to misalignment. In this step, a quick reconstruction was performed with a limited number of

Table 4.1: The view angles for each FBE input arm as determined by view registration. Views were labeled 1 through 9 with increasing θ.

View	1	2	3	4	5	6	7	8	9
θ(°)	-31.9	-16.8	0.1	6.0	13.3	20.6	35.7	50.9	72.4
φ(°)	85.7	86.2	87.1	86.0	86.1	87.7	86.3	130.9	70.0

views, beginning with three, using the calculated orientations from the view registration. Each angle was changed a small amount at increments of 0.5° in an iterative way until the minimum projection error was found using a sample instantaneous measurement. Once this minimum error was found, the same view angles were used while then including an additional view that underwent the same iterative minimization procedure. Additional views were added in this manner until all seven views were optimized. A similar yet more sophisticated process has been developed, called Reconstruction Integrating View Registration (RIVR), where an internal feedback mechanism can optimize the view orientations while simultaneously performing the 3D reconstruction [94, 95]. However, this technique was not fully developed at the time the work in this chapter was performed. The final set of view orientations were then used for all subsequent reconstructions, and the final angular positions for each FBE input are shown in Table 4.1. Note that the orientations for views 8 and 9 are directly from the view registration and were not optimized or used in reconstruction, as mentioned. As seen in Fig. 4.3, and shown schematically in Fig. 4.4a, views 1 through 7 were on the front side of the testbed and were oriented with a relatively shallow inclination angle, no more than 5° above the horizontal. However, due to the geometry and placement of the viewports on the testbed, the 8th and 9th FBE inputs, located on the side of the testbed, had much steeper inclination angles measured from the horizontal of 40.9° and -20°, respectively. These greater inclination angles compounded the difficulty of obtaining measurements of sufficient quality and accuracy from these views, which is why they were ultimately omitted from the tomographic reconstructions.
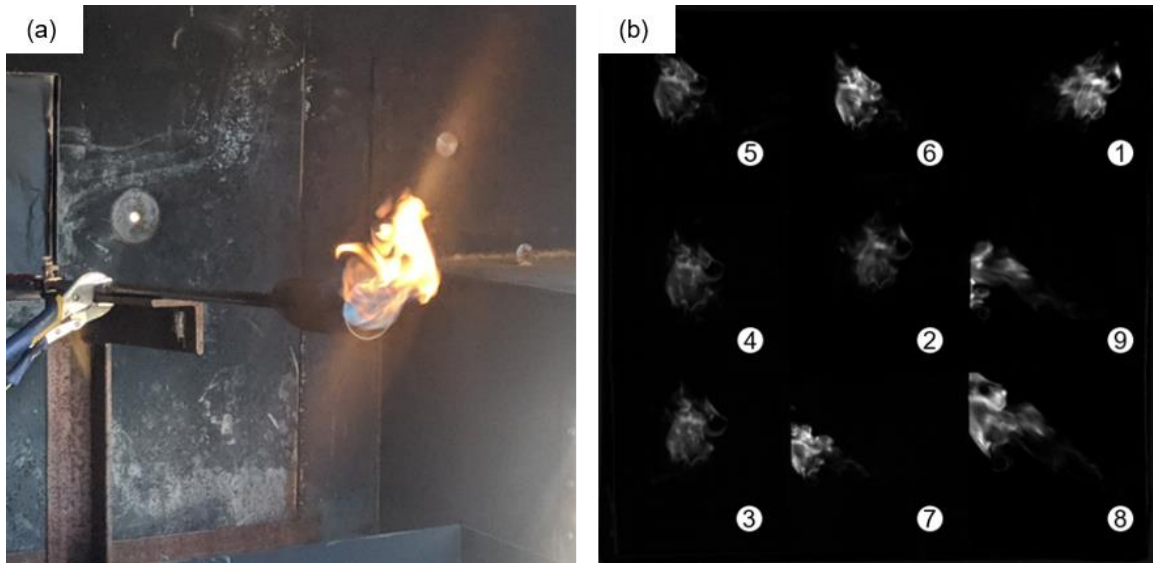
Figure 4.9: Images of the propane torch flame, a) photo taken from outside the testbed, and b) projections from the nine FBE inputs as taken by the single camera

4.3. Experimental Procedure

After the view registration procedure was complete, experimental data was taken under two different flame conditions: using a propane torch and an F24 jet fuel pool flame, which is a kerosene-based fuel. While both flames were smaller than those expected under realistic conditions, the primary focus of this measurement campaign was to develop a proof-of-concept setup that could be implemented under even more realistic conditions. The signal emitted from both the propane torch and pool flame was likely a combination of two emission mechanisms: incandescence caused by blackbody radiation of unburned soot molecules and chemiluminescence from excited radicals in the flame, typically OH* and CH* [26, 86, 96]. In both cases, the emission is in the visible range and could be collected by a camera without any supporting filters. The first set of data taken was using a propane torch that was situated such that the middle of the flame was expected to be near the center of the calibration target. Figure 4.9a shows a photo of the lit propane torch within the testbed, and Fig. 4.9b shows an image of the nine different projections as seen from the output end of the FBE bundle. Once again, it is clear that the flame as viewed from the 8th and 9th FBE inputs is significantly out of frame and would not be usable for tomography.
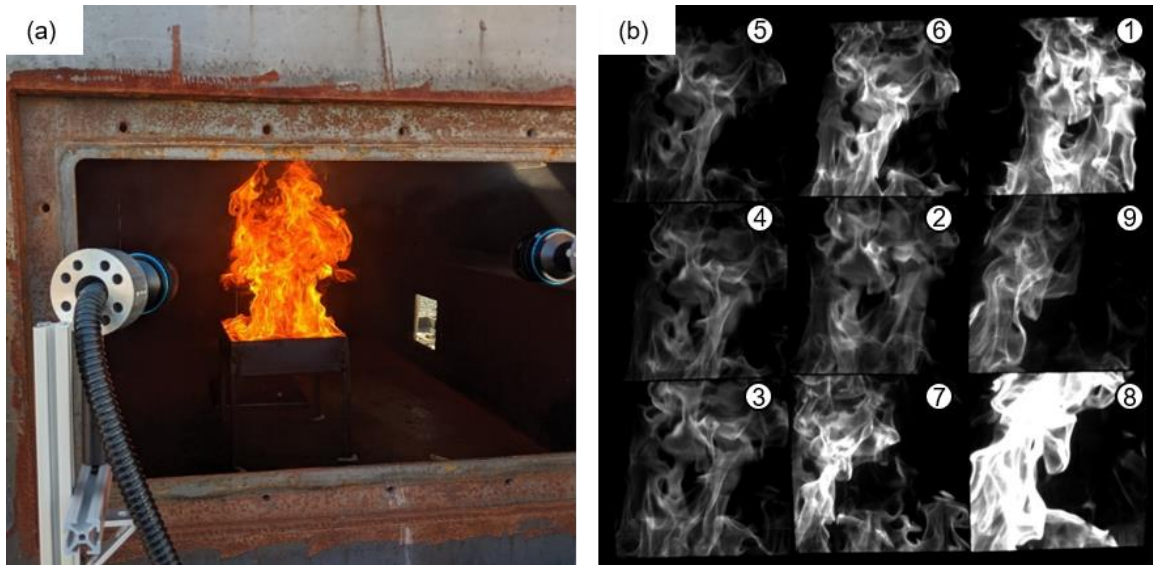
Figure 4.10: Images of the pool flame, a) photo taken from outside the testbed, and b) projections from the nine FBE inputs as taken by the single camera

Throughout the measurement campaign, a variety of exposure times and aperture sizes on the FBE inputs were used with the primary goal of obtaining sufficient signal-to-noise ratio, secondly to maintain a high enough temporal resolution to resolve the flame dynamics, and lastly to achieve approximately the same signal level across all FBE inputs. Such a routine set of objectives was difficult to achieve simultaneously under field conditions, particularly keeping the signal level equal across all views, as seen in Fig. 4.9b. This is due to the possible variation in aperture size for each FBE input, the various distances of the inputs to the flame, and signal attenuation from transmission within the fiber optics. However, an acceptable signal-to-noise ratio and temporal resolution could be achieved under an operational frame rate of 500 Hz with an exposure time of 2 ms for the propane torch and 1 ms for the pool flame, and these parameters were used throughout the remainder of this chapter.

After data was captured from the propane torch, it was removed from the testbed to prepare for the pool flame measurements. F24 jet fuel was used as the fuel source, which was poured into the rectangular container that held the calibration target in Fig. 4.6. The fuel was ignited and generated much larger and more turbulent flames than the propane

torch. Figure 4.10a is a photo of the pool flame seen from outside the testbed, illustrating its size and turbulence compared to the propane torch flame. Figure 4.10b, similar to Fig. 4.9b, shows the nine different simultaneous views taken by the single camera. Based on the location of the calibration target and the magnification of the FBE input views, measurements were taken of approximately the top half of the entire pool flame pictured in Fig. 4.10a. For this reason, some instantaneous measurements of the pool flame contained very little signal, as the flame was relatively short during these moments. As another challenge, the signal level discrepancy is apparent once again, as the view from the 8th FBE input is nearly completely oversaturated. The oversaturation of the signal, which is occasionally present across multiple views and instantaneous projections, causes an irrevocable loss of data that makes including the measurement in the tomographic reconstruction difficult, if not impossible, while maintining high reconstruction fidelity. This can also be a reason why some views may be omitted from the reconstruction in addition to physical misalignment.

Before the measured projections of either flame could be used as inputs for tomographic reconstruction, some image post-processing was required. The image post-processing procedure involved cropping, centering, and normalizing the signal level and magnification across all views used. The magnification was normalized by scaling the size of each view such that the height of the calibration target was equal, modified by the calculated inclination angle, and the signal level was normalized in such a way that the sum of the signal on each view would be equal. By normalizing the signal level and magnification, the reconstruction algorithm treated each view as having been the same distance from the flame center. Given the large uncertainty in the position and orientation of each FBE input, this method showed the most promise in achieving usable results, as opposed to trying to tune the signal level (which differs greatly across all views) to match their distance from the flame. The measurements from each FBE input were cropped and centered in such a way that the center pixel of each image corresponded to a line of sight through the center voxel of the reconstructed measurement volume. While a perfect alignment would make this step unnecessary, such a setup was unachievable due to the logistical limitations on-site (i.e. the short amount of time to set up and collect data and the unstable surfaces for FBEs, camera, calibration target, and flame). After image post-
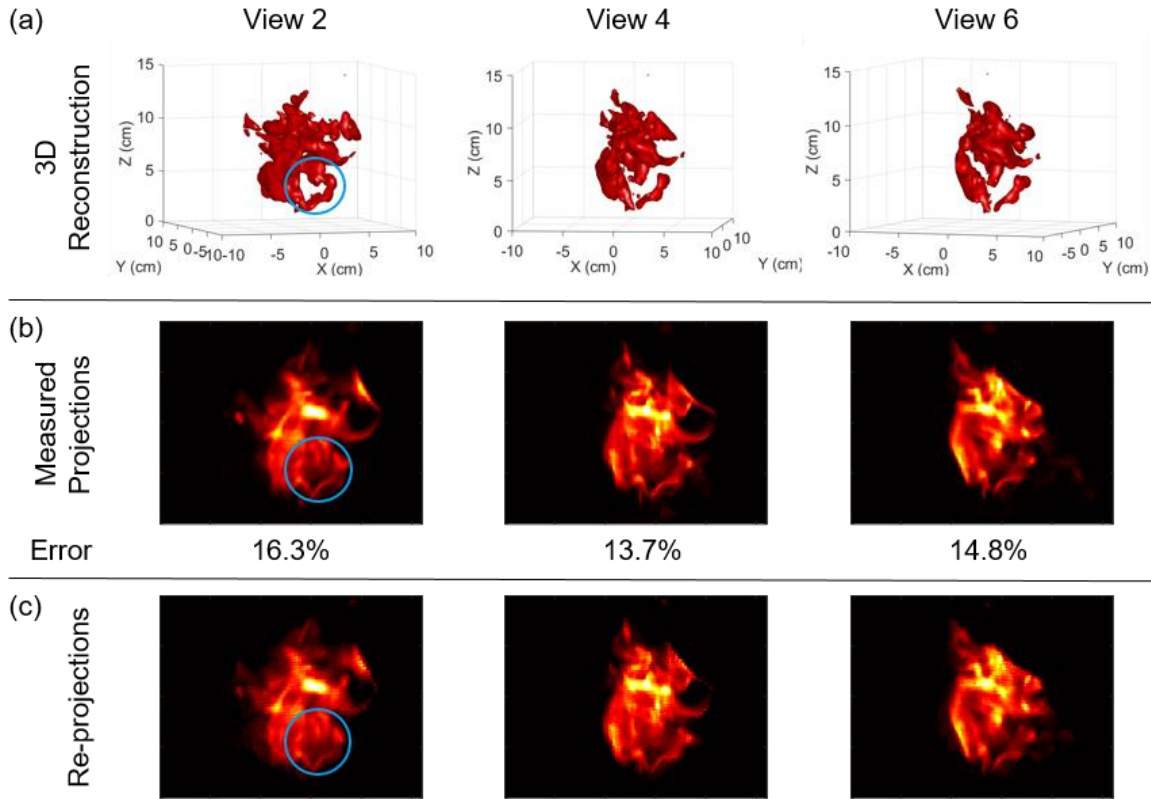
Figure 4.11: Comparison between a) a set of 3D reconstructions of the propane torch flame, b) the measured projections at the corresponding views, and c) the re-projections at the corresponding views, showing the qualitative similarities, as well as the projection error between (b) and (c). A feature has been circled to show the level of detail achievable in the reconstruction.

processing, the projections were used as inputs in the tomographic reconstruction algorithm.

4.4. Results and Analysis

For the propane torch data, views 1 through 7 were used in the tomographic reconstruction, and each of the seven projections was cropped to a pixel resolution of 260 × 200 pixels, resulting in a total of 3.64×10^5 pixels (the total number of inputs). The dimensions of the reconstruction volume were 19.2 cm (width) × 19.2 cm (depth) × 15.0 cm (height), which was discretized into $76 \times 76 \times 58$ voxels, resulting in a total number of voxels of 3.35×10^5 (the number of unknowns variables to be solved). With this

discretization, the voxel resolution was 0.25 cm in each dimension. For both the propane torch and the pool flame reconstructions, the masking technique was used to expedite the reconstruction time of the hundreds of frames. A thick buffer region was included to eliminate any detrimental effects due to the substantial misalignment and view registration error. Figure 4.11 shows the results of the reconstruction of a single instantaneous measurement of the propane torch flame as viewed from three of the seven views used. Figure 4.11a shows the reconstruction as an isosurface, where the isosurface value was chosen that best represented the flame's surface and was derived in a similar way to the binary threshold value described in Chapter 3. Figure 4.11b shows the measured projections for the same three views shown in the top row and can be visually compared to see that the reconstruction accurately captured the bulk flame features. Figure 4.11c shows the re-projections simulated from the 3D reconstruction at the same three views, and a visual comparison between these and the measured projections shows them to be similar at both large and small scales. As a specific example, the circled region in view 2 of Figure 4.11 shows a uniquely shaped hole that can be clearly seen in the reconstruction, demonstrating the reconstruction fidelity.

In previous chapters, a quantitative assessment of accuracy was possible by directly comparing the reconstruction to either the known phantom distribution or a ground truth acquired by more accurate means. However, in this study, there is no known distribution to which the results can be compared. Here, the quantitative comparison can instead be performed by examining the error and correlation between the measured projections and re-projections. Ideally, the re-projections would be identical to the measured projections for each view, indicating a perfect reconstruction. This work calculated the projection error (e_p) between the measured projections (p) and the re-projections (p^r) as defined below:

$$e_p = \frac{\sum_i \sum_j |p_{i,j} - p^r_{i,j}|}{\sum_i \sum_j |p_{i,j}|},$$
(4.1)

where i and j represent the pixel indices of the projections.

Figure 4.11b shows the projection error between the corresponding measured projections and re-projections for the three views shown, and the errors ranged from 13.7%

to 16.3% with an average of 14.7% across all seven views. The projection error is higher than what would normally be deemed acceptable based on earlier characterization of measurements performed in more controlled environments, indicating a significant error in view registration and signal normalization [31, 88]. However, the projection error alone does not provide a full characterization of the reconstruction fidelity. For example, an otherwise perfect 3D reconstruction with only a spatial shift from the true distribution would result in a large projection error. Therefore, to complement the characterization of reconstruction accuracy, the projection correlation (ρ) was used and is defined as:

$$\rho = \frac{cov(p, p^r)}{\sigma_p \sigma_{p^r}}, \tag{4.2}$$

where cov is the covariance between the two projections, and σ is the standard deviation of the pixel intensities for each projection. In the example of a perfect reconstruction with only a spatial shift, the correlation would be $\rho = 100\%$. Across the seven views used for reconstruction, the average correlation between the measured projections and re-projections was 98.9%, indicating a satisfactory level of reconstruction accuracy in terms of capturing the 3D spatial structures based on the earlier characterization. While the relatively large error illustrates the challenges in alignment during field tests, the large correlation shows that the overall structure and dimensions of the flame can still be accurately reproduced.

A similar procedure was performed on the pool flame data. Again, only views 1 through 7 were used during reconstruction for the same reason as the propane torch, and each projection was cropped to 320×260 pixels, resulting in a total of 5.82×10^5 pixels. The reconstruction volume had dimensions of 35 cm (width) $\times$ 35 cm (depth) $\times$ 29 cm (height) and was discretized into $88 \times 88 \times 72$ voxels, for a total of 5.58×10^5 voxels. Due to the much larger measurement volume and only a relatively small increase in total pixels, the voxel resolution for the pool flame was 0.40 cm in all three dimensions. Similar to Fig. 4.11, Fig. 4.12 shows the reconstruction results for three views of the pool flame, with Fig. 4.12a being the 3D reconstruction as an isosurface, 4.12b being the measured projections, and 4.12c being the corresponding re-projections. Once again, upon visual inspection, the reconstruction captured the large-scale 3D features of the flame correctly. Also, the re-
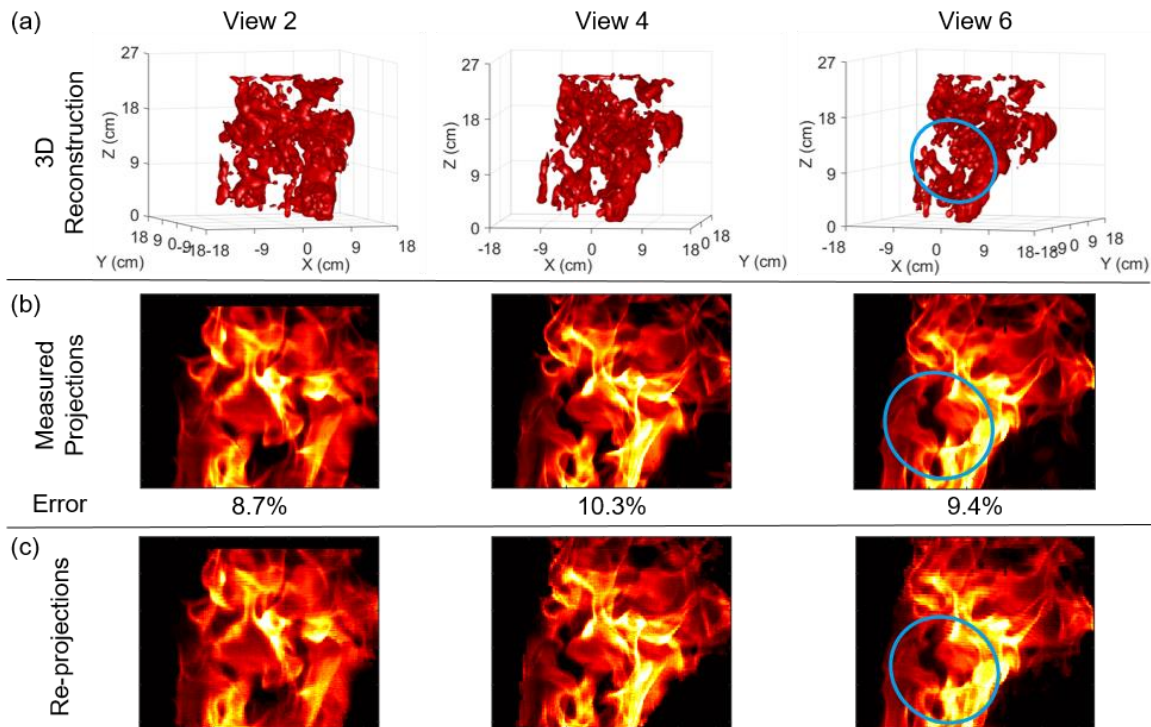
Figure 4.12: Comparison between a) a set of 3D reconstructions of the pool flame, b) the measured projections at the corresponding views, and c) the re-projections at the corresponding views, showing the qualitative similarities, as well as the projection error between (b) and (c). The circled features show that detailed regions of the flame could be accurately reconstructed.

projections and measured projections matched closely, both at an overall and detailed level. As a specific example, the circled region in view 6 shows three uniquely shaped holes in the flame structure that can be compared between Figs. 4.12a, b, and c, again illustrating the fidelity of the tomographic reconstruction. The projection errors for the three views are also shown in Fig. 4.12b, and they range from 8.7% to 10.3% with an average of 9.3% across all seven views. This error is quite a bit smaller than that of the propane torch, indicating that the alignment was less of an issue for this dataset. This may be the case due to the much larger size of the flame, where more of the measurement volume is occupied with signal. For example, if the signal distribution were a single point source, any misalignment would show no agreement between the views, and the projection error would be very large. Similar to the propane torch, the average correlation across the seven views

Figure 4.13: Comparison between the 3D reconstruction (top) and the corresponding measured projections (bottom) at consecutive time frames of the propane torch flame. A key feature is outlined as it moved from the t = -6 ms to t = 0 ms frame and its rate of growth calculated.

used was 98.9%, again indicating that the overall flame structures were accurately reconstructed.

As previously mentioned, data for both experimental conditions was captured at 500 Hz, which was sufficiently fast to resolve the temporal dynamics of the flame while simultaneously allowing for an adequate signal level. To demonstrate the 4D capabilities of the experimental setup and tomographic reconstruction, a temporal analysis of various flame parameters was carried out. For both the propane torch and pool flame, the motion of some key flame features was calculated, as well as the rate of change of the flame surface area, both based on the 3D isosurface of the reconstruction. Figure 4.13 provides an example of the temporal evolution of the propane torch flame, illustrating the 3D capabilities of high-speed tomography. The top row of Fig. 4.13 shows the 3D reconstructions evolving with time at 2 ms increments, while the bottom row shows the corresponding measured projections for visual comparison. The t = 0 ms frame is the same as that shown in Fig. 4.11. The 4D data shown in Fig. 4.13 provides both temporal and spatial information about the flame, such as the location of the extent of the flame in 3D, and also the temporal propagation of the flame. As a specific example, the 4D measurements revealed that the flame feature highlighted in the blue box was moving radially outward with a velocity of 12.9 m/s. This was calculated based on the rate of
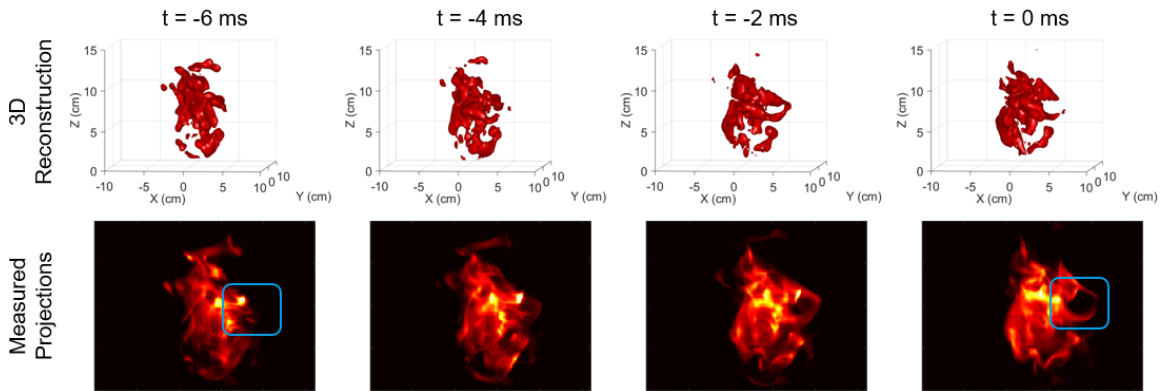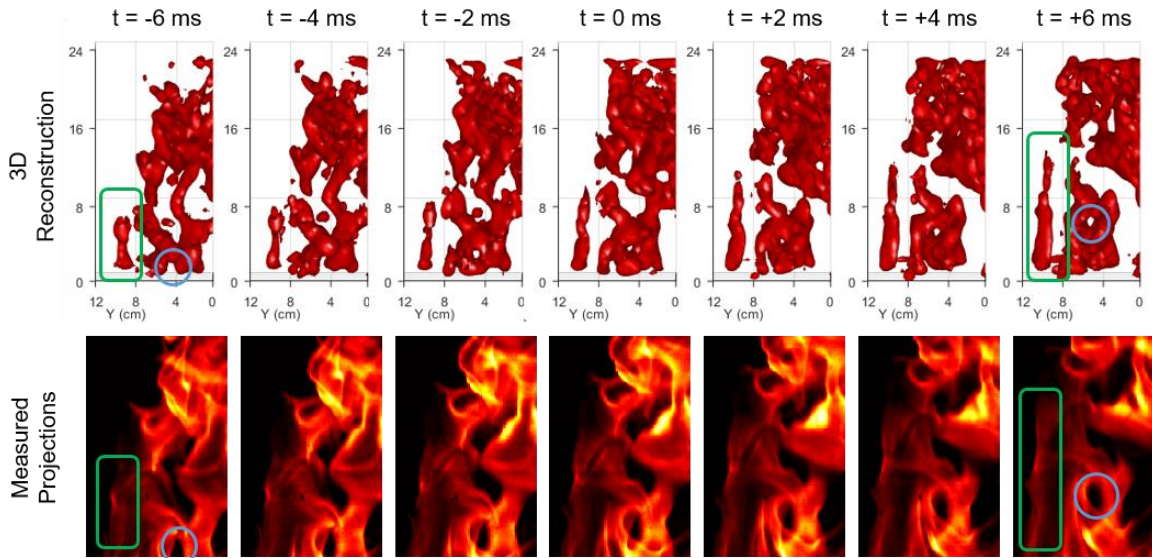
Figure 4.14: Comparison between the 3D reconstructions (top) and the corresponding measured projections (bottom) at consecutive time frames for the pool flame. Two key features are outlined as they moved from t = -6 ms to t = +6 ms and their rates of growth calculated.

change of the distance of this feature from the center of the measurement volume based on the isosurface value displayed. The velocity was measured by dividing the distance traveled by the feature between t = -6 ms and t = 0 ms. Considering the laminar burning velocity of a propane-air mixture is approximately an order of magnitude slower than this measurement, it can be determined that the predominant factor in the rate of growth of this flame is the direction and speed of the flow [97]. This observation is strengthened by the fact that the direction of flow was approximately in line with the velocity vector of this key feature. The measurement of this velocity was enabled by the 4D nature of the reconstruction, as such radial and depth motion are difficult or infeasible to obtain from 2D measurements due to their line-of-sight limitation.

A similar temporal analysis was performed on the pool flame. Figure 4.14 shows the temporal evolution of a segment of the flame over 12 ms, with the top row being the 3D reconstruction and the bottom row being the corresponding measured projections. The t = 0 ms frame is the same as that shown in Fig. 4.12. Again, some key flame features are highlighted in Fig. 4.14: a pillar-shaped feature (highlighted in the green rectangle) and a

hole (highlighted in the blue circle). First, the pillar-shaped feature was difficult to discern as a distinct feature from the 2D measurements in the bottom row, again due to their line-of-sight nature, while the 4D measurements in the top row clearly resolved it. Second, the motion of both features can be seen to be predominantly vertically upwards from both the 2D and 4D measurements, and the vertical speeds of the features were calculated to be 5.0 m/s for the pillar and 5.9 m/s for the hole. Due to the mostly vertical motion of the key flame features, it is estimated that the vertical evolution of this flame is primarily driven by upward convective flow. These measurements are in line with expectations of convective heat rise in a container, with an estimated vertical velocity between 5 – 10 m/s. These 4D measurements also revealed small depth-wise motion for these features, and other regions of the flame, that cannot be resolved from the 2D projections.

In addition to inspection of the time evolution of specific flame features, the time evolution of flame surface area was also calculated. While both the feature velocity measurements and surface area measurements relied on the isosurface, it should be noted that the surface area measurements are much more sensitive to the isosurface value, and these measurements shown are more useful to inspect the relative temporal change of surface area as opposed to the true flame surface area. In addition to their sensitivity to isosurface value, the surface area measurements are also sensitive to the spatial discretization of the reconstruction with respect to the smallest spatial structures within the flame for similar reasons as the flame perimeter measurements in Chapter 3. In Chapter 3, the smallest spatial structures visible were limited by the thickness of the thin reaction layer, and more specifically the presence of CH near the reaction layer. However, in the case of the diffusion flames in this work, where hot soot is expected to be the primary source of signal, there is not such a well-defined region where signal is expected, especially as soot has been shown to diffuse throughout the flame quickly as a function of distance from the ignition source [98]. For this reason, it is very difficult to estimate the smallest measurable scale and therefore the maximum spatial resolution that could be desired. However, due to the use of a single camera and the large measurement volumes for both flames, it is likely that the spatial resolution achieved in this work is not sufficient to resolve the smallest turbulent structures within the flow, and thus the surface area measurements

78

Figure 4.15: Time-evolution of the surface area of the propane torch flame based on different isosurface values, taken over 70 consecutive frames at 2 ms intervals

here are likely to be considerably smaller than that measured with higher accuracy and resolution.

To calculate the surface area of the reconstruction based on the displayed isosurface, the sum of the area of each triangular face that makes up the isosurface patch was taken. This step was performed for each instantaneous measurement's reconstruction and the time-evolution could then be examined. Figure 4.15 shows the time evolution of the surface area measurements (in cm^2) for the propane torch flame over the course of 140 ms (70 consecutive frames) using three different isosurface values that varied by 10% of each other. Note that the middle value of 9.0E-6 was the value used to display the flame earlier in Figs. 4.11 and 4.13. As mentioned, the surface area measurements were dependent on the isosurface value chosen, but Fig. 4.15 demonstrated that the relative change of surface area was consistent across different isosurface values and thus the overall trend could be analyzed based on these measurements. During this short period of time (140 ms), there was substantial variation of the flame surface area, indicating that a temporal resolution of at least 2 ms was required to accurately resolve the flame evolution.
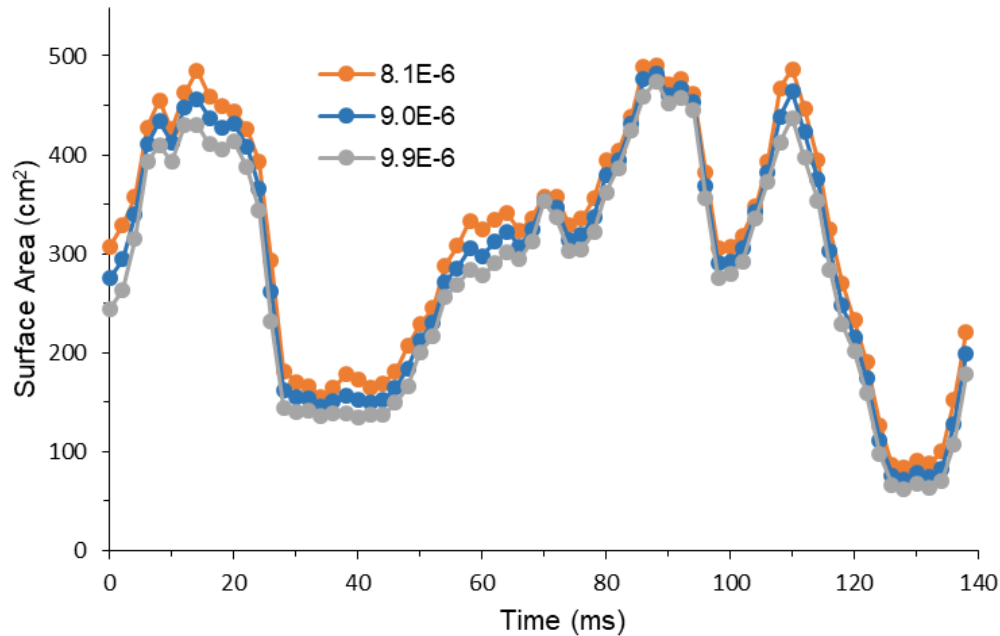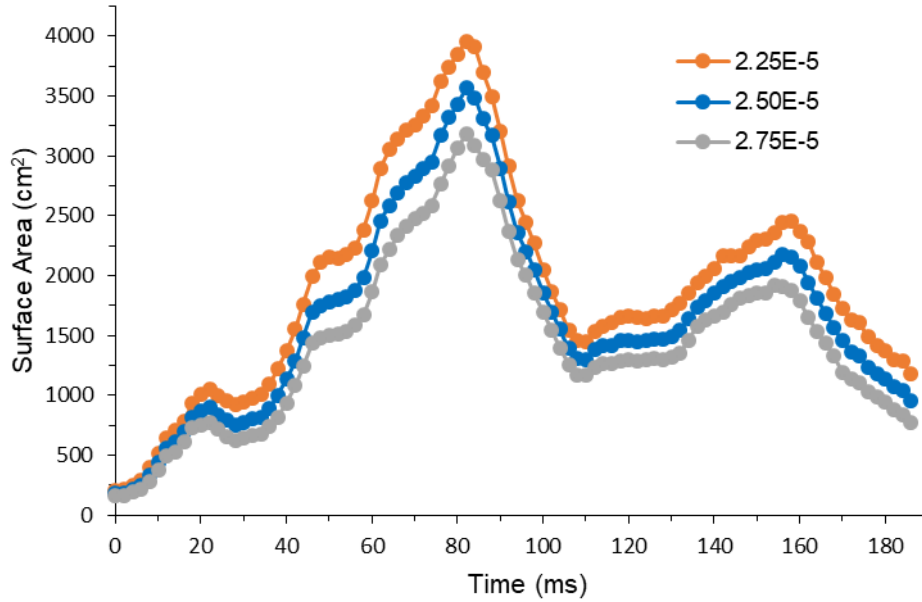
Figure 4.16: Time-evolution of the surface area of the pool flame based on different isosurface values, taken over 94 consecutive frames at 2 ms intervals

In particular, the fastest change in flame surface area was from 431.9 to 162.0 cm^2 between 20 and 28 ms at an average rate of 33.7 cm^2/s. In this particular subset of data for the propane torch, the flame was almost always entirely within the reconstruction measurement volume, and thus the changes in the measured surface area could be explained by variation within the flame signal.

In a similar way to the propane torch, surface area measurements of the pool flame were taken and are shown in Fig. 4.16, again using three different isosurface values that varied by 10% of each other. Once again, the absolute surface area measurements were sensitive to the chosen isosurface value, but the temporal trend remained the same. While the overall variation in surface area for the pool flame was greater than that of the propane torch, with the fastest rate of change being 118.7 cm^2/s (between 60 and 64 ms), the relative rate of change of surface area was slightly lower, again illustrating that the temporal resolution of 2 ms was sufficient to capture the flame evolution. Unlike the propane torch, the variation in flame surface area came from two major sources: the natural variation in flame signal, and the presence of flame signal within the measurement volume. While the propane torch existed almost entirely within the reconstructed measurement volume, the

80

measurement volume for the pool flame only resided around the top of the entire volume that the pool flame occupied. For this reason, during times when the pool flame was relatively short, there could be little to no signal captured by the FBE inputs, and thus very little surface area. This was especially the case near the beginning and end of the data shown in Fig. 4.16, which is why the surface area is so small.

Due to the vast amount of data taken at such a high frame rate and the limitations of data storage and transfer, only up to one second of data was taken at a time (500 frames at 500 Hz), which limited the ability to obtain time-averaged measurements that would better characterize the flames as a whole. However, the primary goal of this measurement campaign was to show that such 4D tomographic setups are possible under field conditions, which was achieved.

4.5. Summary

This chapter demonstrated the *in situ* imaging of 4D fire events within a ground vehicle testbed under field conditions as part of an ongoing campaign to characterize the volatile flames encountered in vehicle fire situations. Using a customized 9-to-1 FBE bundle, time-resolved measurements taken at 500 Hz were taken with a single camera located a safe distance away from the testbed. Measurements of both a propane torch and a pool flame were taken, with measurements volumes of 19.2 cm (width) × 19.2 cm (depth) × 15.0 cm (height) and 35 cm × 35 cm × 29 cm, respectively. The FBE-based diagnostics overcame several key challenges of obtaining time-resolved measurements of large flames under field conditions, including equipment cost, equipment safety, optical access, and the relatively large measurement volume and hostile measurement environment. During this measurement campaign, the design of the diagnostic setup has also been shown to be sufficiently robust for the transportation between University of Virginia (Charlottesville, VA) and ARL APG (Aberdeen, MD), and for the transportation, assembly, alignment, and disassembly within three days. To the author's knowledge, this is the first time that *in situ* 4D measurements under such field conditions have been reported.

The 4D measurements were obtained by using a tomography algorithm to determine the temporally-resolved 3D signal distribution of the flame based on the simultaneous measurements taken by the single camera with nine distinct views from the FBE inputs. During the tomographic reconstructions, the pixel masking method was employed with a sufficiently large buffer region to reduce the vast computational time of reconstructing the many instantaneous sets of measurements without sacrificing accuracy. A large buffer region was required due to the inaccuracy of the view registration procedure in determining the view orientations of each of the nine FBE inputs, which was a consequence of the challenging setup under field conditions. As another method to alleviate the issues of misalignment, a view angle optimization routine was performed to slightly alter the view angles used in reconstruction in such a way that minimized the reconstructed projection error, and these optimized view angles were used for all subsequent reconstructions from this data set.

Based on the 4D tomographic measurements, the temporal evolution of the flame's 3D signal distribution was observed. Measurements of the rate of flame growth and propagation are particularly useful in studying fire events within enclosed containers like ground vehicles, where human lives are at stake. Understanding the rate at which these rapidly evolving flames can grow can inform the design of safety systems, such as automatic fire extinguishing systems, to protect the lives of the occupants. Towards this goal, the temporal evolution of the flame's extent and surface area were calculated. For both the propane torch and the pool flame, key features were identified in 3D that would otherwise be difficult or impossible to identify from purely the 2D line-of-sight projections alone, and the motion of these features was calculated. Additionally, based on an isosurface of the 3D reconstruction, the surface area of the flames was estimated and their temporal evolution was observed. These measurements showed that even under such short time scales there was significant evolution of the flame surface, and the frame rate of 500 Hz was near the minimum required frame rate to fully capture this evolution, further demonstrating the need for high-speed flame measurements.

There were many limitations and challenges encountered during these experiments that needed to be overcome. First, it turned out to be quite difficult to achieve a routine set

of alignment objectives under field conditions, namely, maintaining a sufficient signal-to-noise ratio, sufficient temporal resolution, approximately the same signal level across all FBE inputs, and accurate alignment of view orientations. While additional time and care could improve the quality of the alignment and projections, these factors will always remain a challenge under field conditions. Second, the lengths and placements of the FBE input arms could be designed to better suit the specific field conditions. In particular, the lengths of the two furthest FBE arms were too short to make the alignment stable and easy. As a result of this, the views from these two input arms were not used in the reconstruction. One obvious solution would be an FBE bundle with longer arms, but the additional arm length would likely lead to greater signal attenuation. Another solution could be to perform a more systematic analysis of the possible positions for the FBE inputs and camera to optimize placement with the given hardware. Finally, and perhaps most importantly, the use of a single camera placed a limit on the maximum spatial resolution achievable in the reconstruction. The 1024×1024 pixels available on the camera used represented the maximum number of voxels that could be solved, and thus the maximum achievable spatial resolution, assuming every pixel was used optimally (which is never the case, especially under field conditions). If a finer resolution is required, for instance to resolve smaller structures within the turbulent flame, either a camera with greater pixel resolution or additional cameras would be necessary. Additionally, further studies to determine the chemical composition and relevant length scales that may be of interest should be performed. This work has demonstrated that even with the many challenges faced under field conditions and with limited hardware, 4D measurements of highly turbulent flames were achieved, and even relatively small-scale features could be resolved.

Chapter 5

5. Conclusions

5.1. Summary of Contributions

This dissertation outlines three projects that aim to advance the field of combustion tomography and diagnostics through progress in both data acquisition and data processing techniques. More specifically, two computational techniques were developed, validated, and analyzed which both exploit flame features to more intelligently use the information collected in the measured projections. Both techniques aimed to reduce the computational cost of tomography without a loss of accuracy, and in some cases even improving spatial resolution. In addition, towards improving data acquisition, a proof-of-concept demonstration using fiber-based endoscopes with a single camera enabled the visualization of flames under practical conditions, including limited space and harsh conditions. Time-resolved 3D flame measurements were collected that were able to resolve both the temporal dynamics and spatial structures of the flame.

Chapter 2 first describes an adaptive spatial discretization (ASD) technique that was developed to reduce the computational cost of computed tomography while simultaneously offering the capability to improve spatial resolution. The ASD technique exploits regions within the measured flame that have relatively low spatial gradients in signal intensity. As these regions do not require as great of spatial resolution, they may be reconstructed with larger and fewer voxels. The ASD technique can quickly identify these low-gradient regions and adapt the discretization of the measurement volume such that more and smaller voxels are only used in regions that require high spatial resolution, and larger voxels are used everywhere else. The primary contribution of this work is to reduce the computational cost by using fewer total voxels while maintaining reconstruction accuracy. As a secondary benefit, employing ASD allowed for a slight increase in spatial resolution and has shown to be more noise-resistant than the baseline method. The ASD

technique was validated and analyzed on six phantom cases that were designed to emulate a variety of distributions encountered in tomography applications, and the reconstructions were directly compared to the phantoms to assess the accuracy. Using 18 equally distanced, co-planar projections with an artificially added 3% Gaussian noise, the phantoms were reconstructed using the ASD and baseline methods, where it was found that the ASD method yielded a reduction in computational time of up to 50% while the reconstruction error increased by no more than 0.21% across all six cases. In a similar test to emulate real-world measurements more closely, a high-resolution phantom was projected onto the same views with significantly fewer pixels than voxels (thus limiting the information and maximum spatial resolution achievable). Under these tests, it was found that the ASD method not only reduced the computational time to achieve the same accuracy, but was also able to slightly reduce the error, and thus spatial resolution, in some cases.

Chapter 3 describes a pixel masking technique to similarly reduce the computational cost of tomography while maintaining, or even improving, reconstruction accuracy by exploiting a different feature common in flame measurements. In emission tomography, there are usually regions on the measured projections that do not receive any signal, and it can be inferred that all voxels corresponding to these pixels contain no emission. The pixel masking method identifies pixels that are below a determined noise threshold and removes these pixels and all corresponding voxels from the reconstruction. In doing so, fewer voxels are used in the reconstruction, thus reducing the computational cost to perform tomography while maintaining accuracy. Alternatively, more and smaller voxels may be used in regions of importance, allowing for the improvement of reconstruction accuracy and resolution. To alleviate the issue of error in the calculated camera orientations, as calculated by a view registration algorithm, a buffer region was added at the interface of masked regions within the measurement volume to prevent these voxels from being unintentionally removed. The thickness of the buffer region needed to maintain accuracy using masking was found to be 1.2 mm, based on the approximate $0.5°$ error in view registration. Validation and analysis of the masking method were performed using a direct comparison of flame front contour length between 2D PLIF measurements and a corresponding simultaneous cross-section of a 3D VLIF reconstruction of the flame. The target species in the LIF measurements was the CH radical produced by the CH_4-air

flame, for which the masking method is particularly well-suited due to CH only existing within a small region in the flame. Based on the contour length measurements, it was found that the masking method could achieve a 21% decrease in computation time while simultaneously decreasing the error by reducing the voxel size from 0.16 mm to 0.13 mm per dimension. An additional reduction in computation time could be achievable while simply maintaining accuracy if needed. Similar to the ASD method, the pixel masking technique proved to be another tool that can exploit flame features to reduce the computational cost of tomography without a loss, and in some cases a gain, in accuracy.

Finally, in Chapter 4 a proof-of-concept experimental design is demonstrated using FBEs in conjunction with a single camera to take time-resolved 3D measurements of turbulent flames within the confines of a ground vehicle testbed. Under practical conditions, there is typically limited space and view access to the target flames which makes obtaining multidimensional measurements difficult. Additionally, the conditions can be challenging to obtain accurate calibration and can also be hazardous to the equipment. For these reasons, there is a dire need for improved diagnostic setups for field measurements that can reduce the equipment cost and footprint and be flexible enough to utilize what limited view access exists. The use of FBEs greatly alleviated these issues to enable time-resolved flame measurements of two large, turbulent flames within the vehicle testbed, one being from a propane torch and the other a larger pool flame. These 4D measurements were used to resolve both the spatial structures and the temporal dynamics of the flames. For both flames, velocity measurements were calculated of key flame features and the temporal evolution of the estimated flame surface area. The pixel masking method was employed to reduce the computational requirements for such large-scale computations (a consequence of high-speed tomography at a frame rate of 500 Hz). To alleviate the significant error in the FBE input orientations, a large buffer region was added, and an iterative view angle operation was performed to minimize reconstruction error. From these experiments, it has been demonstrated that such an FBE-based setup could obtain 4D flame measurements under difficult field conditions and shows promise for other similarly challenging environments.

5.2. Future Work

Based on the work outlined in this dissertation, some additional avenues of potential research in the field of combustion tomography are discussed here. Broadly, the implementation of combustion tomography in more practical scenarios, particularly on a larger scale and under field conditions, is still relatively young. Also, the ultimate goal of obtaining real-time tomographic measurements of flames is still some distance in the future, with many more computational advancements (likely in both hardware and software) necessary. This section describes some potential advancements in both categories to make combustion tomography more widely applicable and more computationally efficient.

First, the ASD technique employed in this dissertation was limited to two zones: coarsely and finely discretized regions. However, depending on the application and the range of spatial gradients, as well as the need for very high spatial resolution in some regions, multiple regions of varying discretization could be used. This work found that, when using cubic voxels, there was not much benefit to three zones of discretization in the cases tested. This was due to the limitation of voxel size under this geometry, where the ratio of different voxel sizes is limited to the dimension cubed (a voxel that is 1/3 the width of another has $1/27^{th}$ the volume). The use of non-cubic voxels is one avenue to maximize the benefit of a multi-zone ASD method, although it is worth noting that there are other limitations to the maximum spatial resolution than simply the linear algebra limit, and thus the range of voxel sizes (and therefore the minimum voxel size needed) may be limited. An extension of this work would be to examine the potential benefits of combining the masking method and ASD, as they both exploit different characteristics in combustion measurements and tomography. However, when using ASD, regions that contain no signal and would therefore be masked are already treated with a coarse discretization, and these regions already occupy a small fraction of the overall computational resources.

The validation and analysis of the ASD method in this dissertation employed known phantom distributions and ASD has not yet been tested thoroughly on more realistic data. Applying ASD to a practical dataset is an obvious next step towards the validation of this technique. For instance, the data described in Chapter 3 would be a good candidate for

such tests, as the simultaneous PLIF and VLIF measurements offer the capacity for direct comparison using a well-established ground truth (the PLIF measurements). In fact, the simultaneous PLIF/VLIF setup is such a powerful diagnostic tool for validating new techniques that it would be worth investing resources to replicate the experiment using a high-speed setup to enable time-resolved measurements. Additionally, the data collected and described in Chapter 4 would be another good candidate for testing the ASD technique if not for the significant measurement and alignment errors in this dataset. In the future, similar time-resolved measurements would be useful in the validation of techniques while also offering the capability to test techniques similar to ASD, except applying an adaptive discretization to the temporal realm rather than (or in conjunction with) the spatial dimension. A final practical example where ASD would be a strong candidate is for flow particle image velocimetry (PIV) measurements. While tomographic PIV is relatively new and still developing, ASD would still be applicable to reduce the computational resources by focusing on areas where there are large velocity gradients (as opposed to signal gradients described in this dissertation).

The masking method used in this work exploited features found in the measured projections to improve the efficiency of performing tomography. In a similar way, one application of the ASD technique was to identify regions of large signal gradient based on the projections. However, while this particular application of ASD had some flaws (as discussed in Appendix A.2), more research efforts are warranted to identify features from the measured projections that can influence and inform the tomographic reconstructions.

Finally, the proof-of-concept FBE-based diagnostic setup described in this dissertation has shown to be a useful tool in overcoming many challenges of field measurements. As shown in Appendix section A.1, the same setup was modified to visualize simulated Mach 5 scramjet flames at the University of Virginia Hypersonics Research Complex. While there were additional challenges in obtaining these measurements, the flexibility of the setup was demonstrated again with a single camera. Given that spatial resolution is limited by the hardware used, the next step towards FBE-based field diagnostics would be to include multiple FBE bundles and cameras to improve the spatial resolution of the measurements and to expand the range of possible view angles.

Also, as mentioned, one of the key challenges in field measurements is obtaining accurate view registration for each FBE input. While this dissertation utilized an iterative approach to mitigate the error in orientations, other works have developed a more advanced technique called RIVR, but only in the application of tomographic PIV measurements so far. It would greatly benefit practical combustion diagnostics if RIVR were used in conjunction with an FBE setup for field measurements, potentially reducing one of the more challenging aspects of practical measurements. In addition, a more comprehensive 3D analysis could be performed before such large-scale setups to optimize the placements of each FBE input to maximize the obtainable information. Finally, in characterizing the flames that are present under these vehicle fire situations, smaller-scale laboratory tests should be performed on more laminar flames using the same fuel type to both identify the key chemical species of interest and their concentrations, which may better inform flame properties such as heat release, and to better understand the length scales necessary to resolve in order to better characterize the flames.

Appendix A

A. Other Projects and Contributions

In addition to the research efforts described in this dissertation, other avenues have been explored that require additional work or lie outside the scope of this dissertation. However, in each case, a new method or technique was developed that warrants discussion. In this section, three avenues of research are discussed, including their potential value to the engineering community, as well as how such work could be continued in the future.

A.1. FBE Setup for Scramjet Visualization

In Chapter 4, an FBE-based setup using a single camera was used to visualize very large, turbulent flames within a ground vehicle testbed. While there were significant challenges in these field measurements, many of which were overcome due to the flexibility of the setup, time-resolved 3D tomographic measurements were ultimately obtained that allowed for analysis of the time evolution of the target flames. This same FBE-based visualization setup was modified to view much smaller flames within the University of Virginia Hypersonics Research Complex. The FBE setup was oriented on either side of a supersonic combustor, which had two small observation windows at the flame holder location. Using this setup, data was collected of a simulated Mach 5 scramjet flame from nine different view orientations using a single camera. Figure A.1 shows the experimental arrangement and the test rig, where the single camera was mounted to an optical table and the nine fiber inputs were distributed on either side of the scramjet. Each FBE input was wrapped with foil tape in an attempt to reduce thermal radiation from the scramjet. In this particular instance, given that the FBE bundle was significantly less expensive than a single high-speed camera, being able to move the camera a considerable distance from the scramjet greatly reduced the risk of thermal damage to the camera.
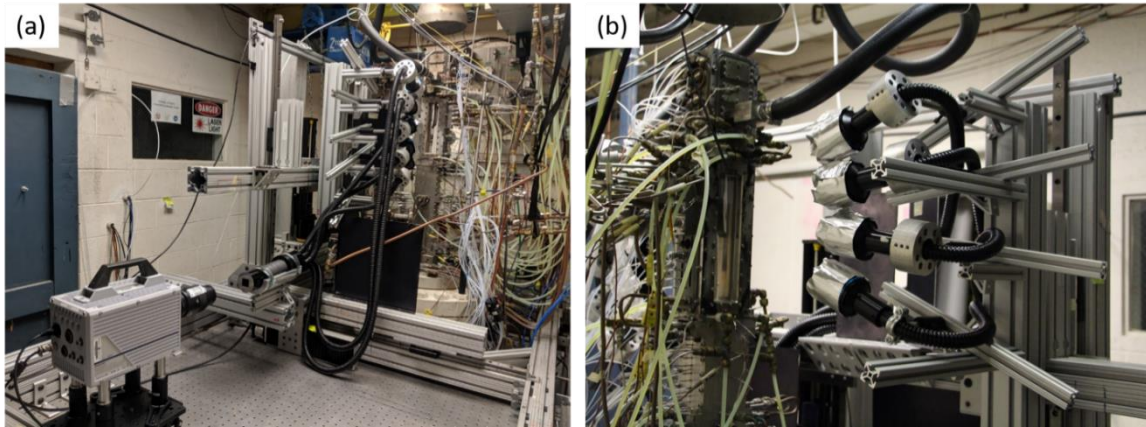
Figure A.1: Photo of the scramjet sensor setup from a) the front, and b) the back

While the initial goal was to obtain time-resolved measurements of the scramjet flame, two major hurdles were encountered. The first was that the flame intensity signal was too weak at frame rates high enough to temporally resolve the flame. Second, there was significant reflection and other signal sources that obscured the flame signal, making even time-averaged measurements difficult. Figure A.2 shows an example of an instantaneous measurement from the nine FBE inputs. The top five views are taken from the front, and the bottom four are from the back. In this case, data was taken at 1000 frames per second, which is not nearly fast enough to temporally resolve the flame dynamics, while still suffering from a very low signal level. As an example, given the approximate velocity of the Mach 5 flow, a frame rate of 1,000,000 Hz would be necessary to reach a spatial resolution of 1 mm (assuming hardware was not a limiting factor). Therefore, the flow visualized in Fig. A.2 is time-averaged. In addition to this challenge, the other signal sources, which are expected to be reflections on the polycarbonate windows and blackbody radiation from the heated flame holder, are much stronger than the flame signal. To enable data of sufficient quality to perform a tomographic analysis, these challenges must be overcome. However, to the author's knowledge, this was the first time that such multi-view measurements of scramjet flames have been attempted with the goal of obtaining
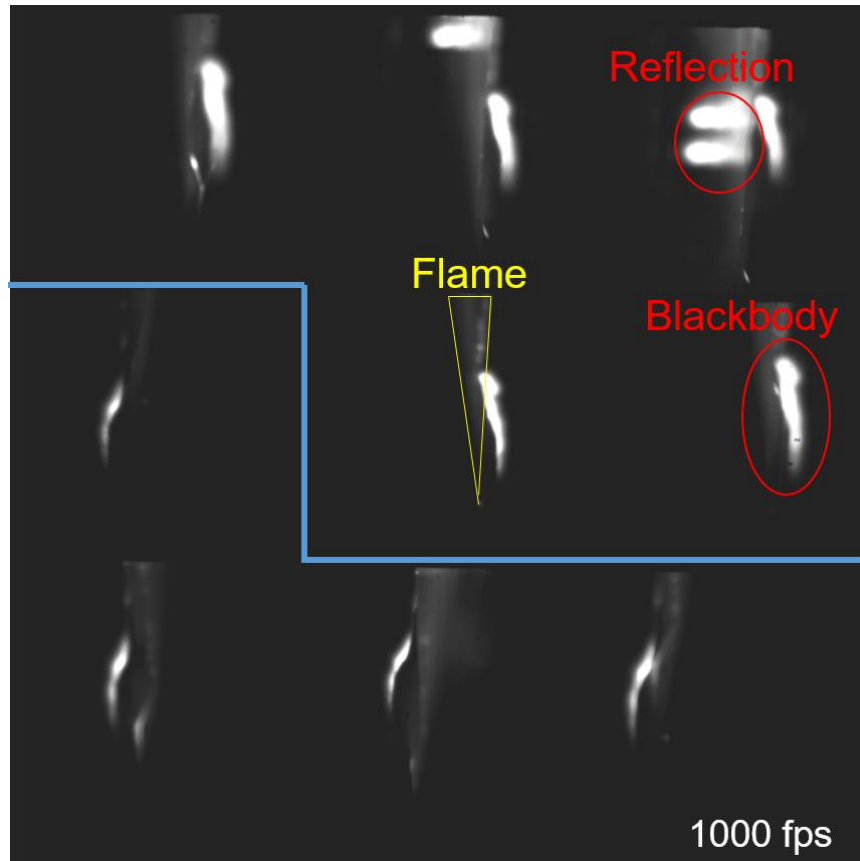
Figure A.2: An instantaneous measurement of the scramjet flame from the nine different FBE inputs, illustrating the challenges encountered

measurements of scramjet flames have been attempted with the goal of obtaining tomographic scramjet flame measurements.

A.2. Adaptive Spatial Discretization Based on Projections

One proposed method to implement the adaptive spatial discretization (ASD) technique was to use information based on the measured projections, as opposed to determining the regions of interest based on a preliminary reconstruction (as described in Chapter 2), similar to the implementation of the masking technique. In this method, the signal gradients were calculated from the measured projections, and those regions deemed as having high signal gradients were highlighted. Then, for each view, all the voxels that
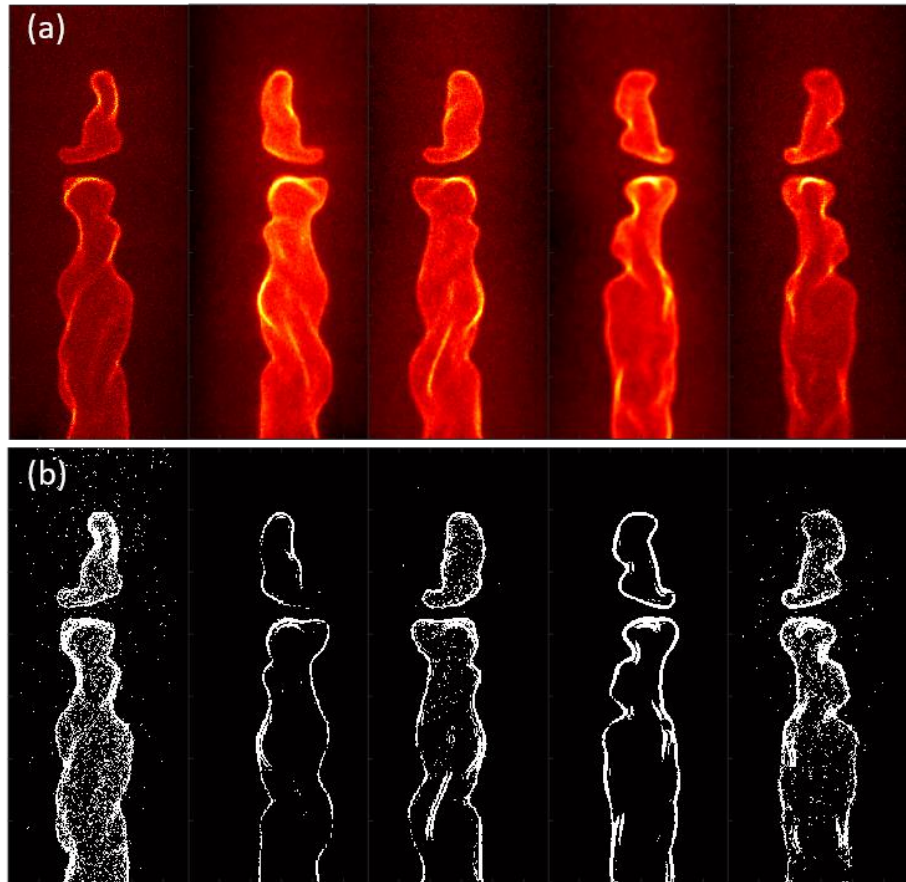
Figure A.3: a) Measured projections of the VLIF signal from five cameras, and b) the high gradient regions extracted from the projections

contributed to highlighted pixels were flagged while using a coarse voxel discretization throughout. The flagged voxels were converted into finely discretized voxels if enough views agreed that the voxel should be flagged for fine discretization. Figure A.3a shows an instantaneous measurement from the Hi-Pilot burner (described in Chapter 3) under low flow and turbulent conditions, making the flame nearly laminar. Figure A.3b shows the regions of large spatial gradients from the projections as highlighted pixels. Besides the high gradient regions detected due to noise, particularly on the far-left measurement, these regions of large gradient are mostly concentrated near the edge of the flame, which corresponds to where we expect the thin CH signal to be, as discussed in Chapter 3.

Figure A.4: Cross-section of the measurement volume showing voxels that would be treated with fine discretization (in white) based on how many views agree

Using the gradient images derived from the measured projections, a binary tomographic reconstruction was performed to determin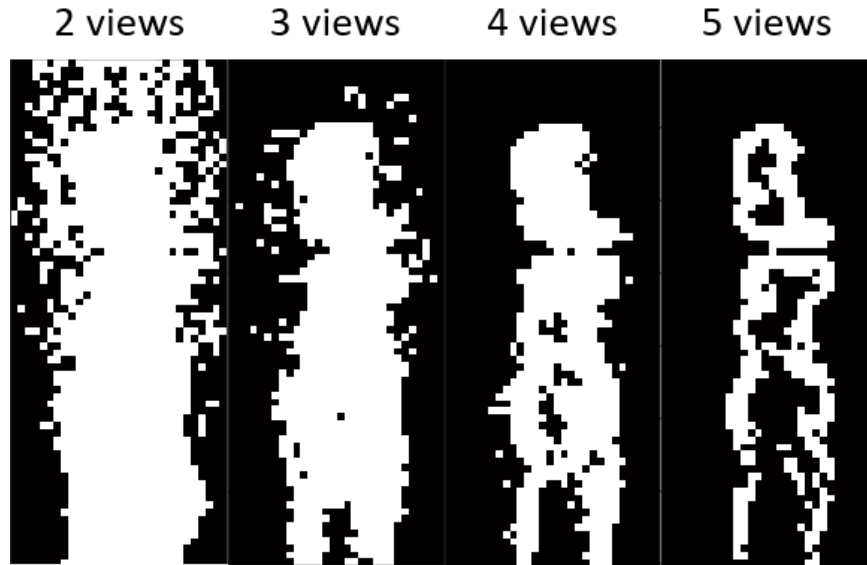e the regions requiring higher spatial resolution, similar to the methods described in Ref. [99]. Figure A.4 shows a central cross-section of the measurement volume with voxels that would be treated with a fine discretization based on how many views agree that they contribute to high-gradient regions on the projections. As seen, when four or five views are required to agree that a voxel contributes to high-gradient regions on the projection, the distribution of finely-discretized voxels matches well with what one would expect the flame distribution (based on CH, as in Chapter 3) to be. This indicates that this method of implementing ASD was successful for this relatively simple flame.

For more complicated signal distributions, however, this implementation has a critical flaw, as it is possible for there to be significant spatial gradients in the 3D signal distribution yet little gradient in the projection pixel intensity. To illustrate this, consider the example of a Sudoku puzzle, where the sum of each index across the horizontal and vertical all equal the same constant value. Under these conditions, some of the projections of such a distribution will have little to no gradient in signal. Figure A.5 shows an example
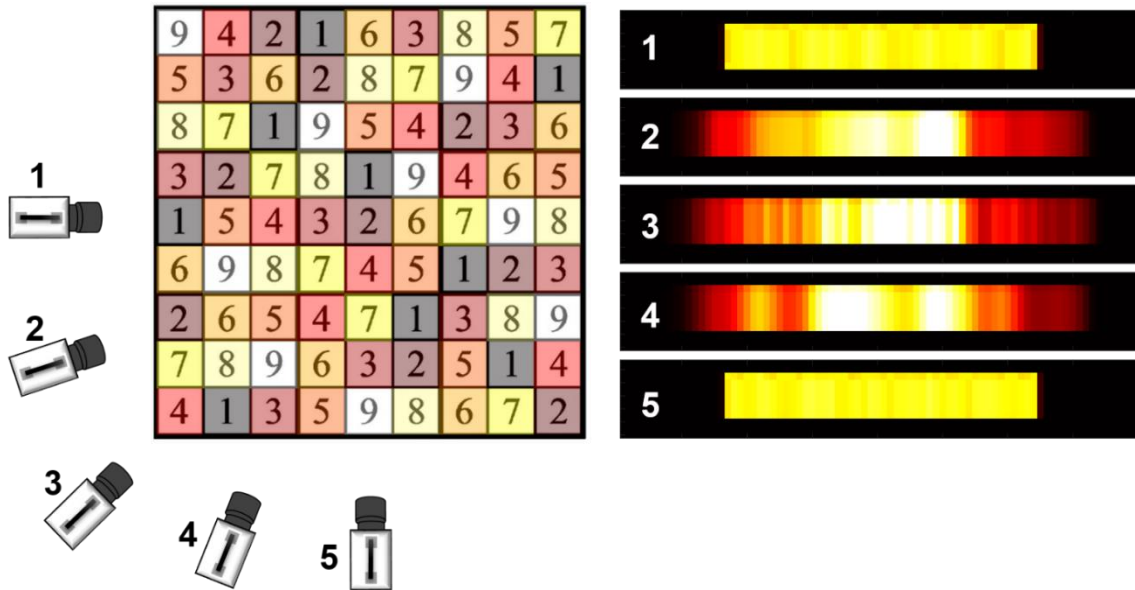
94

Figure A.5: Example projections taken of a "Sudoku" distribution, where the significant spatial gradients are not apparent in the measured projections

of a "Sudoku" distribution with five projections. The projections measured from the horizontal and vertical show no spatial gradient as expected, and the other projections have relatively smooth signal gradients that belie the significant spatial gradients within the measurement volume. For this reason, the implementation of ASD described in Chapter 2 is more widely applicable and resilient. However, the implementation described here shows promise under some conditions and opens an avenue for additional research into what flame properties can be extracted from the measured projections that may improve reconstruction efficiency or accuracy.

A.3. Tomography using Proper Orthogonal Decomposition

While the masking method and the implementation of the ASD described in A.2 sought to improve the efficiency of computed tomography by leveraging information obtained from the measured projections, attempts have been made to use information already gained about the nature of the flame to improve tomographic reconstruction efficiency and accuracy that are described in this section. For instance, it is possible to collect a significant number of measurements from a particular type of flame (like a specific

burner under specific flow conditions) and perform normal tomographic reconstructions for each of those measurements. This yields a large dataset of known 3D distributions of the flame. The information gained from this dataset can then inform the reconstruction of future measurements under the same flow conditions. One application of this is to use machine learning to help predict 3D distributions from their projections based on the previously reconstructed training dataset [46, 47]. One downside to this method is that the information learned from the training set is essentially unknown and perhaps uninterpretable by the users.

As a similar alternative method, the 3D reconstructions in the training dataset may be analyzed through what is called proper orthogonal decomposition (POD). The use of POD is to reduce (decompose) the information in a dataset, in this case, the 3D signal distribution, into orthogonal modes (eigenvectors), with eigenvectors representing their contribution to the entire dataset. For example, the eigenvector with the largest eigenvalue is the 3D distribution that most encapsulates all the distributions in the training dataset. Therefore, POD can also be used as an analysis technique and the results can be interpreted intuitively. Using the modes calculated from POD, any 3D distribution within the dataset can be completely described by a linear combination of modes and their respective amplitudes (eigenvalues), as shown in Eq. A.1:

$$F(x, y, z) = \sum_{k=1}^{N_k} a_k \, \phi_k(x, y, z) \,, \tag{A.1}$$

where F is the 3D distribution, ϕ_k is the kth mode, and a_k is the amplitude of the kth mode. As long as all of the 3D distributions in the training dataset are not orthogonal (which is almost always the case in practical scenarios), the total number of modes will be significantly less than the total number of voxels in the distribution. Using this description for F, Eq. 2.1 can be rewritten as:

$$P(x_P, y_P) = \sum_{k=1}^{N_k} a_k \, \phi_k(x, y, z) \cdot PSF(x, y, z; \, x_P, y_P) \,. \tag{A.2}$$

Similar to solving the typical tomography problem, this reduced problem can be solved using ART with Eq. 2.2, where instead of solving for the value of every voxel for an

unknown distribution, one can instead solve for every scalar amplitude for each of the modes by iteratively looping over all of the measured projections' pixels. In Eq. A.2, every mode ϕ_k is known from POD, and PSF is calculated in the usual way. The only unknowns in the problem are the N_k scalar values of a_k.

To test the effectiveness of this method, a large dataset of various fluid flow fields was used, where the 3D distribution of interest was the absolute magnitude of the fluid velocity, which was discretized essentially into voxels of uniform size. POD was applied to this dataset to identify the modes within the flow field. The goal of applying POD to the tomography problem was to reduce the overall scale of the problem and therefore reduce the computational cost of performing the reconstruction, with the hopes of drastically reducing computation time. However, one major challenge encountered in this implementation was that nearly every mode contributed to nearly every pixel, whereas in the typical formulation, each voxel only contributes to a handful of pixels. Due to this, while the total number of unknowns is significantly reduced (from the total number of voxels to the number of amplitudes), the iterative process actually takes more computation time. Another challenge of this implementation is the key assumption that an unknown distribution is capable of being accurately reproduced through a linear combination of the modes and their amplitudes.

The POD method is undoubtedly a powerful tool for the analysis of datasets, but it has shown to have challenges in implementation for tomography. If these challenges can be overcome, the use of POD to improve the efficiency of tomography could be significant and this avenue warrants additional research. Additionally, because the POD method (and the use of machine learning) requires a large database of measurement results for training, even better if those measurements are time-resolved, there is further motivation to collect high-quality data from novel experimental setups such as the simultaneous PLIF/VLIF measurements described in Chapter 3.

References

[1]   P. Wright, N. Terzija, J.L. Davidson, S. Garcia-Castillo, C. Garcia-Stewart, S. Pegrum, S. Colbourne, P. Turner, S.D. Crossley, T. Litt, S. Murray, K.B. Ozanyan, H. McCann, High-speed chemical species tomography in a multi-cylinder automotive engine, Chem. Eng. J. 158 (2010) 2-10.

[2]   K.M. Busa, B.E. Rice, J.C. McDaniel, C.P. Goyne, R.D. Rockwell, J.A. Fulton, J.R. Edwards, G.S. Diskin, Scramjet Combustion Efficiency Measurement via Tomographic Absorption Spectroscopy and Particle Image Velocimetry, AIAA Journal 54 (2016) 2463-2471.

[3]   A. Unterberger, M. Röder, A. Giese, A. Al-Halbouni, A. Kempf, K. Mohri, 3D Instantaneous Reconstruction of Turbulent Industrial Flames Using Computed Tomography of Chemiluminescence (CTC), Journal of Combustion 2018 (2018) 5373829.

[4]   K. Kohse-Höinghaus, Combustion in the future: The importance of chemistry, P. Combust. Inst. 38 (2021) 1-56.

[5]   M. Aldén, J. Bood, Z. Li, M. Richter, Visualization and understanding of combustion processes using spatially and temporally resolved laser diagnostic techniques, P. Combust. Inst. 33 (2011) 69-97.

[6]   K.-H. Nam, J.-S. Lee, H.-J. Park, Understanding Combustion Mechanism of Magnesium for Better Safety Measures: An Experimental Study, Safety 8 (2022) 11.

[7]   O. Fujita, Solid combustion research in microgravity as a basis of fire safety in space, P. Combust. Inst. 35 (2015) 2487-2502.

[8]   M.J. Hurley, D.T. Gottuk, J.R. Hall Jr, K. Harada, E.D. Kuligowski, M. Puchovsky, J.M. Watts Jr, C.J. WIECZOREK, SFPE handbook of fire protection engineering, Springer2015.

[9]   H. Xia, R. Kan, Z. Xu, Y. He, J. Liu, B. Chen, C. Yang, L. Yao, M. Wei, G. Zhang, Two-step tomographic reconstructions of temperature and species concentration in a flame based on laser absorption measurements with a rotation platform, Opt. Laser. Eng. 90 (2017) 10-18.

[10] Y. Hardalupas, M. Orain, Local measurements of the time-dependent heat release rate and equivalence ratio using chemiluminescent emission from a flame, Combust. Flame 139 (2004) 188-207.

[11] S.M. Wiseman, M.J. Brear, R.L. Gordon, I. Marusic, Measurements from flame chemiluminescence tomography of forced laminar premixed propane flames, Combust. Flame 183 (2017) 1-14.

[12] S. Krishnan, B.M. Kumfer, W. Wu, J. Li, A. Nehorai, R.L. Axelbaum, An Approach to Thermocouple Measurements That Reduces Uncertainties in High-Temperature Environments, Energy & Fuels 29 (2015) 3446-3455.

[13] F. Fuest, R.S. Barlow, G. Magnotti, A. Dreizler, I.W. Ekoto, J.A. Sutton, Quantitative acetylene measurements in laminar and turbulent flames using 1D Raman/Rayleigh scattering, Combust. Flame 162 (2015) 2248-2255.

[14] Y. Wu, M. Gragston, Z. Zhang, P.S. Hsu, N. Jiang, A.K. Patnaik, S. Roy, J.R. Gord, High-pressure 1D fuel/air-ratio measurements with LIBS, Combust. Flame 198 (2018) 120-129.

[15] J. Hayashi, N. Hashimoto, N. Nakatsuka, H. Tsuji, H. Watanabe, H. Makino, F. Akamatsu, Soot formation characteristics in a lab-scale turbulent pulverized coal flame with simultaneous planar measurements of laser induced incandescence of soot and Mie scattering of pulverized coal, P. Combust. Inst. 34 (2013) 2435-2443.

[16] K.Y. Cho, A. Satija, T.L. Pourpoint, S.F. Son, R.P. Lucht, High-repetition-rate three-dimensional OH imaging using scanned planar laser-induced fluorescence system for multiphase combustion, Appl. Opt. 53 (2014) 316-326.

[17] J. Bode, J. Schorr, C. Krüger, A. Dreizler, B. Böhm, Influence of the in-cylinder flow on cycle-to-cycle variations in lean combustion DISI engines measured by high-speed scanning-PIV, P. Combust. Inst. 37 (2019) 4929-4936.

[18] M. Zhang, J. Wang, W. Jin, Z. Huang, H. Kobayashi, L. Ma, Estimation of 3D flame surface density and global fuel consumption rate from 2D PLIF images of turbulent premixed flame, Combust. Flame 162 (2015) 2087-2097.

[19] I. Ihrke, M. Magnor, Image-based tomographic reconstruction of flames, Proceedings of the 2004 ACM SIGGRAPH/Eurographics symposium on Computer animation, Association for Computing Machinery, Grenoble, France, 2004, pp. 365–373.

[20] W. Cai, X. Li, F. Li, L. Ma, Numerical and experimental validation of a three-dimensional combustion diagnostic based on tomographic chemiluminescence, Opt. Express 21 (2013) 7050-7064.

[21] G.T. Herman, Image Reconstruction From Projections, Real-Time Imaging 1 (1995) 3-18.

[22] G.T. Herman, Image reconstruction from projections, The fundamental of computerized tomography, (1980) 260-276.

[23] L.A. Shepp, J.B. Kruskal, Computerized Tomography: The New Medical X-Ray Technology, The American Mathematical Monthly 85 (1978) 420-439.

[24] G. van Kaick, S. Delorme, Computed tomography in various fields outside medicine, European Radiology Supplements 15 (2005) d74-d81.

[25] K.A. Dines, R.J. Lytle, Computerized geophysical tomography, Proceedings of the IEEE 67 (1979) 1065-1073.

[26] N. Denisova, P. Tretyakov, A. Tupikin, Emission tomography in flame diagnostics, Combust. Flame 160 (2013) 577-588.

[27] S.J. Grauer, K. Mohri, T. Yu, H. Liu, W. Cai, Volumetric emission tomography for combustion processes, Prog. Energy Combust. Sci. 94 (2023) 101024.

[28] L. Ma, Q. Lei, J. Ikeda, W. Xu, Y. Wu, C.D. Carter, Single-shot 3D flame diagnostic based on volumetric laser induced fluorescence (VLIF), P. Combust. Inst. 36 (2017) 4575-4583.

[29] M. Gomez, B.W. Yant, M.N. Slipchenko, A.M. Braun, Z.D. Rancilio, T.R. Meyer, S. Roy, Four-dimensional laser-induced fluorescence and tomography of liquids, Int. J. Multiphase Flow 166 (2023) 104501.

[30] X. Li, L. Ma, Capabilities and limitations of 3D flame measurements based on computed tomography of chemiluminescence, Combust. Flame 162 (2015) 642-651.

[31] X. Li, L. Ma, Volumetric imaging of turbulent reactive flows at kHz based on computed tomography, Opt. Express 22 (2014) 4768-4778.

[32] J. Floyd, P. Geipel, A.M. Kempf, Computed Tomography of Chemiluminescence (CTC): Instantaneous 3D measurements and Phantom studies of a turbulent opposed jet flame, Combust. Flame 158 (2011) 376-391.

[33] Y. Yan, T. Qiu, G. Lu, M.M. Hossain, G. Gilabert, S. Liu, Recent Advances in Flame Tomography, Chin. J. Chem. Eng. 20 (2012) 389-399.

[34] K. Wang, F. Li, H. Zeng, X. Yu, Three-dimensional flame measurements with large field angle, Opt. Express 25 (2017) 21008-21018.

[35] A. Goyal, S. Chaudhry, P.M.V. Subbarao, Direct three dimensional tomography of flames using maximization of entropy technique, Combust. Flame 161 (2014) 173-183.

[36] Y. Jin, W. Zhang, Y. Song, X. Qu, Z. Li, Y. Ji, A. He, Three-dimensional rapid flame chemiluminescence tomography via deep learning, Opt. Express 27 (2019) 27308-27334.

[37] L. Ma, Y. Wu, Q. Lei, W. Xu, C.D. Carter, 3D flame topography and curvature measurements at 5 kHz on a premixed turbulent Bunsen flame, Combust. Flame 166 (2016) 66-75.

[38] J. Wang, Y. Song, Z.-h. Li, A. Kempf, A.-z. He, Multi-directional 3D flame chemiluminescence tomography based on lens imaging, Opt. Lett. 40 (2015) 1231-1234.

[39] A.K. Agarwal, A. Agarwal, A.P. Singh, Time resolved in-situ biodiesel combustion visualization using engine endoscopy, Measurement 69 (2015) 236-249.

[40] H. Liu, B. Sun, W. Cai, kHz-rate volumetric flame imaging using a single camera, Optics Communications 437 (2019) 33-43.

[41] S.E. Hodges, Fire Protection in Military Ground Vehicles, SAE International Journal of Transportation Safety 4 (2016) 229-235.

[42] V. Korivi, S. McCormick, S. Hodges, Fire Suppression Modeling & Simulation Framework for Ground Vehicles, SAE International journal of transportation safety 5 (2017) 58-67.

[43] F. Nicolas, V. Todoroff, A. Plyer, G. Le Besnerais, D. Donjat, F. Micheli, F. Champagnat, P. Cornic, Y. Le Sant, A direct approach for instantaneous 3D density field reconstruction from background-oriented schlieren (BOS) measurements, Exp. Fluids 57 (2015) 13.

[44] C. Wei, K.K. Schwarm, D.I. Pineda, R.M. Spearrin, Volumetric laser absorption imaging of temperature, CO and CO2 in laminar flames using 3D masked Tikhonov regularization, Combust. Flame 224 (2021) 239-247.

[45] B. Kanmani, R.M. Vasu, Diffuse optical tomography using intensity measurements and the a priori acquired regions of interest: theory and simulations, Physics in Medicine & Biology 50 (2005) 247.

[46] L. Zhou, Y. Song, W. Ji, H. Wei, Machine learning for combustion, Energy and AI 7 (2022) 100128.

[47] J. Huang, H. Liu, Q. Wang, W. Cai, Limited-projection volumetric tomography for time-resolved turbulent combustion diagnostics via deep learning, Aerospace Science and Technology 106 (2020) 106123.

[48] A. Wickersham, W. Cai, L. Ma, Application of proper orthogonal decomposition to hyperspectral tomographic imaging of unsteady flows, 51st AIAA Aerospace Sciences Meeting including the New Horizons Forum and Aerospace Exposition.

[49] H. Wang, L. Tang, Z. Cao, An image reconstruction algorithm based on total variation with adaptive mesh refinement for ECT, Flow Measurement and Instrumentation 18 (2007) 262-267.

[50] M. Molinari, S.J. Cox, B.H. Blott, G.J. Daniell, Adaptive mesh refinement techniques for electrical impedance tomography, Physiological Measurement 22 (2001) 91.

[51] R. Zhang, J. Si, G. Enemali, Y. Bao, C. Liu, Spatially Driven Chemical Species Tomography With Size-Adaptive Hybrid Meshing Scheme, IEEE Sens. J. 22 (2022) 12728-12737.

[52] W. Bangerth, A. Joshi, Adaptive finite element methods for the solution of inverse problems in optical tomography, Inverse Problems 24 (2008) 034011.

[53] S. Ren, H. Hu, G. Li, X. Cao, S. Zhu, X. Chen, J. Liang, Multi-atlas registration and adaptive hexahedral voxel discretization for fast bioluminescence tomography, Biomedical Optics Express 7 (2016) 1549-1560.

[54] G. Molesini, Geometrical Optics, in: F. Bassani, G.L. Liedl, P. Wyder (Eds.), Encyclopedia of Condensed Matter Physics, Elsevier, Oxford, 2005, pp. 257-267.

[55] A. Lahiri, Chapter 2 - Foundations of Ray Optics, in: A. Lahiri (Ed.), Basic Optics, Elsevier, Amsterdam, 2016, pp. 141-202.

[56] S.J. Grauer, A.M. Steinberg, Fast and robust volumetric refractive index measurement by unified background-oriented schlieren tomography, Exp. Fluids 61 (2020) 80.

[57] P. Modregger, M. Kagias, S. Peter, M. Abis, V.A. Guzenko, C. David, M. Stampanoni, Multiple Scattering Tomography, Phys. Rev. Lett. 113 (2014) 020801.

[58] F. Natterer, F. Wübbeling, Mathematical methods in image reconstruction, SIAM2001.

[59] T. Nielsen, R. Manzke, R. Proksa, M. Grass, Cardiac cone-beam CT volume reconstruction using ART, Medical Physics 32 (2005) 851-860.

[60] N.D. Prionas, S. Ray, J.M. Boone, Volume assessment accuracy in computed tomography: a phantom study, Journal of Applied Clinical Medical Physics 11 (2010) 168-180.

[61] E. Kamutta, Mäkinen, Sofia, & Meaney, Alexander, Cone-Beam Computed Tomography Dataset of a Seashell (1.1.0) [Data set], Zenodo, doi:https://doi.org/10.5281/zenodo.6983008(2022).

[62] A.W. Skiba, T.M. Wabel, C.D. Carter, S.D. Hammack, J.E. Temme, J.F. Driscoll, Premixed flames subjected to extreme levels of turbulence part I: Flame structure and a new measured regime diagram, Combust. Flame 189 (2018) 407-432.

[63] H. Villarraga-Gómez, S.T. Smith, Effect of the number of projections on dimensional measurements with X-ray computed tomography, Precision Engineering 66 (2020) 445-456.

[64] Y. Ishino, N. Ohiwa, Three-Dimensional Computerized Tomographic Reconstruction of Instantaneous Distribution of Chemiluminescence of a Turbulent

Premixed Flame, JSME International Journal Series B Fluids and Thermal Engineering 48 (2005) 34-40.

[65] W. Cai, X. Li, L. Ma, Practical aspects of implementing three-dimensional tomography inversion for volumetric flame imaging, Appl. Opt. 52 (2013) 8106-8116.

[66] R. Keys, Cubic convolution interpolation for digital image processing, IEEE Transactions on Acoustics, Speech, and Signal Processing 29 (1981) 1153-1160.

[67] H. Liu, Q. Wang, F. Peng, Z. Qin, W. Cai, Flame emission tomography based on finite element basis and adjustable mask, Opt. Express 29 (2021) 40841-40853.

[68] D. Adhikari, E.K. Longmire, Visual hull method for tomographic PIV measurement of flow around moving objects, Exp. Fluids 53 (2012) 943-964.

[69] L. Ma, Q. Lei, T. Capil, S.D. Hammack, C.D. Carter, Direct comparison of two-dimensional and three-dimensional laser-induced fluorescence measurements on highly turbulent flames, Opt. Lett. 42 (2017) 267-270.

[70] K.T. Walsh, M.B. Long, M.A. Tanoff, M.D. Smooke, Experimental and computational study of CH, CH*, and OH* in an axisymmetric laminar diffusion flame, Symposium (International) on Combust. 27 (1998) 615-623.

[71] R.K. Hanson, J.M. Seitzman, P.H. Paul, Planar laser-fluorescence imaging of combustion gases, Appl. Phys. B 50 (1990) 441-454.

[72] P.H. Paul, H.N. Najm, Planar laser-induced fluorescence imaging of flame heat release rate, Symposium (International) on Combust. 27 (1998) 43-50.

[73] W. Xu, C.D. Carter, S. Hammack, L. Ma, Analysis of 3D combustion measurements using CH-based tomographic VLIF (volumetric laser induced fluorescence), Combust. Flame 182 (2017) 179-189.

[74] J.G. Speight, Chapter 10 - Combustion of hydrocarbons, in: J.G. Speight (Ed.), Handbook of Industrial Hydrocarbon Processes (Second Edition), Gulf Professional Publishing, Boston, 2020, pp. 421-463.

[75] R. Yang, X. Sun, Z. Liu, Y. Zhang, J. Fu, A Numerical Analysis of the Effects of Equivalence Ratio Measurement Accuracy on the Engine Efficiency and Emissions at Varied Compression Ratios, Processes, 2021.

[76] C.D. Carter, S. Hammack, T. Lee, High-speed planar laser-induced fluorescence of the CH radical using the C-2 Sigma(+) X-2 Pi(0,0) band, Appl. Phys. B 116 (2014) 515-519.

[77] W. Ubachs, G. Meyer, J.J. ter Meulen, A. Dymanus, Hyperfine structure and lifetime of the C-2 Sigma(+), v=0 state of CH, The Journal of Chemical Physics 84 (1986) 3032-3041.

[78] M. Kang, Y. Wu, L. Ma, Fiber-based endoscopes for 3D combustion measurements: view registration and spatial resolution, Combust. Flame 161 (2014) 3063-3072.

[79] H.N. Najm, O.M. Knio, P.H. Paul, P.S. Wyckoff, A Study of Flame Observables in Premixed Methane - Air Flames, Combust. Sci. Technol. 140 (1998) 369-403.

[80] P.C. Hansen, Analysis of Discrete Ill-Posed Problems by Means of the L-Curve, SIAM Rev. 34 (1992) 561-580.

[81] A.M. Vossepoel, A.W.M. Smeulders, Vector code probability and metrication error in the representation of straight lines of finite length, Computer Graphics and Image Processing 20 (1982) 347-364.

[82] R.B. Stoa, The coastline paradox, Rutgers UL Rev. 72 (2019) 351.

[83] J.F. Driscoll, Turbulent premixed combustion: Flamelet structure and its effect on turbulent burning velocities, Prog. Energy Combust. Sci. 34 (2008) 91-134.

[84] R.K. Hanson, Applications of quantitative laser sensors to kinetics, propulsion and practical energy systems, P. Combust. Inst. 33 (2011) 1-40.

[85] K. Kohse-Höinghaus, J.B. Jeffries, Applied combustion diagnostics, Ch8. Multidimensional Diagnostics in Space and Time, 2002.

[86] H.M. Hertz, G.W. Faris, Emission tomography of flame radicals, Opt. Lett. 13 (1988) 351-353.

[87] R. Wellander, M. Richter, M. Aldén, Time-resolved (kHz) 3D imaging of OH PLIF in a flame, Exp. Fluids 55 (2014) 1764.

[88] J. Floyd, A. Kempf, Computed tomography of chemiluminescence (CTC): high resolution and instantaneous 3-D measurements of a matrix burner, P. Combust. Inst. 33 (2011) 751-758.

[89] R.K. Hanson, R.M. Spearrin, C.S. Goldenstein, Spectroscopy and optical diagnostics for gases, Springer2016.

[90] C.S. Goldenstein, R.M. Spearrin, J.B. Jeffries, R.K. Hanson, Infrared laser-absorption sensing for combustion gases, Prog. Energy Combust. Sci. 60 (2017) 132-176.

[91] A.C. Eckbreth, Laser diagnostics for combustion temperature and species, CRC press1996.

[92] T.D. Upton, D.D. Verhoeven, D.E. Hudgins, High-resolution computed tomography of a turbulent reacting flow, Exp. Fluids 50 (2011) 125-134.

[93] J.-Y. Bouguet, Complete camera calibration toolbox for matlab, 2004.

[94] N. Liu, Q. Lei, Y. Wu, L. Ma, 3D tomography reconstruction improved by integrating view registration, Appl. Opt. 58 (2019) 2596-2604.

[95] N. Liu, K. Zhou, L. Ma, 3D tomography integrating view registration and its application in highly turbulent flames, Combust. Flame 221 (2020) 429-440.

[96] A. Yoshida, M. Narisawa, H. Tsuji. Structure of highly turbulent premixed flames. In Symposium (International) on Combustion; 1992: Elsevier. p. 519-525.

[97] A.S. Huzayyin, H.A. Moneib, M.S. Shehatta, A.M.A. Attia, Laminar burning velocity and explosion index of LPG–air and propane–air mixtures, Fuel 87 (2008) 39-57.

[98] S.-Y. Lee, S.R. Turns, R.J. Santoro, Measurements of soot, OH, and PAH concentrations in turbulent ethylene/air jet flames, Combust. Flame 156 (2009) 2264-2275.

[99] W. Cai, L. Ma, Comparison of approaches based on optimization and algebraic iteration for binary tomography, Comput. Phys. Commun. 181 (2010) 1974-1981.